August 2016

# Experimental, Analytical and Numerical Characterization of Effects of Fiber Waviness Defects in Laminated Composites

Seyedmohammadsadegh Shams
*University of Wisconsin-Milwaukee*

# EXPERIMENTAL, ANALYTICAL AND NUMERICAL CHARACTERIZATION OF EFFECTS OF FIBER WAVINESS DEFECTS IN LAMINATED COMPOSITES

by

Seyedmohammadsadegh Shams

A Dissertation Submitted in

Partial Fulfillment of the

Requirements for the Degree of

Doctor of Philosophy

in Engineering

at

The University of Wisconsin- Milwaukee

August 2016

ABSTRACT

**EXPERIMENTAL, ANALYTICAL AND NUMERICAL CHARACTERIZATION OF EFFECTS OF FIBER WAVINESS DEFECTS IN LAMINATED COMPOSITES**

by
Seyedmohammadsadegh Shams

University of Wisconsin- Milwaukee, 2016
Under the Supervision of Professor Rani F. Elhajjar

Fiber waviness is one of the most common defects observed in reinforced laminated composites which can occur during manufacturing. The effects of waviness on the mechanical responses of laminated composites under the standard mechanical testing are investigated with proposed experiments, analytical and numerical approaches. The damage consequences including kink band formation, crack onset, delamination and fiber fractures are characterized by means of full field digital imaging and acoustic emission techniques. The notch and waviness size effects on the notched composite compressive and tensile strength are studied using a progressive damage approach using the finite element method. A numerical approach based on a combined continuum damage analysis and cohesive zone interlaminar behavior is proposed to simulate the failure initiation and propagation responses. The proposed FE modeling approach will attempt to predict the response of the laminate structure inferring distinctive failure mechanisms and their interactions with the defects. Hybrid near infrared hyperspectral imaging surfaces with a bottom-up design discretization approach have been developed to build the finite element model. The proposed method overcomes the limitations of current wrinkle assessment methods by connecting the high sensitivity near infrared hyperspectral measurements to direct structural models. Temporal evaluations of the load-deformation response, acoustic emissions, and optical microscopy are used to study and verify the failure modes and damage progression models in the

tension and compression specimens. An analytical model based on the orthotropic stress concentration factor and a generalized expression using traction continuity through the kink band is developed to predict failure strength of the Open Hole Compression (OHC) specimens. In this thesis, a new methodology to determine the limit point is also proposed based on the out-of-plane displacement tracking using an image correlation method. The method can be used to determine the start of incipient interlaminar delamination in continuous fiber reinforced composite materials.

To
the memory of my beloved parents

# TABLE OF CONTENTS

# LIST OF FIGURES

# LIST OF TABLES

# ACKNOWLEDGMENTS

Firstly, I would like to express my sincere gratitude to my advisor Prof. Rani Elhajjar for the continuous support of my Ph.D. study and related research, for his patience, motivation, and immense knowledge. His fundamental guidance helped me in all the time of research and writing of this thesis. The joy and enthusiasm he has for the research was contagious and motivational for me, even during tough times in my life and the Ph.D. pursuit.

I want to thank Dr. Adeeb Rahman who served as co-advisor in my defense and has taught me about finite element methods through the course that I have taken with him. I would also like to thank to members of my committee, Dr. Hani Titi, Dr. Anoop Dhingra (Department of Mechanical Engineering), Dr. Benjamin Church (Department of Materials Science and Engineering) for the assistance they provided at all levels of this thesis and inspiration in many ways. I would also like to thank Dr. Anastasia Muliana from the Faculty of The Texas A&M University (Department of Mechanical Engineering) for taking time out from her busy schedule to serve as my external committee member.

I would like to express my gratitude to Gabor J. Kemeny president at Middleton Spectral Vision Company and his team who supported this study by providing hyperspectral imaging test setup and sharing their knowledge on the near infrared imaging approach.

The experimental part of this research would not have come to a successful completion, without the help I received from the Engineering Mechanics & Composite Research Laboratory at Civil and Environmental Engineering Department. I am grateful to Dr. Elhajjar and his team of friendly and cheerful fellow students, Peng Yang, Issam Qamhia, Hamid Erfanian and Marco Lo Ricco, that helped me a lot to do experiments.

Finally, I must acknowledge my wife Dr. Mohammedi and best friend and my son without whose loves and encouragement I would not have finished this thesis. In particular my special thanks goes to my sisters and my brother Dr. Saleh Shams for the support they provided me through my study.

# CHAPTER 1

# INTRODUCTION

## 1.1 Defects in Continuous Fiber-Reinforced Composites

Laminated continuous fiber-reinforced composites are now widely used in many applications primarily due to their relatively high specific strength and stiffness but more importantly for their design flexibilities and damage tolerance. These composites can be designed to possess different mechanical properties in different directions thus achieving highly optimized performances. The materials have wide applications in the aerospace, automotive, energy, infrastructure, biomedical and recreational applications. A large variety of fibers are available as reinforcements for composites from E-glass and S-glass fiber to extremely stiff fibers such as carbon and graphite fibers. The performance of such materials is limited by the ability to withstand mechanical, electrical or environmental effects. The matrix provides a medium to protect and support fibers by transferring loads and local stresses between fibers. The most extensively used matrices are polymeric which can be Thermosets or Thermoplastics. Composite structures in practice can be

subjected to various types of damages which can be categorized as manufacturing or in service defects [1-6]. The manufacturing defects are caused by processing variability in composite fabrications, matrix flow and curing processes. Figure 1.1 shows some of the manufacturing defects in woven architecture composite panel applications. Since composites are notorious for Barely Visible Impact Damage (BVID) as well as None Visible Damage (NVD), their design loads and damage considerations must be taken into account for durability and design allowable considerations.

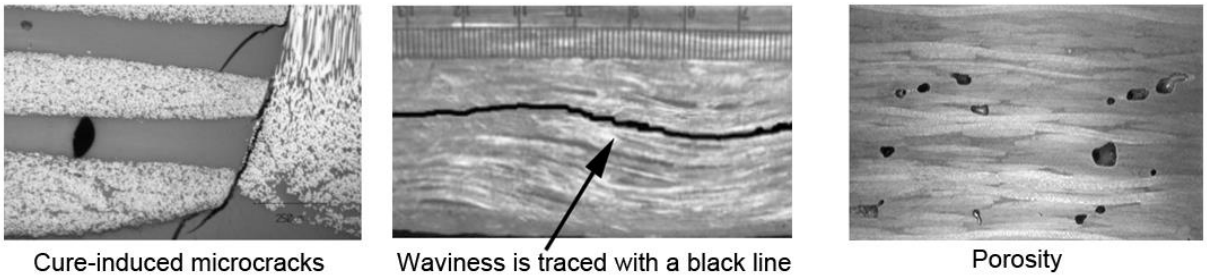


**Figure 1.1** Important manufacturing defects in composite laminates[7, 8]

Heslehurst and Scott [3]considered that the "level of structural degradation in engineering properties varied" with defect severity and location, load path criticality and stress state and history, detectability. Catastrophic failures in composite structures can occur due to the presence of manufacturing flaws not detected in manufacturing process or due to mechanical impact damage in the course of service [9, 10]. Manufacturing flaws can result in significant reductions in strength and stiffness of composites [11-14]. Delamination can occur at processing defects or in-service at stress concentrators such as holes, ply-drop-offs, stringer run-outs, etc.[15, 16].

Among many varieties in mechanical loadings, composites are vulnerable to impacts. Impacts can be classified into low to mid velocity impacts and high velocity impact. Each category

is associated with specialized damage mechanisms and progressions. Optimized composite structure usually employs very thin cross-sections in large areas. The damage can affect the structural load-bearing capability of the composite structure. Unlike metals in which many of these impacts may be absorbed by plastic deformation, the high-strength composites, in particular, carbon fiber reinforced plastics; result in different damage morphologies involving fiber and matrix failures. However, the coverage of the effects of defects in the published literature is limited, but concern for their effects is becoming more widespread, particularly as the aerospace industry increase composite material use for primary structures. It is the purpose of this thesis to investigate the defects which are likely to result from poor manufacturing, and to assess their potential to seriously degrade the performance of the composite. The implications for the development of new non-destructive testing techniques have been highlighted.

Composite structures are prone to the likelihood of manufacturing defects, which when suspected usually necessitate them being included as part of the build process or having the nonconforming parts handled on a case by case basis using the Material Review Board (MRB) process. Examples of such composite structures are the fuselage and wings of the Boeing 787 Dreamliner or the Airbus A350 airliners where some news reports have indicated the presence of such defects in production parts [17]. In addition, composite materials used in structural retrofitting of large infrastructure elements are also prone to these defects due to installation challenges in the field. Fiber waviness is known as one of the most common important manufacturing defects impacting the mechanical performance of composite structures. Fiber waviness may be caused by non-uniform consolidation pressure, interactions with other layers or ply drop-offs. The waviness can typically affect all or some of the plies in a laminate stack. The studies have conclusively shown that fiber waviness can significantly affect the un-notched tension and compression

stiffness and strength properties [13, 18-21].

## 1-2 Research Objectives

Composite laminates can be designed to operate a range of orthotropic mechanical properties such as stiffness and strength by arranging plies in different directions and taking advantages of woven textiles. The constituent materials appropriately can be reached by engineering the interfaces between constituents, and by devising the geometrical placement of the reinforcing constituent in the matrix. Damage tolerance and durability of composite laminates which play an important factor to utilize them in structure designs, performance degradation due to aging, fatigue under multiaxial loads and environmental condition issues such as response at elevated temperature are currently being investigated with a view to enhance the confidence levels associated with composite applications. The desired performance can be unachievable if preexisting imperfections have been not included in design. The damage tolerant feature of composites can be vulnerable if manufacturing defects eliminate in the analysis and designs.

The effects of waviness as one of the main manufacturing defects based on the initiation and propagation of damage in composites have been widely studied, but the physics and mechanics of the processes are not fully understood yet. There is limited understanding of how to model the waviness defects in analytical, experimental and numerical aspects. Also the experimental equipment to detect waviness and characterize its geometry is not well developed yet. Although it is generally accepted that this failure mode is related to misaligned fiber and matrix shear behavior, there is still much work to be done before the structure's failure to account for initiation. For this reason, the aim of the work presented in this thesis is to

synthesize and develop experiments, analytical and numerical models to understand the physical and mechanical process of failure formation, capable of predicting the composite's response under axial tensile and compressive and flexural loads.

### 1-3 Present Study

Chapter 1 contains previous significant studies regarding analytical and numerical analysis of composite laminates containing fiber waviness defects and nondestructive defect identification tests. Chapter 2 presents the basis of the numerical and analytical approaches used in this thesis. The experiments are explored under imaging and sounding approaches. Chapter 3 describes numerical and analytical approaches which will be used in this thesis. A synthesized analytical model combining a fiber kinking compression model and the notch stress concentration will be presented to predict the strength of the Open Hole Compression (OHC). The numerical models are described based on the continuum damage modeling in combination with interlaminar cohesive model. The combined Hashin/Puck's criteria with Cohesive Zone Model (CZM) which used in this thesis can predict the load carrying capacity of the wrinkled specimens comparable with experimental results which be validated in the next chapters. The numerical FE model provides a vision by following the stress flow over ply levels of the laminate. The stresses when meet failure criterion illustrate failure mechanisms and their interactions.

In chapter 4 OHC and the Open Hole Tension (OHT) tests have been performed for evaluating the effects of out-of-plane fiber waviness in continuous fiber reinforced composites. A setup is designed focusing on the OHC kink band observations using synchronized acoustic emission with optical microscopy. Experimental, analytical and numerical approaches are used to incorporate the notch and waviness size effects on composite compressive and tensile strength.

The OHC material allowable presents a critical design value controlling the design of composite structures. An analytical model based on synthesizing orthotropic stress concentration factor and a generalized expression using traction continuity through the kink band is developed. Temporal evaluations of the load response, acoustic emissions and optical microscopy are used to understand the failure modes in the specimens considered and their relationship to the load drops observed during the test. The numerical simulations are described and the results presented and discussed, as they proved to be the major source of information for the achievement of the project's goal. The combined Hashin/Puck's with CZM model which used in this thesis can predict the load carrying capacity of the wrinkled specimens comparable with experimental results. The numerical FE model provides a vision by following the stress flow over ply levels of the laminate. The stresses when meet failure criterion illustrate failure mechanisms and their interactions.

Chapter 5 is devoted to proposing a new method determining the limit point in composite materials which can be used to design considerations of laminated composite structures. The limit point is proposed based on the z-displacement or out-of-plane displacement tracking using an image correlation method to determine the start of incipient interlaminar delamination in continuous fiber reinforced composite materials. The maximum principal strain is used to identify the hot spot stress location for construction of an evaluation line. The z-displacement along this evaluation line is then tracked as the specimen is loaded. Differentiation of the z-displacement field results in peaks that are subsequently used to identify the limit point of the composite material. In Chapter 6, a structural application linking Chapters 3 (modeling) and 4 (experiments) focuses on using a Hyperspectral Near Infrared Imaging (NIR) method to model and predict the behavior of composites with waviness defects. It is proposed to use NIR hyperspectral imaging and progressive damage finite element analysis for advanced distributed damage characterization

in composite structures. Our approach overcomes the obstacles facing accurate mechanical analysis of the structure as it is built without simplifying assumptions of defect levels. A finite element mesh generation technique with the capability of meshing layers separately has been developed to transform the resin thickness maps to a finite element mesh with a ply-by-ply representation including cohesive layer failure interfaces in between the plies. The proposed method is demonstrated on a continuous plain weave fabric carbon fiber/epoxy laminate.

Chapters 7 presents the main conclusions of this thesis and suggestion for further research.

# CHAPTER 2
# LITERATURE REVIEW

This chapter contains a literature review over the considered research objectives of the thesis including defect definition, failure mechanisms and engineering tools to identify them. Firstly, the damages are categorized based on manufacturing and in-service defects which may cause premature failures in composite laminates. Then an overview about the failure mechanisms associated with the laminated composites will be presented. The analysis of the failure are presented by exploring the previous significant studies regarding waviness geometry characterization, analytical and the finite element (FE) analysis of composite laminates containing fiber waviness defects. The defect identification tests will be explored by studying imaging and sounding approaches.

## 2.1 Damage Mechanisms in Fiber Reinforced Composite Laminates

Composite structures show several failure mechanisms occurring independently or interacting with each other, e.g. fiber crushing, matrix failure, delamination, or longitudinal splitting. Fiber waviness may be caused by non-uniform consolidation pressure, interactions with other layers or ply drop-offs. The waviness can typically affect all or some of the plies in a laminate stack. In all the test samples, cracking of the resin occurred at the waviness zone, but ultimate capacity was always greater than the crack initiation load. Fiber waviness (or sometimes called wrinkles, tiger or zebra stripes according to industrial vernacular) is one type of the common manufacturing defects encountered during the manufacture of composite structures (Figure 2.1). These defects as previously discussed can be part of the build process depending on the severity, the expected design loads and the locations where these defects occur.

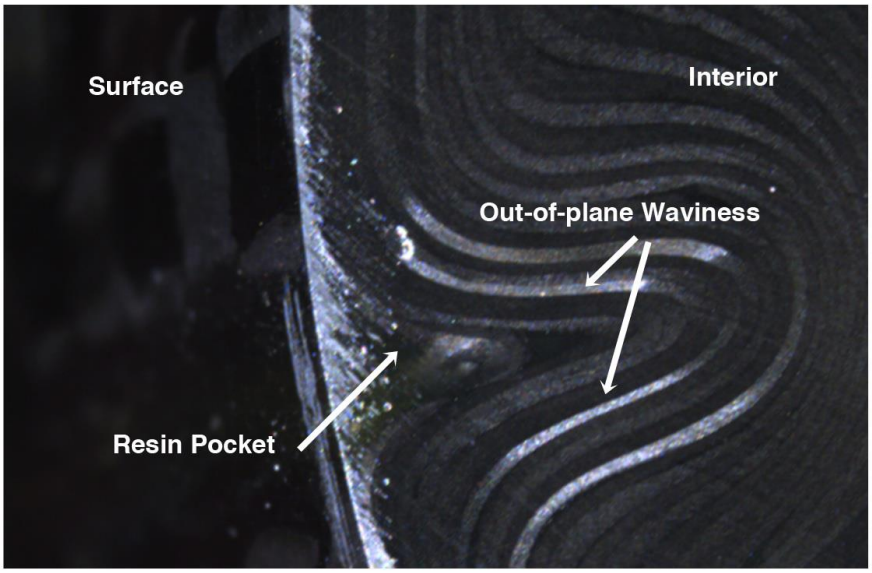


**Figure 2.1** Example of a severe fiber waviness profile in a composite structure[12]

Composite structures in aerospace applications are typically designed to carry the stress rise around notches and discontinuities. If waviness occurs at notch zones, the design capacity of the structure can be expected to further decline. It is not unreasonable to expect that in composite structures that waviness may occur anywhere including near holes, cut-outs or other geometrical discontinuities. For example, in a composite fuselage holes are used in bolted joints between structures such as frames or shear ties.

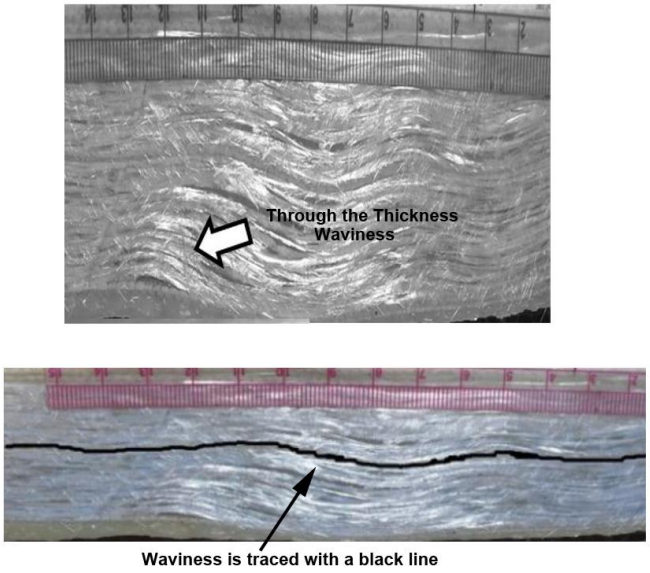


**Figure 2.2** Out of plane waviness seen through the thickness in a composite wind blade[8]

Figure 2.2 shows photographs of built flawed wind blade section cutting out to provide a cross section view of the skin and spar cap laminates illustrating out of plane waviness [8] . In some research, defects in composite structures have been demonstrated to affect the structural integrity and significantly reduce the strength and stiffness of the composite structure [11-14]. Damage can be derived by preexisting defects progressing to different failure mechanisms

including matrix cracking, inter/intra delamination and fiber breakage. The damage mechanisms are extremely dependent of the levels of anisotropy and inhomogeneity of the constituents where a multiplicity of damage mechanisms can degrade the material [22, 23]. As the composite laminates can be stacked in unidirectional or multidirectional sequences associated with different degrees of anisotropy, damage occurs as transverse cracking of the matrix, fiber matrix debonding, fiber breakage, fiber kinking, fiber splitting or interlaminar delamination (Figure 2.3).

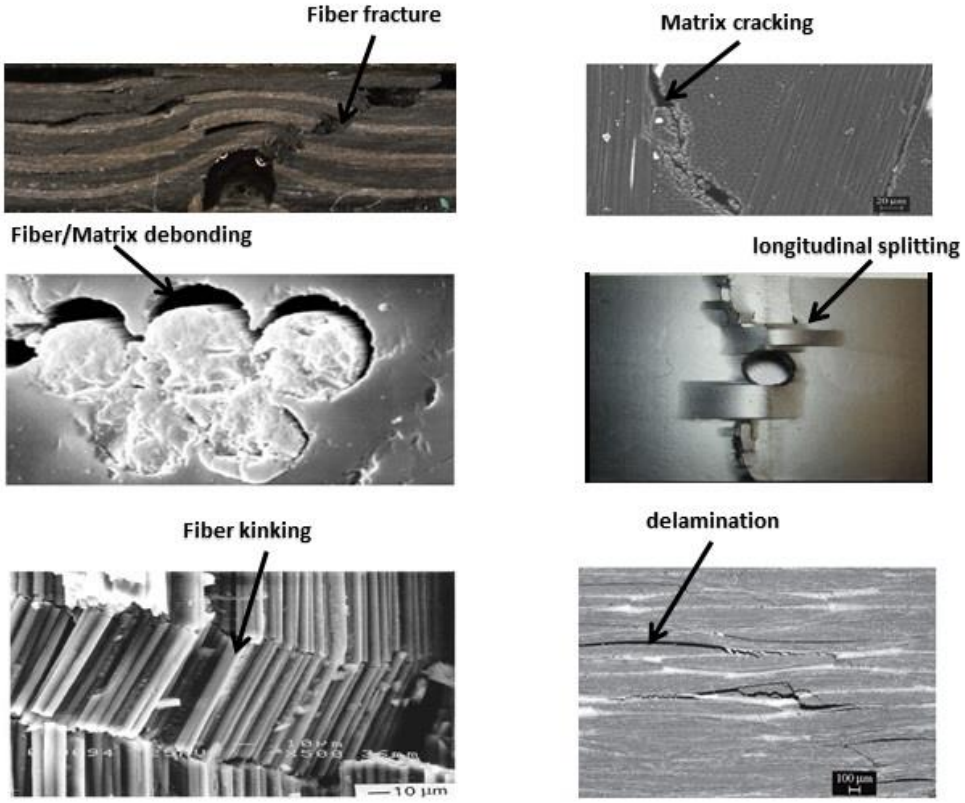


**Figure 2.3** Possible damage mechanisms in composite laminates [24, 25]

Beside the degrees of anisotropy, damage mechanisms can be derived by the applied loading conditions which are fundamental for evaluating the residual strength and life of composite structures. The damage progression can be altered through the load increasing as well as the number of cycles under fatigue loadings. Among the possible failures, matrix cracking is the first likely failure mode.

However matrix cracks at initial stages of applied load do not contribute to final failure, but result in degrading the material stiffness. By increasing the load, cracks can propagate and result in other failure modes. The crack initiation and propagation predictions are complex depending on parameters which cannot distinctively be defined. Therein the development of a general progressive damage model to predict damage initiation, damage growth and ultimate strength of composite laminates has not been proposed.

## 2.2 Effects of fiber waviness defects

The increased application of the fiber reinforced composite materials has resulted in a strong need to investigate the effects of defects associated with various manufacturing anomalies. Some of these defects that can occur include porosity, waviness, delaminations, and resin migration. However, when defects are present, whether a part is accepted for production or scrapped is dependent on the structural evaluation performed. Fiber waviness is considered as one of the most common types of defects encountered in manufacturing of composite structures[26, 27]. Fiber waviness in fiber reinforced composites commonly occurs due to three sources: pressure from other composite layers, residual stresses that can occur in the laminate from tooling, or when different layers of materials are co-cured in differing configurations [28-30]. A survey of the literature reveals significant interest in this topic, yet a large volume of work on compression properties in fiber reinforced composite does not consider the interactions between notches and fiber waviness. Such defects can serve as initiation sites for matrix cracking, fiber kinking, fiber/matrix debonding and delamination. Of the possible defects, ply-level out-of-plane waviness or wrinkling can lead to the highest degradation of mechanical properties [13, 18, 19, 31, 32] and is the most challenging of defects to detect using conventional approaches. Ply waviness can be

caused by wrinkles in bagging or non-uniform consolidation pressure, interactions with other layers or ply drop-offs. Processing parameters including length of cure, cooling rate, and tool plate material can also influence the development of wrinkles in the laminates [33, 34].

Fiber waviness can occur in both the in-plane and out-of-plane directions [35]. Several approaches have been proposed for characterization and measurement of out-of-plane fiber waviness. The ability of predicting the location and severity of the waviness before the composite part is cured is theoretically of great interest but limited success has been achieved. Micrographic assessment methods are capable of identifying the waviness but require destruction of test parts. The characterization of fiber waviness using optical microscopy of autoclave manufactured unidirectional panels has been previously reported [36]. Wisnom and Atkinson [37] artificially induced waviness in composite rings and were able to correlate the post-cure waviness levels using a displacement-based technique applied during the manufacturing stage. Potter et al. [31] showed that the influence of defects such as waviness must be explicitly included in determining allowable properties of composites. Bradley et al. [38] investigated methods to directly correlate experimentally determined strain fields and compressive strengths with analytical predictions. Their results showed that under compression loading, large interlaminar shear and normal strains occurred as a result of layer waviness.

The effect of the fiber waviness morphology on the tension and compression properties has been previously discussed [19, 20, 39] indisputably showing a link between the amplitude of the waviness to the degradation in properties [40]. Closed form methods have also been reported for prediction the compression strength based on the matrix dominated shear strength using the Puck failure criteria [41]. Compressive properties were also investigated and modeled for the effects of the wrinkle on the kink band formation [42]. Other studies have shown the interaction of fiber

waviness with stress concentrations showing even higher reductions in properties are observed [43]. However, most of these studies focus on compression and the ultimate stress conditions and have a limited discussion on the limit stress conditions, defect characterizations and damage evolution when such defects are present under mechanical loads.

### 2.3 Design of composite materials with fiber waviness defects

There is clear evidence of early failures in laminated composites during tension testing caused by wrinkles [12]. The results show interlaminar failures occur prior to the maximum load without a significant load drop that can be used to identify the early failure. Using optical video microscopy on the side of the specimen, it was possible to qualitatively identify the interlaminar damage. In a composite specimen this can clearly occur without a significant drop in the load-displacement response. This load drop in the response is normally used to study the onset of failure. However when there is no load drop observed in the load-displacement record, a non-conservative assumption of using the ultimate stress for characterization of the material system is typically used. Without the load drop it is not possible to accurately define the onset of failure in the composite material. Further, it is not always possible to monitor the specimens using a video microscope if the defect is not visible on the side (e.g. wrinkle does not extend to the edge) or if the specimen geometry precludes this from happening. Thus there exists a need in establishing standard methods for determining the limit point of fiber reinforced composite materials in the presence of typical composite manufacturing anomalies such as wrinkles.

The characterization of fiber waviness using optical microscopy of autoclave manufactured unidirectional panels has been previously reported [36]. Ampiah, N. et al. [44] investigated the effects of waviness imperfections on the circumferential stress of the retrofitted pipes. In all the

test samples, cracking of the resin occurred at the waviness zone, but ultimate capacity was always greater than the crack initiation load. The following section brings some important works which have been proposed to analyze the waviness in composites using finite element methods and closed form solutions.

## 2.4 Finite element and closed form solutions background

Flek et al. used a finite element couple stress formulation to predict microbuckle initiation from a patch of fiber waviness in a unidirectional fiber composite under remote compression and bending[45]. They predicted the strength of the wavy laminate different than kinking theory prediction which neglects the role of fibre bending. Garnich [46] investigated the effects of fiber waviness defects on properties of unidirectional fiber composites using a finite element micromechanics modeling at the constituent level. Davidson et al. [47] used a finite element model to show the influence of misalignment angle of the out of plane fiber waviness on strength knockdown of the carbon fiber unidirectional specimens. Schultheisz and Waas [48] concluded that FE analysis would be an excellent candidate to handle the 3D aspect of microbuckling. Compression testing is not a trivial task in continuous high strength and high modulus fiber reinforced polymer composites.

In compression loading, kinking models can assess the effects of waviness defects on strength. The elastic shear microbuckling model proposed by Rosen [49] predicts compressive strength in the absence of fiber initial misalignment. This model suggested the failure as an elastic shear bifurcation at an axial applied stress equal to the in-plane shear modulus:

$$X_c = \frac{G_m}{1+v_f} \qquad (2.1)$$

Where $X_c$ is the compressive strength, $G_m$ is the matrix shear modulus and $v_f$ is the fiber volume fraction. Many extensions and improvements have been performed to refine Rosen's model to predict initiation of microbuckling [50-52]. Argon [53] considered the initial fiber misalignment based on a model of microbuckling as a plastic collapse:

$$X_c = \frac{\tau_Y}{\bar{\varphi}} \qquad (2.2)$$

Where $\tau_Y$ is the composite shear strength and $\bar{\varphi}$ the initial fiber misalignment angle. Several researchers have also incorporated the imperfection geometry to a proposed kinking model [52, 54-57]. Budiansky [52] generalized Argon's equation to elastic perfectly plastic composite response as :

$$X_c = \frac{\tau_Y}{\gamma_Y + \bar{\varphi}} \qquad (2.3)$$

Where $\gamma_Y$ is defined as yield shear strain. Budiansky and Fleck [58] extended the Equation 2.3 to a more generalized expression using traction continuity through the kink band:

$$\sigma_\infty - 2\tau_\infty tan\beta = \frac{\tau - \tau_\infty + \sigma tan\beta}{\varphi + \bar{\varphi}} \qquad (2.4)$$

Where $\sigma_\infty$ and $\tau_\infty$ are remote stresses, $\varphi$ is the fiber rotation angle and $\tau$ and $\sigma$ are stresses through the kink band. $\beta$ is the kink band inclination angle shown in Figure 2.4.

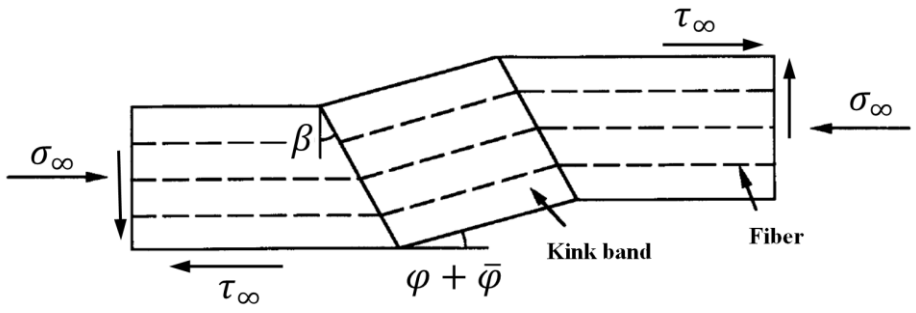


**Figure 2.4** Definition of the stresses under kink band formation

Hahn and Williams [57] developed a compressive failure model considering either the shear stress exceeding the composite shear strength or the fibers failing in bending. Berbinau et al. [55] considered a fiber as an Euler slender column which is supported by a nonlinear matrix. A follow-up study by Pimenta et al. [59] used a bending theory approach to obtain close form solution to kink strength and kink band formation. Even these models are shown to be capable to predict softening and fiber failure appropriately, but they are limited to low initial misalignment angles. Fleck et al. [60] investigated the microbuckle initiation from an open hole and from the free surface of a band of waviness in unidirectional fiber composite by using the finite element method. They concluded that pre-existing fiber waviness adjacent to the hole gives a further reduction in the compressive strength.

In development of the fiber waviness and kink-zone failures models we first consider an orthotropic laminate uniaxially loaded along the principal axis, *x*, having the maximum stress occurs at the hole boundary. The infinite, orthotropic stress concentration factor is given by [61]:

$$K_T^{\infty} = 1 + \sqrt{2\left(\sqrt{\frac{E_{xx}}{E_{yy}}} - v_{xy}\right) + \frac{E_{xx}}{G_{xy}}} \qquad (2.5)$$

Where $E_{xx}$, $E_{yy}$ and $G_{xy}$ are the effective longitudinal, transverse and shear elastic moduli and $v_{xy}$ is the Poisson's ratio. These moduli and the stress concentration factor can be used to relate the notched to the un-notched strength using the point stress criterion [62]:

$$\frac{X_n^{\infty}}{X_{Un}} = \left[\frac{2}{2+z^2-3z^4-\left(K_T^{\infty}-3\right)\left(5z^6-7z^8\right)}\right] \qquad (2.6)$$

Where $X_{Un}$ is the unnotched strength of the laminate, $X_n^{\infty}$ is the notched strength of an

infinite plate and $z = \frac{R}{R+d_0}$ . R is the hole radius and $d_0$ is a characteristic distance. $X_n^\infty$ can be related to $X_n$ by introducing a finite width correction factor containing circular holes [63]:

$$\frac{K_T}{K_T^\infty} = \frac{2+\left(1-\frac{2R}{w}\right)^3}{3\left(1-\frac{2R}{w}\right)} \qquad (2.7)$$

where $w$ is the width and the ratio of un-notched to notched strength can be expressed as a function of the geometry and the stress concentration factor [63]:

$$\frac{X_{Un}}{X_n} = (1 + \frac{1}{2}z^2 - \frac{3}{2}z^4 - \frac{1}{2}(K_T^\infty - 3)(5z^6 - 7z^8)(\frac{2+\left(1-\frac{2R}{w}\right)^3}{3\left(1-\frac{2R}{w}\right)}) \qquad (2.8)$$

## 2.5 Mechanical behavior characterization using standard tests

### 2.5.1 Tension and compression

The Open-Hole Compression (OHC) and Open-Hole Tension (OHT) test methods are typically used for determining the compression and tension strength allowable of continuous high modulus symmetric and balanced composites [64, 65]. The notch and the waviness affect the stress field at the combined imperfection zone in the OHT and OHC tests. The failure mechanisms can be considered a structural test having complex interactions between local failures and structural instabilities[66]. The failure mechanism interactions make the compression tests very sensitive to geometry perturbations or defects such as out of plane fiber waviness or porosity.

In the compression test, several failure mechanisms can occur independently or interact which each other, e.g. fiber crushing, matrix failure, delamination, longitudinal splitting and fiber kinking. However, in composite structures, these defects can occur anywhere including near holes, cut-outs or other geometrical discontinuities. For example, in a composite fuselage holes are used

in bolted joints between structures such as frames or shear ties and many times designers cannot preclude with all certainty the presence of waviness defects in those locations. Further, the stress concentration associated with these holes is usually the driving factor in design. For this reason, the Open-Hole Compression (OHC) test method is typically used for determining the compression properties (such as compression strength allowable) of continuous high modulus symmetric and balanced composites [64].

In the OHC test, a notched specimen is face supported using a multi-piece bolted support fixture. This test method has proven its ability to capture the effects of notches under compression loads. The use of OHC allowable is critical in the context of the move towards large and built-up composite parts containing holes or circular cutouts. Despite the success of using the OHC specimen in capturing the effects of notches, the specimens for the OHC allowables are usually manufactured in environments that are not typical to the actual manufacturing conditions of the composite structure. Thus, it maybe advantages to incorporate these defects directly into the OHC specimen to produce modified strength allowable.

### 2.5.2 Flexural behavior

Wisnom [67] used a non-linear finite element analysis showing the same mechanism of shear instability due to fiber waviness occurring under pure bending as under pure compressive loading. Through the thickness stresses which are originated in the stress gradient in carbon/epoxy laminates increase the maximum compressive strength in bending in comparison with pure bending [67]. This phenomenon is more significant for thin specimens, where the stress gradient is high, while in thick laminates, the maximum compressive stress in bending tends towards the value in pure compression. As the thickness decreases, the bending stress increases due to the

constraint of the adjacent less highly loaded fibers. Winson [67] discovered the predicted maximum stress in bending was up to 73% higher than in compression. The results show that where failure is controlled by shear instability due to fiber waviness, compressive strength can be expected to be a function of stress gradient and therefore cannot be regarded as a true material property.

Mandell et al. [68] investigated the effect of through thickness waviness on carbon fiber laminates and hybrids indicating that a severe loss about 60% of the control range in compressive strength and ultimate strain are possible with carbon prepreg. Allison et al [69] experienced 37% reduction in strength compared to a flat specimen in large concave up waves cases under three-point bending tests for S-glass/epoxy composites. The dominant failure mode for unidirectional wavy composites under bending was shown to be interlaminar shear, which in turn leads to microbuckling. In compression loading, kinking models can assess the effects of waviness defects on strength.

It is noteworthy to mention that mechanical properties provided in material datasheets are often obtained via uniaxial tests at quasi-static rates while flexural bending tests showing disparate responses than the axial tension or compression. Hallett [70] used a statistical approach demonstrated that fiber reinforced composites respond a notably higher tensile strength in the bending mode compared to standard axial tension. Ardakani et al. and Papdakis et al. [71, 72] raised the tensile and shear properties by 40% to take the effect of bending stress into account. Santiuste et al.[73] increased the quasi-static tensile strength by 40% in order to account for the effect of bending mode and established matching between experiments and numerical results of composite laminated beams.

## 2.6 Waviness geometry characterization

Despite mathematical expressions and numerical modeling, experiments are necessary to describe the damage evolution, the stiffness changes and symmetry loss in composite laminates in practice. The common experimental tools have been used widely such as strain gauges [74, 75] photoelasticity and digital image correlation (DIC). Fundamentally DIC is an optical method that employs tracking and image registration techniques for accurate 2D and 3D measurements of changes in images. This is often used to measure deformations, displacements, strains in the solid mechanics application. Nondestructive testing techniques such as acoustic emission (AE) and ultrasonic testing (UT) can be used to detect defects as well as for the characterization of damage progression in composite materials[76]. Delamination as a common defect derived by in-service and manufacturing in carbon fibre reinforced plastic (CFRP) components, can be detected by ultrasonic (UT) method.

Current analysis methods for composites with defects are limited by the ability of nondestructive methods to adequately and economically characterize the defect levels in the structure. Sutcliffe et al. [77] used an X-ray image analysis technique to determine the fiber waviness. This technique provided good agreement with results from the polished prepreg samples. Prepreg is a fibrous material pre-impregnated with a particular synthetic resin, used in making reinforced composite laminates. Similarly, Nikishkov et al. [78] proposed a method for automated generation of finite element meshes for unidirectional composites with waviness defects using X-ray computed tomography. Pain et al. [79] used an ultrasonic array to extract the scattering of the interior of the composite structure. Pulsed terahertz response of the composite is shown to provide clear indications of the fiber waviness [80] but characterization of wrinkle levels continues to be an area of concern and is likely to be limited by a variety of factors such as the stacking

sequence and the thickness of the structure in question. Ultrasonic characterization methods are difficult to interpret because elastic wave propagation is highly dependent on stacking sequence effects and interactions with other defects, such as porosity, which can occur at the same time as wrinkle defects. The computed tomography methods previously discussed are limited to testing specimens of small sizes and are currently not practical for many types of composite structures.

In the absence of reliable stochastic or multi-physics models that account for manufacturing, it is not possible at this point to accurately predict the locations where defects occur before manufacturing. Even if the wrinkle defect is visible, it is not currently possible to reliably determine its depth non-destructively using methods that are commonly used, such as ultrasonic inspection. In other cases, excess resin on the composite surface might result from a wrinkle in the bagging material, so there is no underlying composite feature. NDI methods based on ultrasound can detect resin pockets in excess of 1000 microns but cannot accurately measure pockets that are less than 1000 microns deep. Thermoelastic stress analysis methods have also been proposed to identify resin pockets and wrinkles, but these require a cyclic application of load [81]. Thus there exists the need for robust, portable and accurate methods for providing identification and depth measurement of wrinkles in composite structures.

Chemometric data processing methods can be used to characterize the relationship between the spectra and the resin thickness and provide the correlation to predict a point-by-point local resin thickness and thus produce thickness maps of the scanned resin surface. Recent advances in hyperspectral near infrared (NIR) sensing and data processing technologies have made real-time infrared methodologies a viable solution for accurate analysis of composite structures. NIR imaging can accurately measure surface resin on composite materials from 125 to 2500 microns thick, detecting virtually all resin pockets, resin-filled surface wrinkles and other surface resin

features [82]. The resin-rich areas on the surface are usually an indicator that wrinkles are affecting some or all of the plies in a laminate stack.

### 2.6.1 Gaussian function characterization

The characterization parameter of the fiber waviness is necessary in order to capture the level of waviness and its relation to the open-hole tension strength. The simplest of the approaches to characterize the fiber waviness involves taking a ratio of the waviness length to the waviness height, $A_w$. This approach can be problematic in the sense that the definition of the length of the waviness is subject to the interpretation of the individual characterizing the waviness morphology. The out-of-plane uniform fiber waviness has been also characterized by assuming it to be planar sinusoidal in the x-z plane with the amplitude as by Hsiao and Daniel[39]:

$$v(x) = A_w sin\frac{2\rho x}{L} \qquad (2.9)$$

The out-of-plane waviness geometry for the morphology can also be characterized by means of a Gaussian function to capture the bell-curve response of the wavy plies. The Gaussian function can also be used to characterize the behavior from certain morphologies of given defects[12]. Figure 2.5 presents a photograph of the waviness defects produced in this study where the waviness more resembles the Gaussian function.

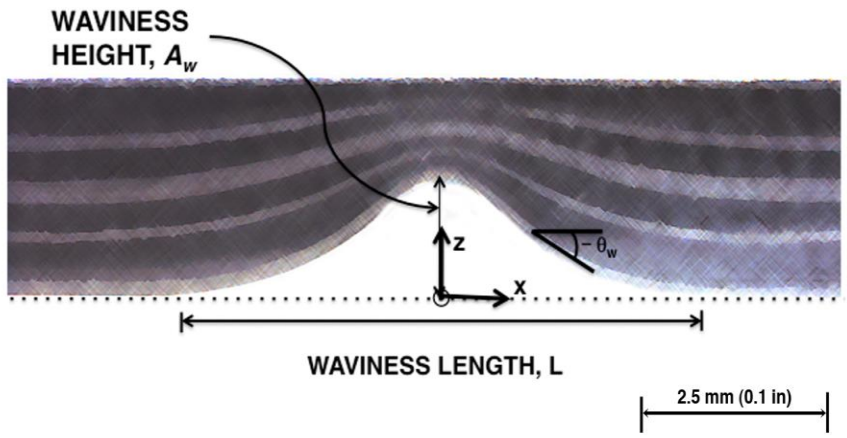


**Figure 2.5** Photograph of through thickness waviness defects[12]

Gaussian functions are widely used in statistics, signal processing and image processing. Since these analytic functions are differentiable, they can be used to determine the angle of the waviness and hence can be used in transformation of elastic constants if necessary. This Gaussian function is a characteristic symmetric "bell curve" shape that quickly falls to plus/minus infinity. The parameter *A*, is controlled by the height of the curve's peak or the height of the waviness parameter, *b*, is the position of the center of the peak, $e$ is Euler's number, and, *c*, controls the width of the bell curve[39]:

$$f(x) = A\, e^{-\frac{(x-b)^2}{2c^2}} \qquad (2.10)$$

Thus, for the case of uniform waviness the z-coordinate along the x-axis, $v\left(x\right)$ becomes:

$$v(x) = A_w\, e^{-\frac{x^2}{2c^2}} \qquad (2.11)$$

where $b = 0$, for a centered curve at the $x = 0$ position. The Gaussian function fit to the experimental measurements obtained using an image from an optical microscope for a specimen is shown in Figure 2.6.

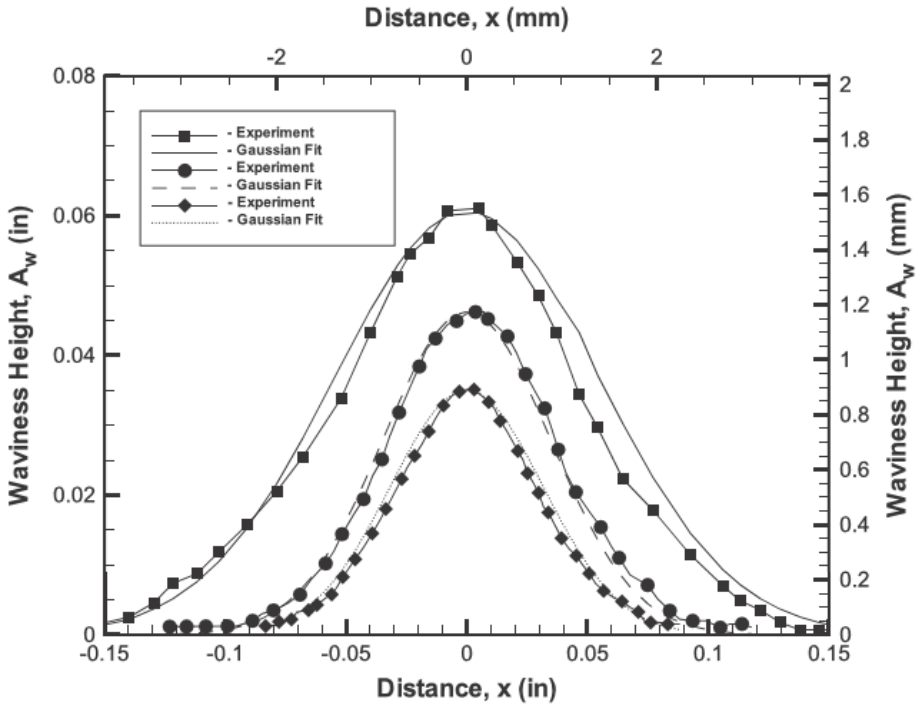


**Figure 2.6** Gaussian functions with experimental measurements from optical measurements[12]

The waviness measurements were made using image analysis of the captured morphologies using an optical microscope. Note that the Gaussian function is independent of the length of the waviness profile which is important since there can be a great amount of subjectivity when defining the length of the defect.

### 2.6.2 Imaging methods

The increased use of image correlation methods made possible by advances in theory and cost reduction of equipment have extended the use of such coupled methods for composite material characterization[83-86]. Several researchers have studied the deformation and failure behavior of composite materials using digital image correlation methods. Shearography has been successfully used for qualitative measurement of wrinkles in wind turbine blades [87]. Goidescu et al. [88] used a coupled digital image correlation, infrared thermography and X-ray tomography approach to study the failure of CFRP composites in a qualitative approach observing material anisotropy and failure aspects. Johanson et al. [89] used the Lagrangian strains from DIC to study the architecture and failure in discontinuous carbon fiber composites formed from randomly orientated bundles and to map the evolution of the failure.

Digital image correlation (DIC) techniques have been increasing in popularity, especially in micro- and nano-scale mechanical testing applications due to its relative ease of implementation and use. Many of the Digital image correlation (DIC) procedures available are based on correlation image velocimetry methods directly inspired from earlier developments in fluid mechanics[90, 91]. DIC has been used in solid mechanics applications [92, 93]. By using a CCD camera, pictures of speckled specimens at different stages are recorded during the test. The specimen is usually coated by a random black and white pattern. Sometimes the natural texture of the observed surface is sufficient to use the technique with no coating. The in-plane displacement map is computed with a correlation technique between an initial picture and a subsequent one[94]. Two-dimensional DIC uses one image sensor and is suitable for applications that are not subject to out-of-plane motions. Three-dimensional DIC uses two image sensors to track surface displacements in three dimensions.

The DIC technique has the advantage of being applied to any class of material; it requires no heavy specimen surface preparation and the optics involved are quite simple. No fringe analysis and phase unwrapping are needed in this method and also there is no fringe density limitation which makes the DIC measurement range much larger than the other technique. Moreover, it is truly a non-contact by nature and provides full field data[95]. In filament-winding application, Henry et al. [96] used a 2D DIC method to study the behavior in unidirectional and cross-ply laminates. The observations of strain on the free edge revealed that fiber undulation caused elevated out-of-plane shear and through-thickness normal strains in regions eventually involved in the fiber micro-buckling failure process. Makeev et al. [97] tested thick section carbon-epoxy multidirectional laminates using DIC to measure the strains and used the nonlinear shear behavior to predict the failure load. A limit point can be defined as a point of transient phase passing from elastic response. Prior to this limit point, the material will deform elastically and will return to its original shape when the applied stress is removed. However, once the limit point is passed, some fraction of the deformation will be permanent and non-reversible and is caused by interlaminar delaminations and separation of the material.

This is particularly an issue in a layered medium where the out-of-plane response is primarily matrix dominated. The knowledge of the limit point is thus vital when designing a component since it represents an upper limit to the load that can be applied during normal operating conditions. Current test standards [98] used to determine the tension properties of laminated composites do not directly consider the presence of defects in the composite material or how this may affect the limit loads. Further, as previously stated the identification of this limit point is complicated by the fact that the limit load is not directly observable during a standard tension test [99-102].

Current analysis methods for composites with defects are limited by the ability of nondestructive methods to adequately and economically characterize the defect levels in the structure. Sutcliffe et al. [77] used an X-ray image analysis technique to determine the fiber waviness. This technique provided good agreement with results from the polished prepreg samples. Similarly, Nikishkov et al. [78] proposed a method for automated generation of finite element meshes for unidirectional composites with waviness defects using X-ray computed tomography. Pain et al. [79] used an ultrasonic array to extract the scattering of the interior of the composite structure. Pulsed terahertz response of the composite is shown to provide clear indications of the fiber waviness [80] but characterization of wrinkle levels continues to be an area of concern and is likely to be limited by a variety of factors such as the stacking sequence and the thickness of the structure in question. Ultrasonic characterization methods are difficult to interpret because elastic wave propagation is highly dependent on stacking sequence effects and interactions with other defects, such as porosity, which can occur at the same time as wrinkle defects. The computed tomography methods previously discussed are limited to testing specimens of small sizes and are currently not practical for many types of composite structures.

### 2.6.3 Sounding methods

Acoustic emissions are stress waves associated with micro-structural changes in the material [103]. AE techniques have been extensively used for the analysis of failure modes in composite material where the total strain energy is dissipated as a wave propagating from the failure source through the medium. The AE analysis has been previously used to investigate fiber breakage, matrix cracking and interlaminar debonding [104, 105]. Qamhia et al. [106] showed that AE can be used to detect damage associated with fiber waviness provided the porosity levels

are low. The number of hits, cumulative energy and amplitude has been the most widely adopted parameters for describing and characterization of damage in composites materials[34].

Ultrasonic testing can be shown with high sensitivity to all defects in composite laminates[107]. This technique is based on specifying the transmitted wave reflection result in any changes in material acoustic impedance. The velocity and absorption of ultrasonic waves propagated in the medium is measured with the same or another transducer. A common technique is immersion testing where the transduced is coupled to the specimen with water. The mechanical waves travel through the material with some loss of energy, and are deflected at interfaces and/or defects. The deflected beam can be displayed and analyzed to assess the presence and location of flaws or discontinuities. Apart from microstructural changes, the acoustic characteristics of a material can also be influenced by degradation being a result of accumulated micro-damages caused by working conditions put on the structure. The "A" scan identifies the giving time of flight and reflection amplitude data. The "C" scan display a pictorial plan view of the defects detected. Wróbel[108] attempted to determine dependencies between the degree of load capacity degradation and the changes in characteristic of an ultrasonic wave passing through a composite material. Potel et al. [108, 109] presented some ultrasonic methods to detect and to characterize defects, possibly obtained after damage caused in composite materials.

Generally, through transmission and pulse echo approaches to the ultrasonic testing are the most popular in the non-destructive evaluation of materials. In through-transmission test, two transducers can be placed at each side of the material. In the case where only one side is accessible, both transducers or one transmitter-receiver transducer is located on that side and a pulse-echo technique is used [110]. The choice of the most appropriate technique mainly depends on specific application with particular regard to the materials specifications and requirements of the quality

control process. A comparison has been shown by [111] that the results obtained for the wave velocity from pulse-echo and through transmission are in good agreement, indicating that both techniques can be considered as a quantitative non-destructives tools of local fiber content evaluation.

# CHAPTER 3

# ANALYTICAL AND NUMERICAL ANALYSIS APPROACH

This chapter describes numerical and analytical approaches which will be used in this thesis. A synthesized analytical model combining a fiber kinking compression model and the notch stress concentration will be presented to predict the strength of the OHC. The numerical models are described based on the continuum damage modeling in combination with interlaminar cohesive model. The combined Hashin/Puck's criteria with Cohesive Zone Model (CZM) which used in this thesis can predict the load carrying capacity of the wrinkled specimens comparable with experimental results which be validated in the next chapters. The numerical FE model provides a vision by following the stress flow over ply levels of the laminate. The stresses when meet failure criterion illustrate failure mechanisms and their interactions.

### 3.1 Analytical closed-form approach

Budiansky and Flek [58] proposed a compressive failure model that included the inclined kink band which induces transverse stresses at the initiation of kinking and presented a combined stress plasticity law using a quadratic yield condition:

$$\left(\frac{\tau}{\tau_Y}\right)^2 + \left(\frac{\sigma_T}{\sigma_{TY}}\right)^2 = \left(\frac{\tau_e}{\tau_Y}\right)^2 \qquad (3.1)$$

Where $\tau \; and \; \tau_e$ are the shear and the effective shear stress, where in yield condition $\frac{\tau_e}{\tau_Y} = 1$. $\tau_Y$ and $\sigma_{TY}$ are defined as the in-plane shear plastic yield strength at a corresponding strain assuming a perfect plasticity material response and the plain strain yield strength in a pure transverse tension response. The maximum compressive stress can be expressed by [112]:

$$X_C = \frac{\sqrt{1+(\sigma_{TY}/\tau_Y)^2 tan^2\beta}\,\tau_Y}{\bar{\varphi}+\varphi} - \frac{1}{\alpha}\tau_Y(\sigma_{TY}/\tau_Y)^2 tan\beta \qquad (3.2)$$

Where $\beta$ and $\varphi$ are the kink band inclination and kinking angles. $\alpha$ can be defined as $\sqrt{1+(\sigma_{TY}/\tau_Y)^2 tan^2\beta}$. In the case of elastic-plastic strain hardening behavior where a Ramberg–Osgood law can describe the shape of the shear stress versus strain curve for typical engineering composites, this equation can be written as [58]:

$$X_c = \frac{(1+\left({}^{\sigma_{TY}}/_{\tau_Y}\right)^2 tan^2\beta)G}{1+n(3/7)^{1/n}\left[\frac{\bar{\varphi}}{(n-1)\left(\gamma_Y/\sqrt{1+\left({}^{\sigma_{TY}}/_{\tau_Y}\right)^2 tan^2\beta}\right)}\right]} \tag{3.3}$$

where the shear strain, $\gamma_Y$, equals approximately 1% and the strain-hardening exponent, n is in the range 3–10 [113]. In the presence of large amplitude fiber waviness, once the matrix fails the fibers lose their support and break as a consequence. The benefit of the failure model in Equation 3.3 is that it separates the formation of kink bands from fiber failure [114]. Flek et al. [45] predicted compressive strength in composite with a large amplitude waviness where the bending moment created by the high amplitude fibers affected the asymmetric shear stress across the element at the kink band.

The predicted strengths for the case of an infinite band of waviness based on the Budiansky model shows a minor deviation between the initiation and band broadening stress level even for large initial misalignment[45]. They concluded that for the waviness less than 10°, the compressive strength decreases with increasing$\bar{\varphi}$, and for larger values, the strength asymptotes to a constant value [45]. The lock-up effect vanished in large waviness beyond a critical misalignment value of 14°. The use of Budiansky kinking model [58] is justified in this study since we are investigating relatively large misalignment angles. Therefore as the high amplitude waviness shortens the softening process that takes place after the peak load is reached, elastic perfectly plastic characterization of the matrix is considered a reasonable assumption. By combining Equations 3.1 and 3.3 and Equation 2.8, the composite compressive strength, $X_C$ as a function of the stress concentration factor and fiber waviness misalignments can be expressed as:

$$X_C = \frac{(1+(\sigma_{TY}/\tau_Y)^2 tan^2\beta)G}{1+n(3/7)^{1/n}\left[\frac{\varphi_0}{(n-1)\left(\gamma_Y/\sqrt{1+(\sigma_{TY}/\tau_Y)^2 tan^2\beta}\right)}\right]}\left((1+\frac{1}{2}z^2-\frac{3}{2}z^4-\frac{1}{2}(K_T^{\infty}-3)(5z^6-\right.$$

$$\left.7z^8)(\frac{2+\left(1-\frac{2R}{w}\right)^3}{3\left(1-\frac{2R}{w}\right)})\right) \qquad (3.4)$$

## 3.2 Numerical Analysis Approach

Determining the onset and propagation of delamination are critical for an accurate structural integrity assessment of composite structures. Significant progress has been achieved in developing numerical approaches and underlying constitutive models for initiation and propagation of specific damage modes. Intra-ply damage modes have been investigated primarily within the framework of Continuum Damage Mechanics (CDM)[115] while delamination has been studied extensively using interface fracture modeling techniques such as cohesive zone models[116] and virtual crack closure techniques (VCCT)[117] .

### 3.2.1 Continuum Damage Mechanics (CDM)

Continuum damage mechanics approach has been proposed to predict damage initiation and propagation in bulk material. The structural stiffness degradation is used to characterize damage onset and failure. As composites possess near brittle response to applied mechanical loadings, the nonlinear deformation can be neglected in this approach. The material response can be expressed by[118]:

$$\sigma = \begin{bmatrix} \frac{(1-d_f)}{D}E_1 & \frac{(1-d_f)(1-d_m)}{D}v_{21}E_1 & 0 \\ \frac{(1-d_f)(1-d_m)}{D}v_{12}E_2 & \frac{(1-d_m)}{D}E_2 & 0 \\ 0 & 0 & \frac{(1-d_s)}{D}G \end{bmatrix}[\varepsilon] \qquad (3.5)$$

D in the elasticity matrix is defined as $1-(1-d_f)(1-d_m)v_{12}v_{21}$and $d_f$, $d_m$and $d_s$show the state of damage for fiber, matrix and shear respectively. The elasticity matrix representing the failures defined by four modes including fiber fracture in tension, fiber micro-buckling in compression, matrix cracking under transverse tension and shearing and matrix crushing under transverse compression and shearing. $d_f$, $d_m$and $d_s$ are derived from damage variables $d_f^c$,$d_f^t$, $d_m^c$ and $d_m^t$as:

$$d_f = \begin{cases} d_f^t & if \quad \hat{\sigma}_{11} > 0 \\ d_f^c & if \quad \hat{\sigma}_{11} < 0 \end{cases} \qquad (3.6)$$

$$d_m = \begin{cases} d_m^t & if \quad \hat{\sigma}_{22} > 0 \\ d_m^c & if \quad \hat{\sigma}_{22} < 0 \end{cases} \qquad (3.7)$$

$$d_s = 1-(1-d_f^t)(1-d_f^c)(1-d_m^t)(1-d_m^c) \qquad (3.8)$$

Where $\hat{\sigma}_{11}$ and $\hat{\sigma}_{22}$ are components of the effective stress tensor.

### 3.2.2 Cohesive Zone Model (CZM)

The basic concepts of Cohesive Zone Model (CZM) were presented by Barenblatt [119]. The CZM principle was implemented in the finite element framework by Hillerborg et al [120]. The interface in CZM is modeled as a constitutive behavior specified by a traction-separation relationship. The CZM approach assumes that a cohesive damage zone, or softening plasticity, develops near the crack tip. The derivation and finite element implementation of the cohesive damage model are described in [116]. A brief description of the kinematics and constitutive damage models is presented. In a CZM model, a constitutive law for the interface relates traction,$T$, to the distance jump between two surfaces of the crack, $\delta$, by a structural operator, C, on a plane of separation (defined a priori):

$$T = C\delta \tag{3.9}$$

The energy dissipated in the process of fracture at final fracture displacement $\delta_f$ is computed by:

$$\int_0^{\delta_f} \mathrm{T}\mathrm{d}\delta = \mathrm{G_C} \tag{3.10}$$

Where, $\mathrm{G_C}$ is the area under the curve defined by equation that represents the energy required for complete failure of the interface. Figure 3.1 shows the failure modes in pure traction-separation laws.

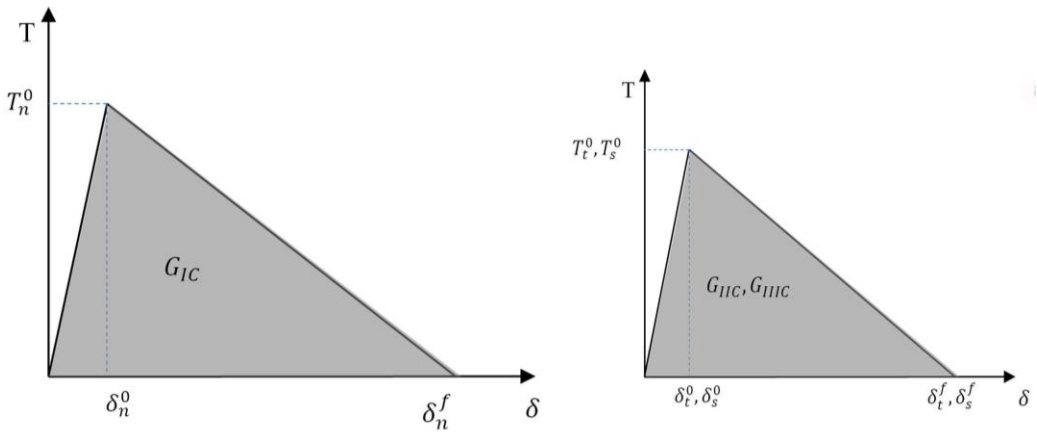


**Figure 3.1** Traction-separation law under pure mode I and II and III[121]

Traction-separation laws are described by using a damage initiation criterion and a damage evolution law. There are various criterions using an interaction between the components of tractions or displacements in different modes to predict crack initiation. These criteria are governed by the energy release rate components. The interfacial tractions for the normal ($T_n$), transverse ($T_t$) and shear modes ($T_s$) are:

$$T_n = \frac{\partial \emptyset}{\partial \delta_n}, T_t = \frac{\partial \emptyset}{\partial \delta_t}, T_s = \frac{\partial \emptyset}{\partial \delta_s} \qquad (3.11)$$

where $\emptyset$ is the potential function of the cohesive zone. The value of interfacial separation at the point of damage initiation is, $\delta^0$. At a value of displacement,$\delta^f$, damage is completed and beyond this point the interfacial traction remains zero. The pure separation modes in the normal $T_n^0$ , transverse, $T_t^0$, and shear, $T_s^0$directions of the contact stress at damage initiations are shown in Figure 3.1. Consequent evolution represents the rate of the damage propagations after initiation. A general frame work as described for the bulk material damage evolution is defined here as:

$$t_i = (1 - D)\overline{t_i} \qquad (3.12)$$

where "D" evolves from 0 to 1 upon further loading after initiation of damage, *i* can take n, s and t as representatives of $\overline{t_n}$, $\overline{t_s}$ and $\overline{t_t}$ defining contact pure stress components in normal, shear and transverse directions at the point of separation. It is obvious that at pure mode I, the separation is arrested. This is a model that is currently implemented in the ABAQUS [122] and is based on formulations proposed by Camanho [123].

### 3.2.3 Mixed-mode modeling

A cohesive surface interaction has been applied between two main sub component layers. A 3D composite material with continuum damage model within ABAQUS [122] finite element software are used to model the crack initiation.The simulation of progressive delamination using cohesive elements uses the concepts of damage, softening and fracture mechanics. This approach need not have an initial crack thereby allowing the possibility to predict the onset and propagation of a crack in the cohesive zone. In a finite element model using the cohesive interaction model, guidelines have been proposed for selecting element size, stiffness and strength of the cohesive zone. Turon et al. [124] proposed a procedure which accounts for the size of a cohesive finite element and the length of the cohesive zone to ensure the correct dissipation of energy;

$$l_{cz} = \frac{ME_2G_C}{\tau^2} \qquad (3.13)$$

In Equation 3.13, $E_2$ is the transverse Young modulus of the material for the case of orthotropic materials with transverse isotropy, *Gc* is the fracture energy release rate, $\tau$ is the maximum interfacial strength, and *M* is a parameter that depends on each model. Hilerborge showed that M can be considered as approximately 1.0. The number of elements in the cohesive zone is obtained with the equation:

$$N_e = \frac{l_{cz}}{l_e} \tag{3.14}$$

Where $N_e$ is the minimum number of elements needed in the cohesive zone and $l_e$ is the number of element in the direction of the crack propagation. It is possible to choose a strategy to adapt the length of the cohesive zone to a given mesh size by adjusting the maximum interfacial strength. Diehl [125] developed a novel penalty methodology for enhancing the use of the cohesive-zone method (CZM) in finite element models. Finite element implementations of the virtual crack closure technique and interface cohesive behavior have been successfully used to predict the failure in composite structures. For mixed mode damage growth the following propagation criterion are integrated within the modeling framework for the total critical strain energy release rate, $G_{TC}$, [126], [127]:

$$G_{TC} = G_{Ic} + (G_{IIc} - G_{Ic}) \left(\frac{G_{shear}}{G_T}\right)^{\eta} \tag{3.15}$$

Where $G_{Ic}$ is critical mode-I strain energy release rate, $G_{IIc}$ is the critical mode-II strain energy release rate. $G_{shear}$ is the shear energy release rate in a mixed mode loading case which can be expressed by the summation of the first and the second shear directions (usually are the same). $G_T$is the total energy including shear and normal energies. $\eta$ is a cohesive property which the criterion provides a good fit to the delamination initiation results for carbon-fibre/epoxy

composites with taking the value of 1.55 [127]. In the modeling approach, a cohesive behavior at the interface of the plies is used to simulate the delamination between layers on the scratch region. This model does not contain any pre-existing cracks. It uses the same toughnesses and strengths in modes II and III. Figure 3.2 illustrates the damage initiation and evolution when a mixed-mode traction-separation response with isotropic shear behavior is dominated in the analysis. The mixed mode traction can be defined as:

$$\left(\frac{\langle T_n \rangle}{T_n^0}\right)^2 + \left(\frac{T_t}{T_t^0}\right)^2 + \left(\frac{T_s}{T_s^0}\right)^2 = 1 \qquad (3.16)$$

In this equation, the brackets <> are the Macaulay brackets notation.

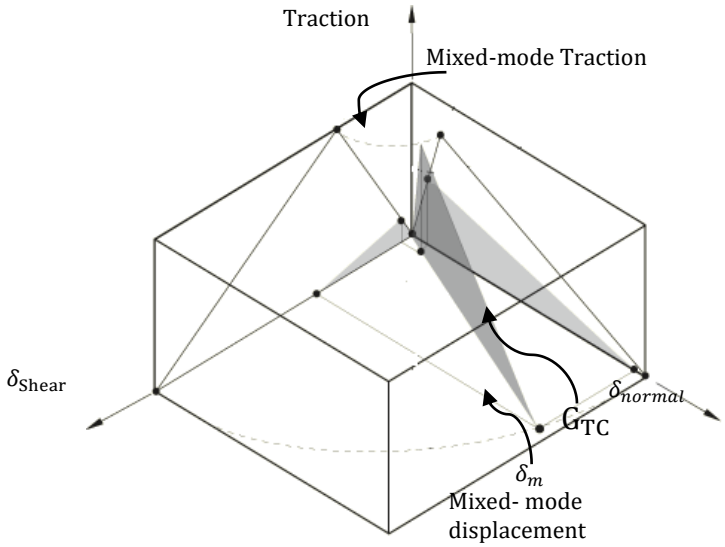


**Figure 3.2** Mixed-mode responses in cohesive interactions[128]

$\delta_m$ in Figure 3.2 shows the effective displacement under the mixed-mode conditions as;

$$\delta_m = \sqrt{\langle\delta_n\rangle^2 + (\delta_t)^2 + (\delta_s)^2} \qquad (3.17)$$

This modeling approach is used after confirmation with experimentally observed behavior of the crack path in the crack region. The continuum damage analysis model relies on a combination of Hashin's failure criteria [129] and Puck's action plane theory [130]. The validity of these theories against experimental results have been previously documented [131].

The damage progression model of this approach containing the Hashin's criteria and Puck's action plane models are implemented as a user subroutine, VUMAT [132]. In these models, the following are the definitions of the damage variables:

Tensile fiber failure: $\sigma_{11} \geq 0$

$$e_f^t = \left(\frac{\sigma_{11}}{F_1^{tu}}\right)^2 + \left(\frac{\sigma_{12}}{F_{12}^{su}}\right)^2 + \left(\frac{\sigma_{13}}{F_{13}^{su}}\right)^2 = 1 \qquad (3.18)$$

Compressive fiber failure: $\sigma_{11} \leq 0$

$$e_f^c = \frac{|\sigma_{11}|}{F_1^{cu}} = 1 \qquad (3.19)$$

The tensile matrix failures modeis: $\sigma_{22} + \sigma_{33} \geq 0$

$$e_m^t = \left[\left(\frac{\sigma_{11}}{2F_1^{tu}}\right)^2 + \frac{{\sigma_{22}}^2}{|F_2^{tu}.F_2^{cu}|} + \left(\frac{\sigma_{12}}{F_{12}^{su}}\right)^2\right] + \sigma_{22}\left(\frac{1}{F_2^{tu}} + \frac{1}{F_2^{cu}}\right) = 1 \qquad (3.20)$$

The compressive matrix failures mode is: $\sigma_{22} + \sigma_{33} \leq 0$

$$e_m^c = \left[\left(\frac{\sigma_{11}}{2F_1^{tu}}\right)^2 + \frac{{\sigma_{22}}^2}{|F_2^{tu}.F_2^{cu}|} + \left(\frac{\sigma_{12}}{F_{12}^{su}}\right)^2\right] + \sigma_{22}\left(\frac{1}{F_2^{tu}} + \frac{1}{F_2^{cu}}\right) = 1 \qquad (3.21)$$

In the above relations, the damage variables$e_f^t$ , $e_f^c$, $e_m^t$, $e_m^c$ are associated with the fiber and matrix in tension and compression failure modes respectively. When damage variables are met to one for each element, the element is removed.

$F_1^{tu}, F_1^{cu}$, and $F_2^{tu}, F_2^{cu}$, are the tensile and compressive failure stresses in fiber and transverse directions respectively and $F_{12}^{su}, F_{13}^{su}$ are corresponded to failure shear stresses in shear and transverse plane respectively. Transient dynamic models using an explicit FE solver were used to improve solution robustness and convergence during the failure progression [122].

These two methodologies are implemented within an explicit finite element analysis for modeling the waviness damage effects. To take the all shear stress components into account, 3D elements allow specifying the transverse shear effects in the out of plane direction of each ply.

# CHAPTER 4

# TENSION AND COMPRESSION BEHAVIOR

The OHC and OHT tests have been performed for evaluating the effects of out-of-plane fiber waviness in continuous fiber reinforced composites. A setup is designed focusing on the Open Hole Compression (OHC) kink band observations using synchronized the loading machine, acoustic emission and the microscope. In another experimental setup consisting of a pair of digital cameras observing the surface of a multidirectional carbon-epoxy specimen loaded in tension to measure deformations leading to discovering a new method for the limit point determination in the next chapter. The proposed test setup uses the OHC and OHT specimens with controlled levels of fiber waviness created using steel rods to initiate the perturbations in the plies. Experimental, analytical and numerical approaches which are discussed in previous chapter are used to incorporate the notch and waviness size effects on composite compressive and tensile strength. The OHC material allowable presents a critical design value controlling the design of a large number of composite structures. The OHC specimen can be modified to include a waviness zone to capture the effects of manufacturing defects. Temporal evaluations of the load response, acoustic emissions and optical microscopy are used to understand the failure modes in the specimens considered and their relationship to the load drops observed during the test.

### 4.1 Experimental method

In this study, the Open Hole Compression (OHC) and Open Hole Tension (OHT) tests for evaluating the effects of out-of-plane fiber waviness in continuous fiber reinforced composites are investigated. The OHC and OHT specimens are fabricated containing intentional waviness in unidirectional and multidirectional continuous carbon fiber/epoxy laminates. The proposed specimen design incorporates the OHC and OHT specimens with controlled levels of fiber waviness created using steel rods to initiate the perturbations in the plies. In addition, the effects of the waviness-associated resin pockets on the mechanical response have been experimentally evaluated. Temporal evaluations of the load response and optical microscopy are used to understand the failure modes in the specimens considered and their relationship to the load drops observed during the test. The OHC and OHT specimens in this study were fabricated using carbon-fiber epoxy in prepreg form and the specimen geometry in ASTM D6484 [64]. The carbon fiber/epoxy prepreg (resin pre impregnated fibers) is used for the specimens to reduce the variability in the processing since they produce more controlled fiber volume fractions and ply thicknesses. The fiber and epoxy used were a Toray prepreg T700GC-12K-31E fiber with the #2510 epoxy system[133].

Basic mechanical properties of unidirectional tape prepreg system are tabulated in Table 4.1. Three modes of the fracture energies including opening, in-plane shearing and out of plane shearing modes must be defined in the numerical method. The value of Mode I interlaminar fracture toughness is verified by testing that is conducted according to ASTM D5528 – 01 [134] for the mode I interlaminar fracture toughness of unidirectional fiber-reinforced polymer matrix composites. The values of Mode II and mode III were assumed to be equal [135]

**Table 4.1** Mechanical properties of the carbon/epoxy T700GC-12K-31E/#2510 Prepreg

| $E_1$ GPa (Msi) | $E_2$ GPa (Msi) | $\nu_{12}$ | $G_{12}$ GPa (Msi) | $F_1^{tu}$ GPa (ksi) | $F_2^{tu}$ GPa (ksi) | $F_1^{cu}$ GPa (ksi) | $F_2^{cu}$ GPa (ksi) | $F_{12}^{su}$ GPa (ksi) |
|---|---|---|---|---|---|---|---|---|
| 125 (18.1) | 8.40 (1.23) | 0.309 | 4.22 (0.613) | 2.16 (314.4) | 0.049 (7.09) | 1.45 (209.1) | 0.20 (28.8) | 0.15 (22.4) |

Interlaminar fracture toughness

| $G_{Ic}$ $Jm^{-2}$ (lb/in) | $G_{IIc}, G_{IIIc}$ $Jm^{-2}$ (lb/in) | $T_n, T_t, T_s$ GPa (ksi) |
|---|---|---|
| 217 (1.26) | 586 (3.35) | 0.049 (7.09) |

For the OHT and OHC group of specimens fabricated, prepreg plies are tailored and stacked up in unidirectional and multidirectional sequences (Table 4.2). The laminates were cured using a 'press-claving' approach where uniform heat and pressure are applied per the recommended 121 degrees Celsius (250 degrees Fahrenheit) cure cycle. Each ply has a nominal design thickness of approximately 0.15 mm (0.0059 in) in numerical modeling. The waviness is built at the center of the laminate going through the hole. The out-of-plane waviness geometry for the morphology can be characterized by means of a Gaussian function to capture the bell-curve response of the wavy plies. The Gaussian function can also be used to characterize the behavior from certain morphologies of given defects [12]. Several methods have been reported in the literature for creating fiber waviness profiles.

**Table 4.2** Waviness profiles investigated for open-hole

| **Waviness Height, $A_w$ mm (in)** | **Gaussian Function Parameter,$c^2$** |
|---|---|
| OHT coupons | |
| 1.54 (0.0606)<br>0.88 (0.0350) | 0.003<br>0.001 |
| OHC coupons | |
| 0.83 (0.032)<br>0.62 (0.0244)<br>0.5 (0.0196) | 9.0e-4<br>7.0e-4<br>5.0e-4 |

Some of these profiles have been successfully replicated in a study on fabrication methods by using ply drop offs or transverse strips of composite material to trigger the waviness profile [136]. Bonding specifically fabricated prepreg layers can produce high precision replication of graded waviness in carbon fiber composites. One study has shown how waviness can be made with oversized plies made to conform to a given geometry [137]. Potentially any method can be used to induce the waviness to more closely resemble the as built composite structure.

The waviness in the specimens was introduced in the composite by displacing the plies with a close-tolerance steel rod separated from the composite using a Teflon sheet. The diameters for the rods used correspond to the waviness result desired (from 0.5 to 1.54 mm). The bar was then easily removed from the composite specimen after the curing process was completed. The specimens were trimmed from 304 × 304 mm (l2 ×12 in) panels cured using the process described. The width of the specimen is 38.1 mm (1.50 in) and the length is 304.8 mm (12.0 in).

A notch is created in the specimen by having a centrally located hole with a diameter of either 6.35 mm (0.25 in) or 9.525 mm (0.375 in) centered by length and width. The hole was drilled in the specimen using a solid carbide drill bit with a rotation speed around 3000 rpm. A backing plate made from polymer composite material was used during the drilling process to minimize any damage during the notching process.

The resin pocket is not provided in coupons to exclude other influences in waviness examination. In manufacturing environments, the resin itself may pool into the recess created by the rod; thus the epoxy resin was added to the cavity left by the rod in the previous step. In the further steps, the specimens are examined on the side with the resin pocket and the back-surface where such a resin pocket does not exist. Cross-sectional views after polishing the side of the specimens are shown in Figure 4.1.

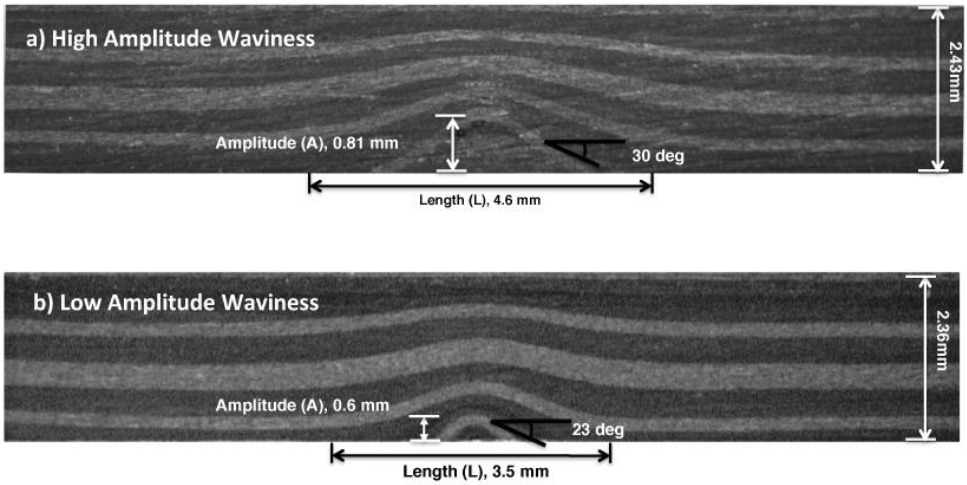


**Figure 4.1** Cross-sectional views of the defects in the test specimens

The length and depth of the out-of-plane waviness is typically used to characterize composite materials

**Table 4.3** Unidirectional and multidirectional layups investigated for out-of-plane fiber waviness in OHT and OHC tests

| **Layup** | **Number of Plys** | **Stacking Sequence** | **Nominal Laminate Thickness mm (in)** |
|---|---|---|---|
| OHT samples | | | |
| Multidirectional | 16 | $[0/45/90/-45/0/45/-45/0]_s$ | 2.44 (0.096) |
| OHC samples | | | |
| Unidirectional | 16 | 0 | 2.44 (0.096) |
| Multidirectional | 16 | $[0/45/90/-45/0/45/-45/0]_s$ | 2.44 (0.096) |

Three specimens were tested for each variable using an electromechanical test machine (314R: Test Resources, Shakopee,MN, USA) with a 100 kN loading capacity and tested under quasi-static compression and tension loadings. In the OHC test, a notched specimen is face supported using a multi-piece bolted support fixture (Figure 4.2). It is designed by Boeing and it took part of the ASTM D6484 standard. This test method has proven its ability to capture the effects of notches under compression loads [64]. In this procedure, a support fixture is used to support the faces during the compression test. The fixture consists of support plates and grip assemblies to support the specimen during the loading process and to maintain a 0 to 0.12 mm tolerance between the support plates and the long grips to minimize grip failures and friction effects (Figure 4.2). The specimen is gripped in place by using bolts to the support fixture. This lateral pressure was adjusted according to the recommend torque.

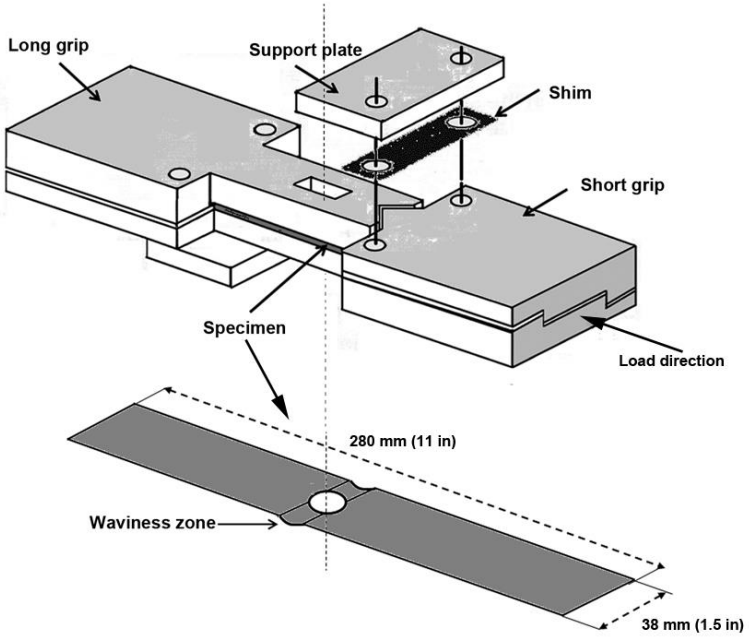


**Figure 4.2** Schematic of the open-hole compression specimen and test fixture[138]

When compression load is applied on the fixture, the sample supported by fixture in the lateral direction to restricting overall buckling and the specimens is loaded through shear in the grips. The test fixture is placed between flat platens and loaded in compression at each end. The experiments were performed in a displacement control mode at a rate of 0.1 in/min (2.54 mm/min). The loading rate was selected so that the failure would occur between approximately 2 minutes during the test. During the tests, the cross-head displacement and load were simultaneously recorded. The AE method was used to monitor the acoustic emissions in the specimens during loading since several damage events in the OHC specimen are not always visible in the load-deformation record.

Acoustic Emission (AE) measurements were recorded during the compression testing. A MISTRAS 2001 (Physical Acoustics Corporation, New Jersey-USA) was used to record the AE data in real time. An HD50 sensor with a medium resonant frequency and high sensitivity AE response has been selected since there is limited space for sensor mounting using the OHC fixture. The sensor has an operating frequency of 350-880 kHz with a resonance frequency of 500 KHz and peak sensitivity occurring at -70 V/mbar. For improving the quality of the captured signals; a pre-amplifier coupled with a band pass filter adjusted to pass frequencies in the range of 10-1200 kHz was used. The number of counts, amplitude, absolute energy, duration, signal strength and rise time were recorded during the test. The failure near the waviness zone was also captured using an optical microscope that was synchronized with the loading regime. During the measurements, the load, displacement, time and acoustic emissions were simultaneously measured.

The OHT specimens were tested in tension according to the ASTM D5766 standard for the open-hole tension strength of polymer composites with the exceptions of the deviations noted with layups and the proposed inclusion of the fiber waviness zone. The experiments were performed in

a displacement control mode. The load was applied using an electromechanical test system with a 200 kN (22 kips) capacity. The maximum error of the recorded load was within ±0.02 kN (5.0 lb). The shear response features need to be determined to use in analytical modeling. Figure 4.3 shows a representative shear stress-strain curve and the fitting parameters used in the analytical failure model [133]. This curve will be used to extract the shear stress and the shear strain parameters in the closed form solution.

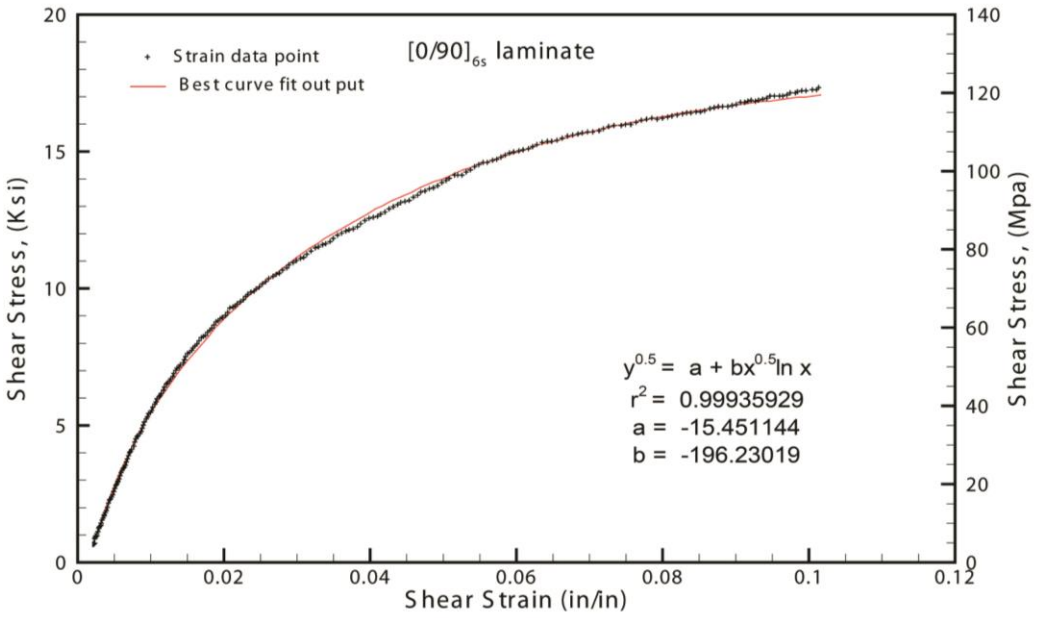


**Figure 4.3** The shear stress versus strain behavior for the T700/#2510 composite

The presented curve fitting equation can be used directly in the closed form equations however still there is a need to determine the yield point by making some restrictions to the “a” and “b” constants. To avoid engaging the closed form solutions with these complications, the yield strength of composites requires careful definition. For polymers, the yield point is identified as the stress at which the gradient of the stress-strain graph is zero. When such a local maximum is not present,

then it is defined as the stress at which the stress-strain curve becomes markedly non-linear: typically, a strain of 1%. The yield strength of a composite is best defined by a set deviation from linear-elastic behavior of 0.5% which is taken in the presented closed form formulation.

The variables investigated in the manufactured specimens are i) layup (unidirectional and multidirectional) ii) specimens with and without resin pockets, and iii) notch diameter and waviness levels. The characterization parameter of the fiber waviness is necessary for relating level of waviness to the OHC measured properties as shown in Equation 2.11.

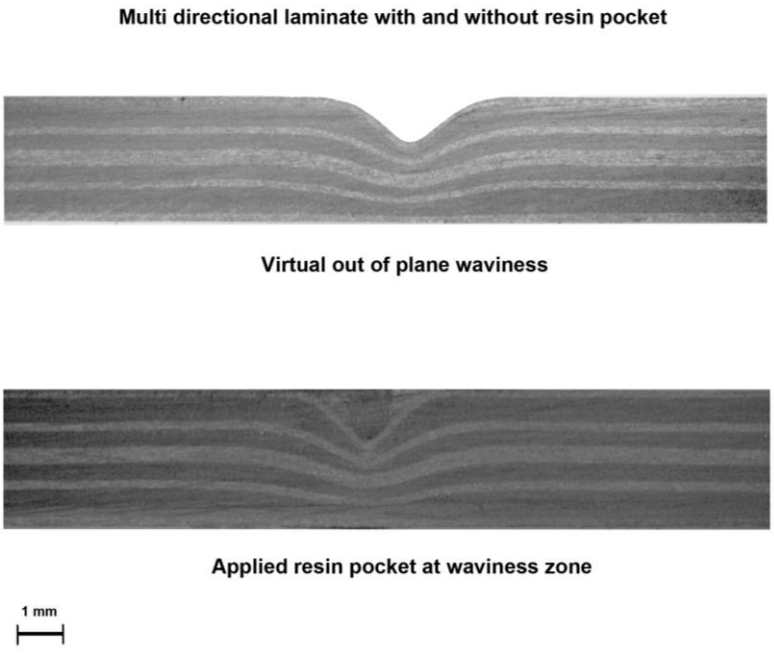


**Figure 4.4** Micrographs of waviness profile with and without resin pockets

Using a metric with the length can be problematic since of the length of the waviness is subject to the interpretation of the individual characterizing the waviness morphology. In this study we use the maximum amplitude of the fiber waviness and the angle. Figure 4.4 shows a cross view of specimens without resin pocket and with resin pocket. In Figure 4.5, different levels of

waviness are characterized with Gaussian function parameters.

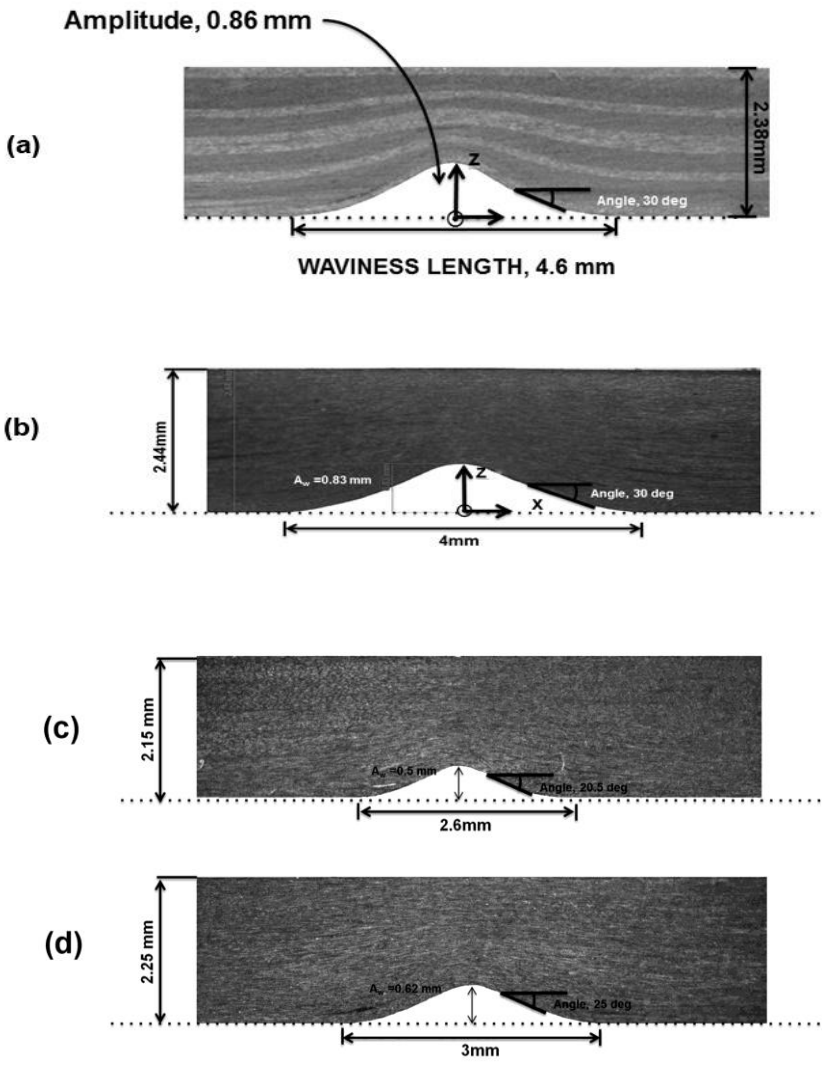


**Figure 4.5** Characterization of waviness profiles in a) multidirectional laminate using 0.032 in (0.81 mm) rod and unidirectional laminate with b) 0.032 in (0.81 mm), c) 0.024 in (0.6 mm) and d) 0.019 in (0.48 mm)[138]

Three specimens were tested for each variable using an electromechanical test machine with a 100 kN loading capacity and tested under quasi-static compression loadings. A total of 36

specimens were manufactured and tested as part of this effort.

An ultrasonic investigation using an immersion scanner (UT-3D 3-Axis; TecScan Systems, Quebec, Canada) performed in thru-transmission mode using a pair of 5Mhz transducers to investigate the free-edge delamination caused by drilling. The effect of the hole drilling on the laminate maybe made worse by the presence of the waviness. The results show some attenuation a few millimeters away from the TTU edge affected zone (Fig. 4.6).

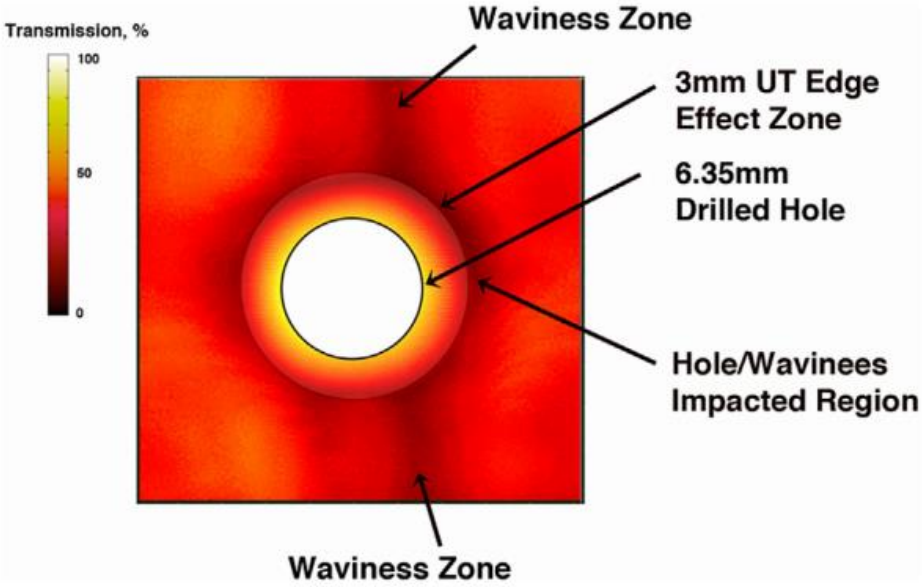


**Figure 4.6** Through-transmission ultrasonic c-scan near open hole[138]

## 4.2 Damage evolution in compression tests

The suitability and failure mechanics of the un-notched and OHC specimens with defects are investigated by the experimental observations of damage progression and the ultimate loads are compared with closed form solution obtained in Chapter 3. A finite element model is provided based on continuum damage mechanics explained in chapter 3 and results are evaluated with experiments for a representative waviness and a hole size. The failure mechanism in the OHC test is primarily a local fiber microbuckling failure based on the loss of stability of the fibers in the matrix phase. The fiber waviness is shown to affect the stress field to an extent by initiating the fiber microbuckling kinking failure. The study of the optical micrographs is used to study the origin of the failure initiation and the microbuckling of fibers. The kinking band inclination is caused by the need to balance compressive and shear deformations [139]. Subsequently, the final failure happens as a result of interlaminar delamination, the kink band broadening and fiber fracture. The average characteristic distance used in the calculations was computed by using the experimentally obtained strength of the notched and un-notched specimens without waviness (Equation 3.3). The stresses at failure of the notched coupons are calculated using the mechanical properties (Table 4.4) and the average gross cross-sectional area of the specimens since Equation 3.3 is based on the far field compressive stress.

In this table, the notched laminate strength (without waviness) is tabulated. The results for the 0.25 in (6.35 mm) hole size without waviness defects are used in Equations 2.4 to 2.7 to find the characteristic distance. It is shown that the notch can reduce the ultimate stress capacity of the structure more than 50 percent.

**Table 4.4** Mechanical properties obtained by the point stress criterion for unidirectional and multidirectional laminates

| 16 ply laminate | $E_{xx}$ GPa (Msi) | $E_{yy}$ GPa (Msi) | $G_{xy}$ GPa (Msi) | $v_{xy}$ | $K_T^{\infty}$ | Experiment $X_N^{\infty}/X_{Un}$ |
|---|---|---|---|---|---|---|
| Unidirectional | 124.1<br>18.0 | 8.4<br>1.23 | 4.32<br>0.627 | 0.309 | 6.55 | R1:0.45<br>R2:0.41 |
| Multidirectional | 60.3<br>8.75 | 34.3<br>4.984 | 18.2<br>2.644 | 0.431 | 3.1 | R1:0.4<br>R2:0.45 |

Characteristic distance $d_0$=0.027

R1=6.35 mm(0.25 in), $\frac{K_T}{K_T^{\infty}} = 1.03$

R2=9.52 mm (0.375 in ), $\frac{K_T}{K_T^{\infty}} = 1.08$

In the finite element simulation, once failure occurs, the index of failure meets one as defined through Equations 3.18 to 3.21. Figure 4.7 shows an overview of mesh containing notch and waviness and detail view of the waviness zone. The transverse shear stiffness for this element is taken into account using a constant correction factor through each layer. This feature provides a basis for estimating interlaminar shear stresses in a composite section. This model is used to study the notch and waviness size effects on notched composite compressive and tensile strength.

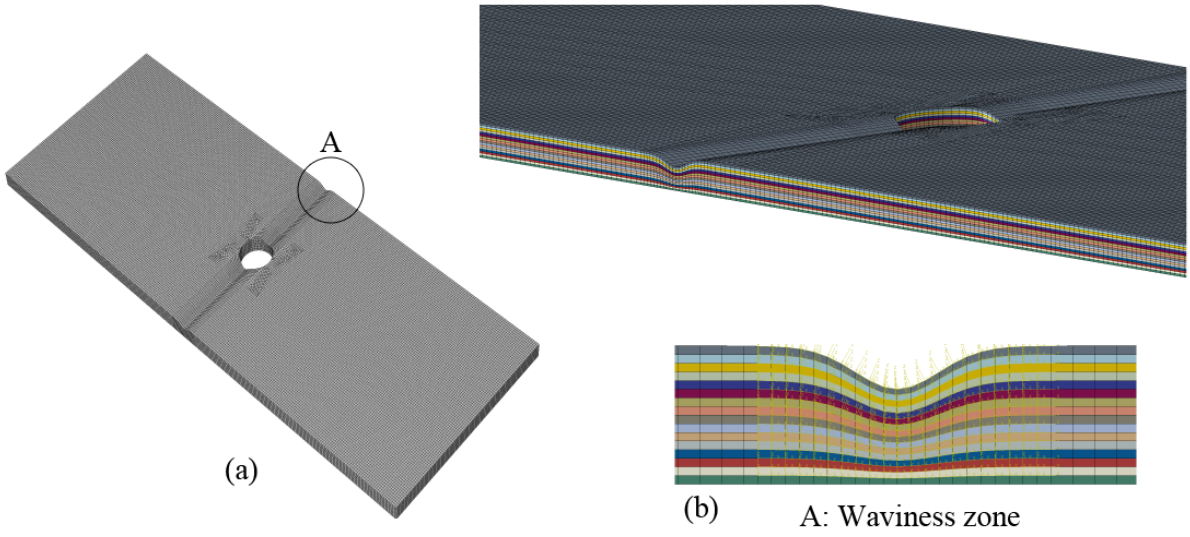


**Figure 4.7** FE Model of the composite laminate a) overview of mesh containing cut out and waviness and b) close up showing detailed mesh[140]

In the first case study, the failure model includes 2D-Hashin model where the interlaminar failure originated in the out of plane stresses is not taken into account. The modeling technique is brought using a layered description, each separate layer of the laminate is explicitly represented with its own DOF. Since this description introduces a number of DOF that depends on the number of layers constituting the laminate, this approach can rapidly become very expensive. This approach is obligated to use as a matter of changing material orthotropic definition along waviness zones. To reduce the processing time, a sub-laminate approach is used, in which plies are grouped together to form a composite section. The FEM modeling of uses a 3D shell quadrilateral elements, which are stacked on each other so to form the whole laminate.

In the second approach, the model has the advantage of the first approach in possessing layer-wise laminate description besides a bottom-up CAD modeling technique to provide separated

nodes for each layers. This approach is capable to be featured by surfaces assigning cohesive properties. The approach permits additionally to stack continuum-based solid elements in order to capture the detailed 3D stress tensor especially in out of plane directions.

The final configuration of both technique is going to be the same as shown in Figure 4.7 but the described features are built in the finite element details. The failure criteria of this approach as the 3D solid brick elements allows, has been taken as 3D Hashin/Puck model for the bulk composite materials. This criteria has been implemented as a user subroutine, VUMAT as mathematized in Chapter 3. The cohesive interlaminar zones has been also defined between layers in the current model. The model can be titled as a continuum damage with progressive interlamnar model. The results of both approaches have been collected in the results of the analysis. The results will disclose how the interlaminar stresses play an important role in describing the failure behaviors and establish a conservative results.

### 4.2.1 Damage evolution in unidirectional OHC specimens

The failure mechanisms for the OHC unidirectional specimens (without waviness) are in the form of longitudinal fiber splitting. This is due to high strains which introduce local damage near the hole edge in the form of axial splitting and transverse matrix cracking resulting in stress redistribution and a reduction of the stress concentration factor [141]. The matrix shear failure mechanism originating from Poisson's effects can be significant in unidirectional composites where the transverse strength is low [142]. The results of the OHC tests are used to compare with the experiments of OHC specimens containing defects to understand the contributions of the notches and waviness on the compressive strength reduction separately.

Figure 4.8 shows the progression of the failure in a unidirectional laminate for the laminate without a resin pocket (Figure 4.8-a) and with resin pocket (Figure 4.8-b) before and after the kinking band formation. The microscopic observations show the kink band dominates laminate failure leading to major matrix cracking, interlaminar failure and fiber breakage. The OHC specimens with waviness show a localized failure at the fiber waviness location and a larger likelihood of a kinking type failure compared to the un-notched specimens. For the high amplitude waviness, the compression load induces shear and transverse stresses which dominate the behavior of the specimen. The built in clearance in the OHC fixture has an effective role in the kinking band formation for both multi and unidirectional laminates. Appropriate clearance which is maintained by using shims in unsupported zone allows the laminate to be susceptible to microbuckling.

Fiber kinking has been observed for both specimens with and without the resin pocket, however the fiber kinking is postponed in laminates with the resin pocket. The onset of the kinking occurs at the vertex of the waviness to the straight face. The optical microscope view on the side of the unidirectional specimen shows a comparison between a representative specimen (with the waviness of 0.032 in) containing the resin pocket and one without.

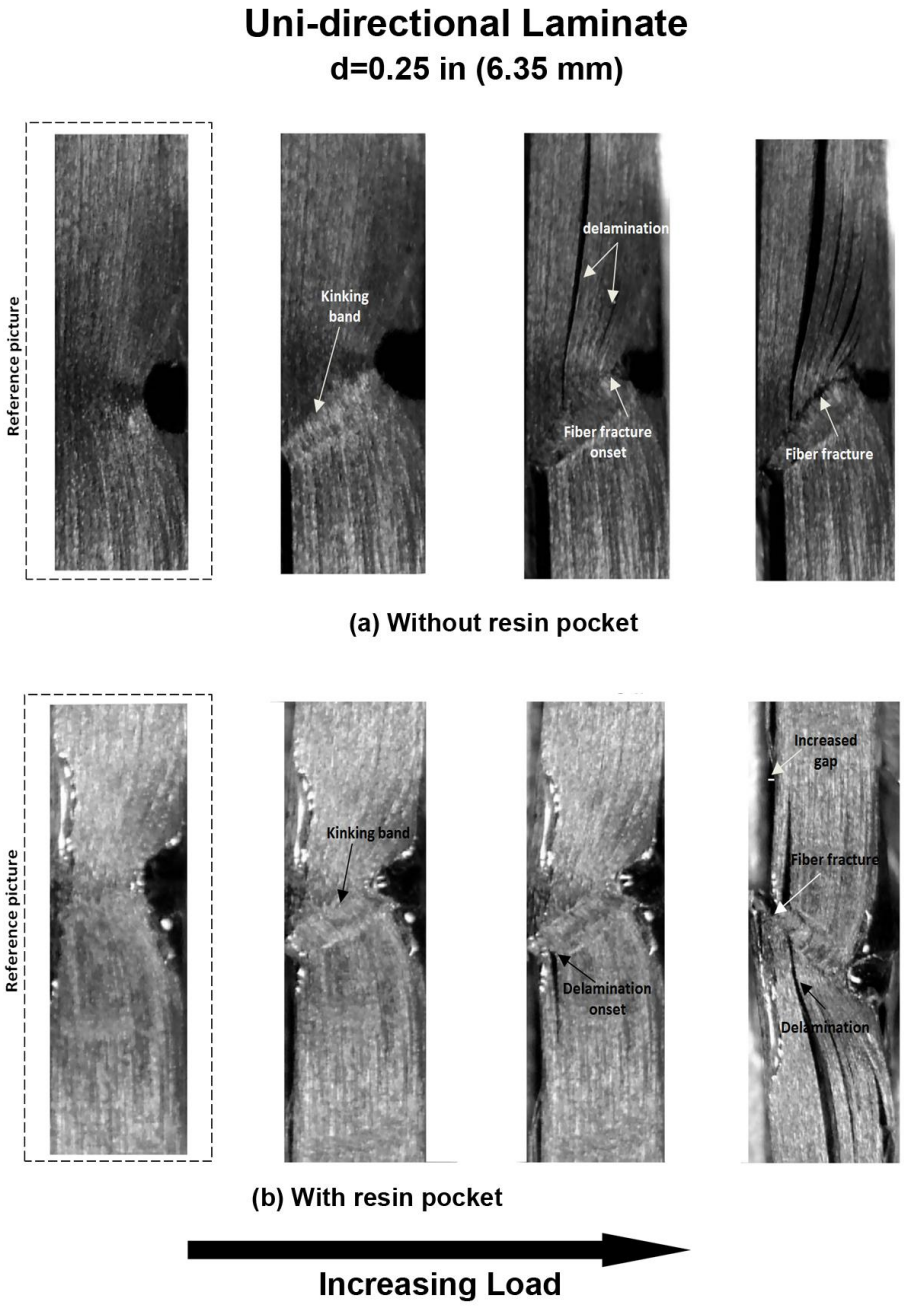


**Figure 4.8** Optical micrographs showing damage initiation and evolution in a unidirectional OHC specimen containing fiber waviness (a) with and (b) without the resin pocket[138]

Optical microscopy shows how the onset of kinking is followed by the crack onset modulated by the stress transferring mechanisms and fiber failure. Microscopic evaluation and the associated AE measurements show the location of the damage initiation occurring at the hole edge. The successive failure events are not always easy to capture due to the dynamic nature of composite material failures. Therefore for the subcritical failures not visible using the optical microscope, the AE technique is more powerful to indicate failure modes. For example, delamination in AE shows as low acoustic energy/long duration compared to the high-energy/short duration AE events associated with fiber failures. There is a high stress concentration at the notch hole boundary initiating a local crack primarily at the resin pocket. Figures 4.9 and 4.10 show the load-displacement plot associated with the cumulative energy and number of counts extracted from the AE sensor.

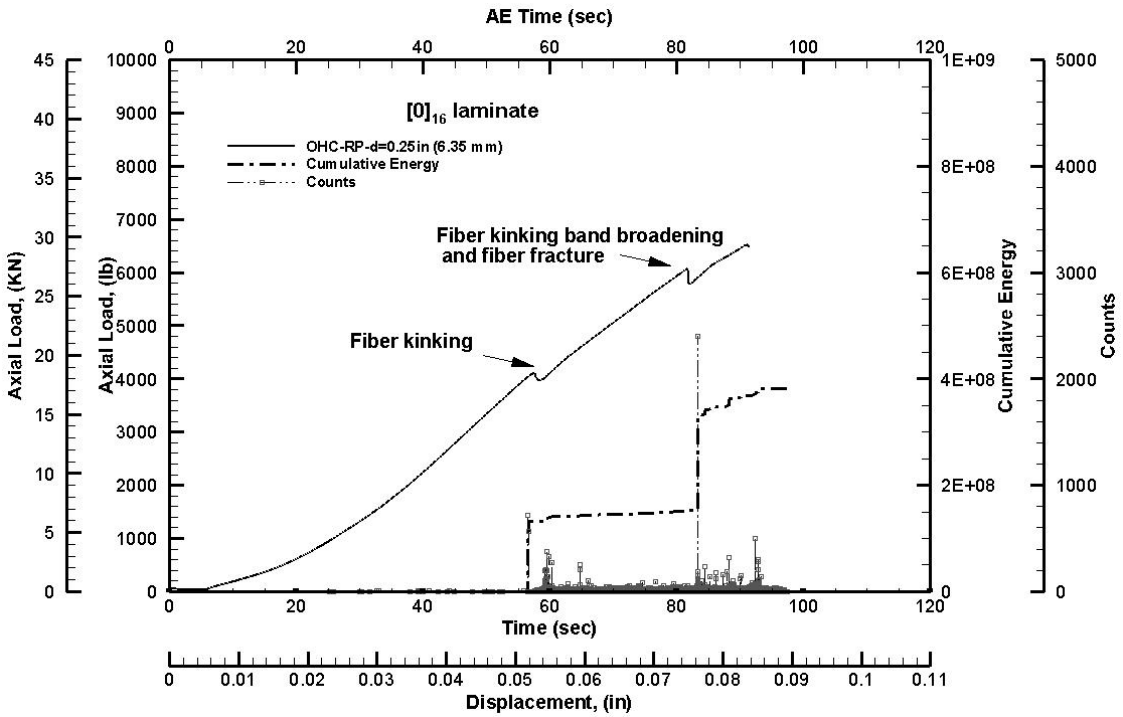


**Figure 4.9** Temporal Load and AE for a representative OHC unidirectional specimen with 30° misalignment angle containing the resin pocket and the hole size d= 0.25 in (6.35 mm)[138]

Figure 4.9 illustrates two main load drops in the load versus deformation response. The first load drop is related to the fiber kinking and the second load drop is due to the fiber kinking band broadening and fiber fracture caused by the sliding stress at the line of the inclination angle.

Microscopic images show the fiber kinking starting with the fibers with the higher amplitude waviness. The location of the fiber kinking onset is at the point where the waviness was characterized by the misalignment angles. The maximum fiber misalignment angle is used in the analytical approach for the specimens without the resin pocket. The analytical approach was not applied to the waviness stabilized by the resin pocket due to the additional support provided. The analytical approach thus represents a conservative condition when the resin pocket stabilizes the waviness zone.

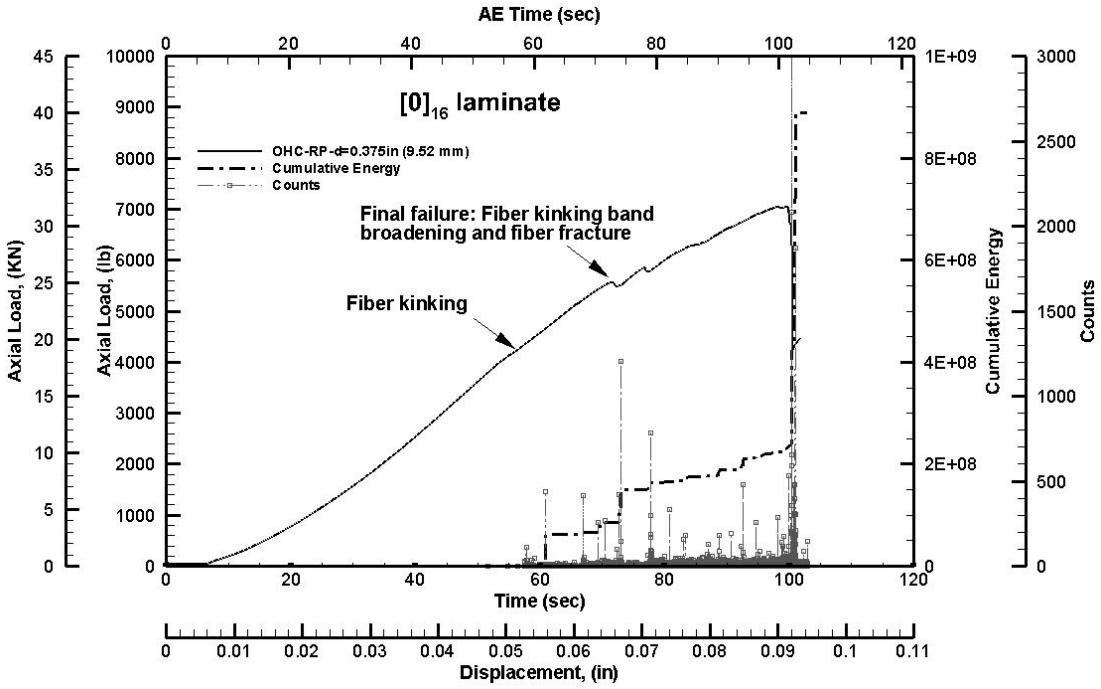


**Figure 4.10** Temporal Load and AE for a representative unidirectional specimen with 30° misalignment angle containing the resin pocket and the hole size d= 0.375 in (9.52 mm)[138]

The amplitude of energy and counts for the load lower than 3860 lb (17.2 KN) are (less than 25 counts) suspected to be due to matrix cracking. The AE results show a very low AE energy associated with these cracks which don't affect the load curve as a load drop. From the synchronized microscopic observation with load displacement curve, the location of the kinking zone on the loading curve can be identified and synchronized with AE measurements. Figure 4.10 shows a similar behavior around the time where the fiber kinking appeared. A slight change in the load-displacement curve around the fiber kinking band can be caused by the fixture built in clearances and is not always visible.

Excessive torque applied on the fixture or not enough shim thickness can reduce the gap between the specimens and the grip plates leading to restriction of the kink band formation. This discrepancy does not affect the results as long as the clearance is in between 0 to 0.005 in (0.127 mm) as provided by ASTM D6484. As a result of interactions between the hole and the waviness, the open hole affects the fiber kinking strength and mutually the waviness stress field is seen to redistribute the stresses around the open hole. The extension of the load capacity after the second drop can be caused by engaging fractured fibers and is not considered in this study.

Figure 4.11 shows the fiber fracture inclination line for various waviness amplitudes before final fracture. The authors suggest measuring the inclination angle during the tests by microscopic apparatus since after finishing the test, the excessive deformations and fiber breakage make the measurements unreliable.

The inclination angles are measured about 30° for all various waviness. The microscopic investigations show the progressive crack propagates along the inclination line from the fibers with the higher waviness angles towards the back surface of the specimen.

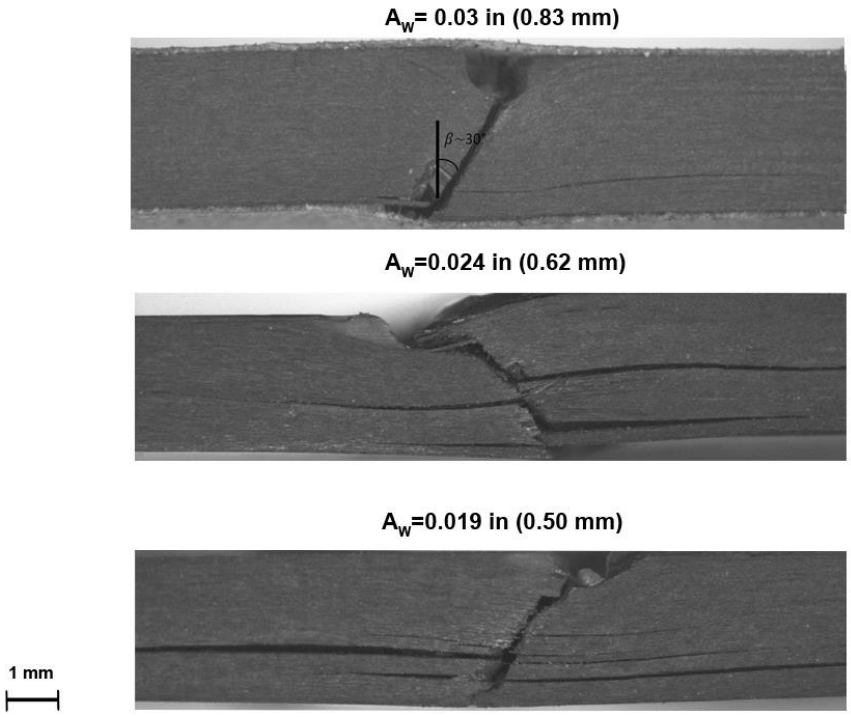


**Figure 4.11** Failure inclination angle for the various waviness amplitudes[138]

Waviness induces a larger displacement for the wavy fibers compared to the straight fibers leading to a local bending moment and out of plane stresses driving mixed mode delaminations. This bending moment does not create significant delamination in the high amplitude waviness area as it is essentially compressive but is more severe at the farthest fibers. The minor delaminations occur due to matrix cracking in the high amplitude zone.

On the other hand, the kink zone is developed through the thickness derived by the built in fixture clearance and transfer of shear stress. The number of AE counts have jumped twice from 3 to 716 at about 60sec indicating the first kink zone. Final failure occurs at 73sec by sliding fractured fibers over an inclination line where the oblique fracture can be seen in microscopic images. Figure 4.12 also shows how the resin pocket postpones the kink band formation and

increases the load bearing capacity. As a result of the comparison in Figures 4.12, the time between the first and second load drop is doubled in specimens with the resin pocket.

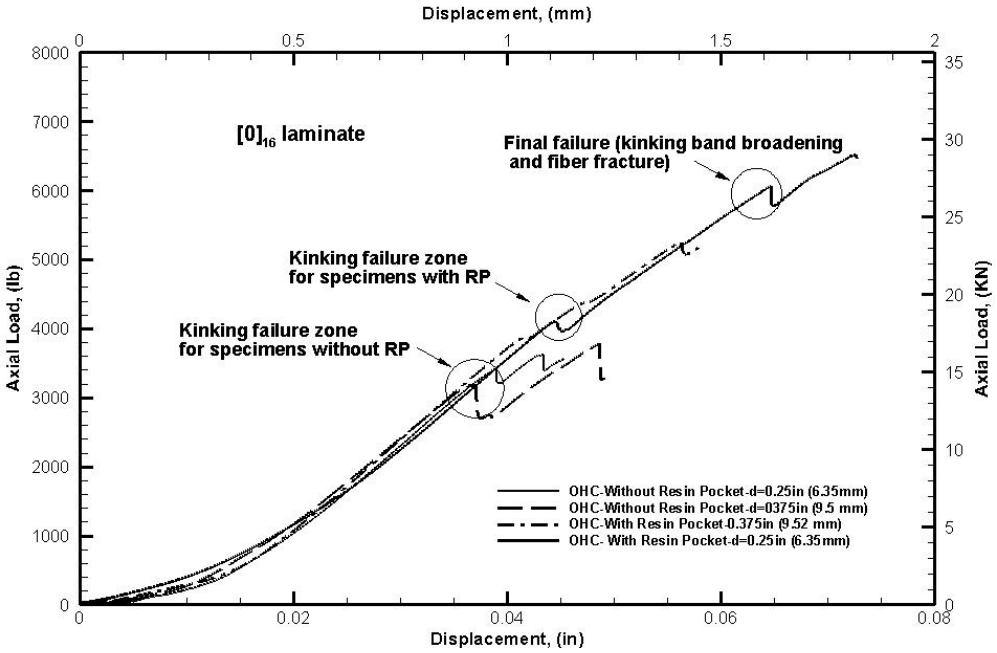


**Figure 4.12** Temporal Load and displacement in unidirectional specimens[143]

Results for the analytical approach predictions of failure loads of unidirectional waviness specimens are summarized in Table 4.5.

**Table 4.5** Analytical predictions of compressive strength for the unidirectional laminate with different waviness amplitude without hole

| $A_w$ mm (in) | $X_C$ Experiments (without hole) Mpa (Ksi) | $X_C$ Analytical (Equation 3.3) Mpa (Ksi) | Error% |
|---|---|---|---|
| 0.5 (0.0196) | 442.9 (64.25) | 465.9 (67.58) | 3.4 |
| 0.62 (0.0244) | 357.1 (51.8) | 374.8 (54.37) | 4.5 |
| 0.83 (0.032) | 296.9 (43.07) | 313.5 (45.47) | 5.2 |

It should be noted that the experimental $X_C$ is normally calculated from the gross cross sectional area of the specimen to account for far field strength computation. The analytical approach used shows a reasonable correlation with the experimental measurements.

The influence of waviness for un-notched specimens is shown in Figure 4.13.

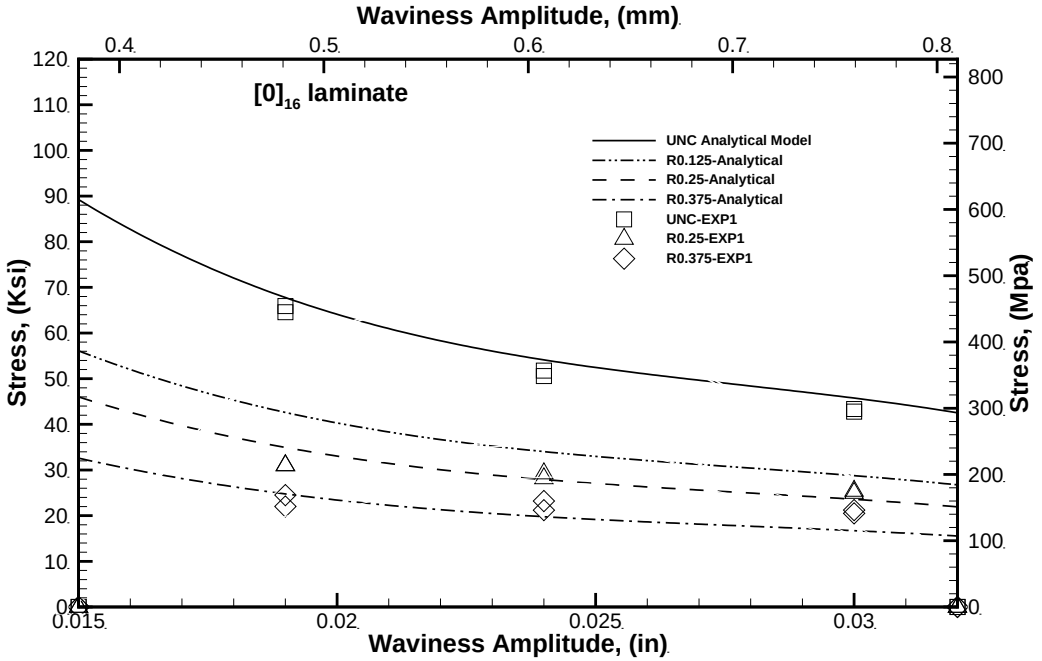


**Figure 4.13** Summary of OHC and UNC strength properties of laminates with different size of waviness

As the analytical model has been derived for kinking within a band of finite width and infinite extent for fibers with high amplitude waviness, the results should not be completely matched with specimens with applied resin pocket since resin pocket supports the fibers at that zone to take a higher stress. The fiber kinking is a matrix failure based and cannot be directly used to assess the additional stabilization provided by the resin pocket.

The detail quantity of the ultimate stresses influenced by combined notches and waviness summarized in Table 4.6 for unidirectional specimens.

**Table 4.6** Analytical predictions of compressive strength for the unidirectional laminate with different waviness amplitude and hole sizes

| $A_w$ mm (in) | $X_C$ experiment Mpa (Ksi) | $X_C$ Analytical (Equation 3.4) Mpa (Ksi) | Error % |
|---|---|---|---|
| 0.5 (0.0196) | R1: 213.7 (31)<br>R2: 168.9 (24.5) | R1:239.9 (34.8)<br>R2:170.3 (24.7) | -12.3<br>-0.78 |
| 0.62 (0.0244) | R1: 194.4 ( 28.2)<br>R2:153 ( 22.2) | R1:194.4 (28.2)<br>R2:136.9 (19.86) | 0.43<br>10.5 |
| 0.83 (0.032) | R1:169.6 (24.6)<br>R2:141.3 (20.5) | R1:161.6 (23.44)<br>R2:120 (17.4) | 4.5<br>15.4 |

Computations are based on n=3 in Ramberg-Osgood representation

Inspection of stresses for both types of specimens (notched samples without waviness and wavy samples without notches) can be used to infer that the effects of the notch and waviness

interactions. One of the main results of this study can be implied on the initiation and propagation of the damage in laminates with notches and waviness imperfections where the crack onset initiates from the notch and the waviness develops the failure by the premature fiber kinking and bending mechanisms. Figure 4.13 shows that the failure load capacity has not been aggressively influenced by different hole sizes.

Now the results of the finite element model will be scrutinized while looking at every failure mechanisms and location wise observations have not been feasible in experimental and analytical models. At the first glance, since the fibers have been impacted by waviness in degradation level toward the back of the laminate, the failure mechanisms are varied through thickness of the laminate. In the OHC simulation, the failure is initiated at point 1 in Figure 4.14 at fibers of the layers with higher waviness and matrix around the notch zone while the matrix on the back layers is not failed yet.

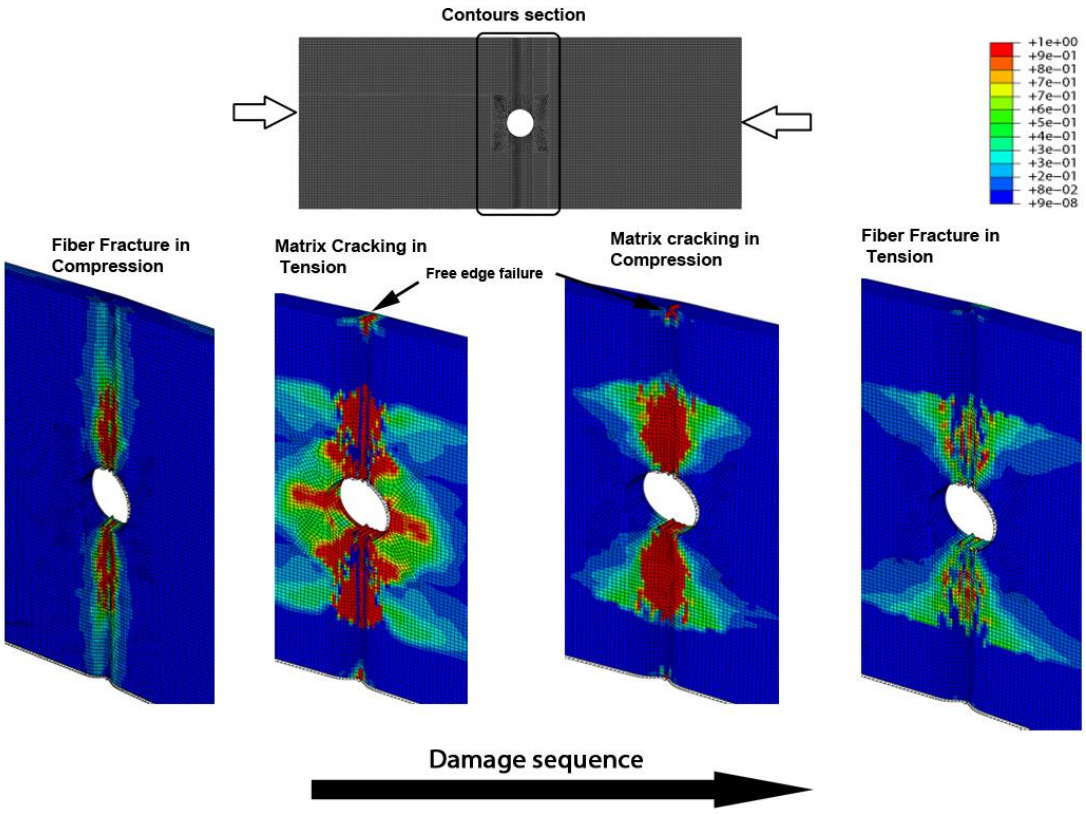


**Figure 4.14** FE simulation of failure associated with four modes of Hashin's criteria in the OHC unidirectional laminate[140]

Figure 4.14 also shows the evolution of the fiber splitting failure in the longitudinal direction (in matrix cracking failure mode in tension) for the OHC unidirectional specimen. The matrix failure in compression mode occurs at the waviness zone around the hole and free edges, The fiber failure under tension is not clearly distinguished when the waviness zone is crushed under previous activated failure modes. From the experimental observations, the free edge failure is activated before point 3 where the final fracture occurs (Figure 4.15).

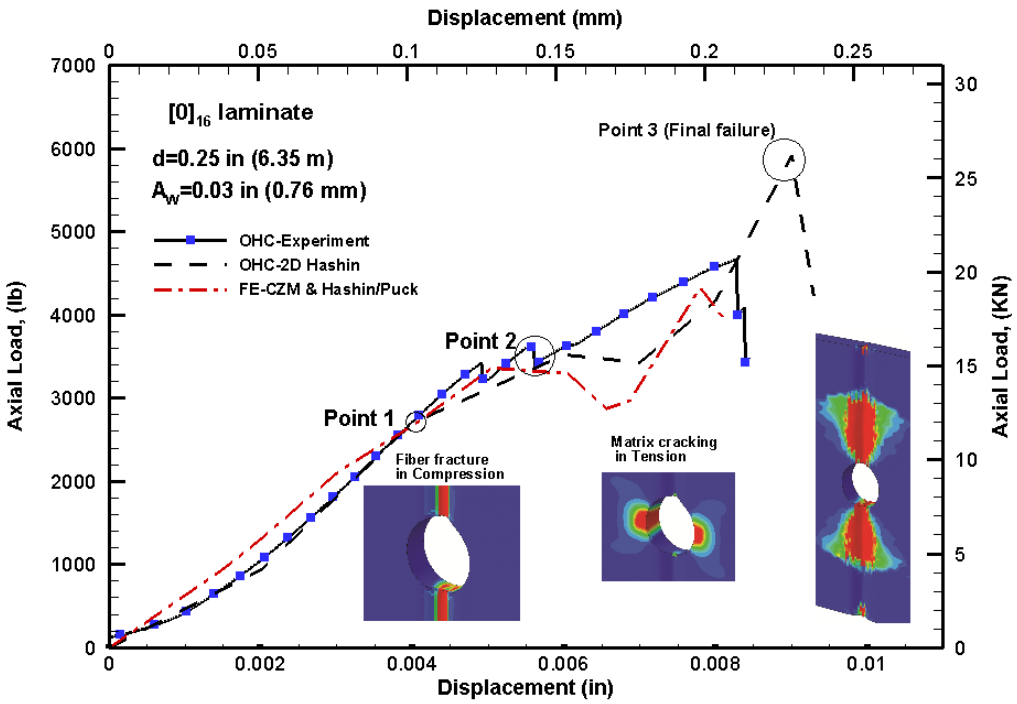


**Figure 4.15** Failure propagation of unidirectional OHC laminate, comparison of FE and Experiments[140]

In the OHC specimens, the stress is transmitted from the fiber to matrix successively (between point 1 and 2). At point 2 the failure is developed in the matrix along the longitudinal direction (along the applied load) to the lateral direction at the notch and then propagates to the laminate free edges. At this point the damage has not propagated for the plies with lower waviness.

The final failure occurs by increasing the displacement where the main portion of the OHC sample experiences failure in all four failure modes. From Figure 4.15, the FE model shows higher load capacity than the experiments. The Hashin's criterion provides better predictions for initiation rather than final failure. It is worth noting that the matrix and fiber failure in tension occur first at the plies with the lower waviness since those plies are in tension meanwhile high waviness plies are under a high rate of compression loading and some have already failed.

Through thickness FE observations shows the fiber failure in compression and matrix failure in tension for the elements shown in (Figure 4.16). In this Figure, the curves are provided as polynomial regressions between layers discontinuities.

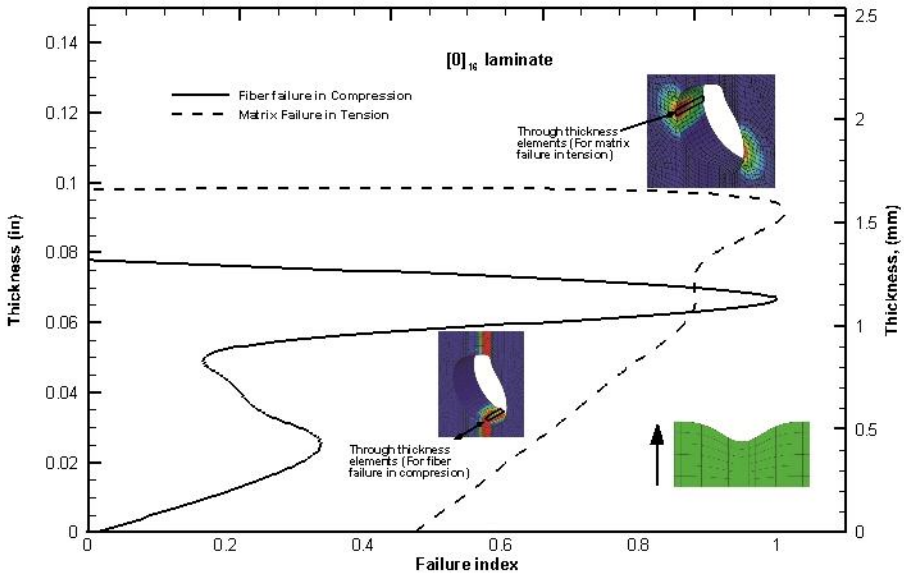


**Figure 4.16** The failure progression through the thickness in the unidirectional OHC specimen[140]

### 4.2.2 Damage evolution in multidirectional OHC specimens

The role of angle plies is highlighted whilst the interlaminar stress is involved. The interlaminar stress rises at free edges (the hole and specimen's sides) and can be reached to the interlaminar strength. As the kinking is a matrix derived failure phenomenon and the in-plane shear strength at plastic yielding point is close to interlaminar shear strength, the failure sequence between kinking and interlaminar failure cannot be easily distinguished. Note that the interlaminar

stress for carbon/fiber epoxy laminate is approximately linear before the softening process therefore the interlaminar strength can be considered as the yield shear strength. Berbinnau et al [144] verified that the influence of off-axis plies on the 0° fiber kinking is small. For un-notched specimens, Prabhakar and Waas [145] investigated the compressive strength of multidirectional laminates and effects of stacking on failure modes. They concluded that the cohesive interlaminar strength is an important factor in influencing the compressive strength. Berbinnau et al.[144] emphasized that the off-axis plies have little effect on the $0^o$ fiber kinking stress unless other defects at the $0/\theta$ interfaces degrades the laminate interlaminar stiffness resulting in delamination and premature microbuckling. Therefore in an identical condition of laminates with the waviness, the compressive failure of unidirectional and multidirectional laminates is controlled by the fiber kinking. A similar failure trajectory could be identified for the multidirectional laminate tests. The failure mechanisms in multidirectional composite laminate is observed to be a combination of kinking for the 0° fibers and subsequent delamination at interfaces with the angle plies. By decreasing the amplitude of waviness the contribution of kinking stress is reduced and the interlaminar stress at the free edge is increased. However the overall results of the kinking strength are not affected by the angle plies in multidirectional laminates.

The highest ply mismatch appears to favor the path of delaminations at -45°/90° and 0°/45° as it can be clear in Micrographs (Figure 4.17) show a close-up of the waviness zone in representative multidirectional specimens.

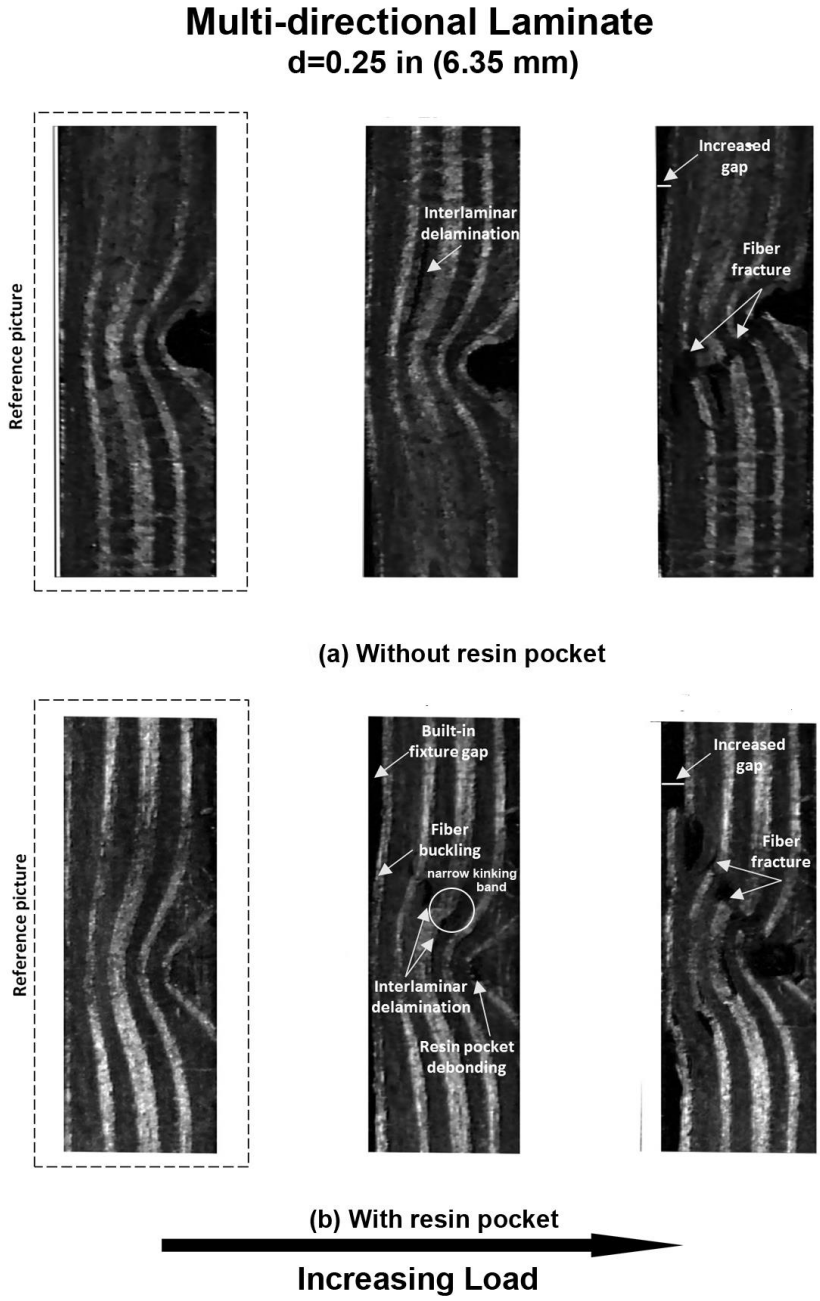


**Figure 4.17** Microscopic images of the damage initiation and evolution in multidirectional laminates a) with and b) without resin pocket[138]

The test starts after one minute from the beginning of the test. The photography shows how a narrow kinking band occurs in the 0° fibers which are especially notable for the 0°/0°

interfaces. Fiber fracture occurs successively since the delamination makes fibers unsupported and prone to fracture. The load-displacement curves exhibit a significant drop associated with the fiber fracture. Figure (4.17-a) shows the progression of failures of multidirectional samples without the resin pocket. Figure (4.17-a) barely shows a very narrow band of kinking in 0° fibers in the middle of the specimen besides significant delaminations in adjacent plies.

Damage progression of multidirectional laminates with the resin pocket (Figure 4.17-b) illustrates that after the delamination failure a wider band of fiber kinking is seen to occur. The kinking band is larger for the 0°/0° plies undertaking higher compressive stresses.

It also indicates that the delamination occurring at the $0^o/45^o$ interface at the bundle of un-wavy plies where the induced bending moment contributes to delamination and kinking.

The structural degradation induced by delamination impacts the bundle of wavy plies where subsequent sliding between the angle-plies results in drastic fiber breakage in this bundle. It has been observed that that the notch and high amplitude waviness (relative to low amplitude with large wave length) prevent the plies to experience considerable fiber kinking deformations before final fracture. First fiber fracture starts from the farthest 0° fibers to the waviness zone where the bending moment is maximized. The load-displacement curve does not show load drops indicating kink band formation. Figure 4.18 shows the kinking band in specimens without the resin pocket has been occurred adjacent to the final failure by tracking of the cumulative energy and response.

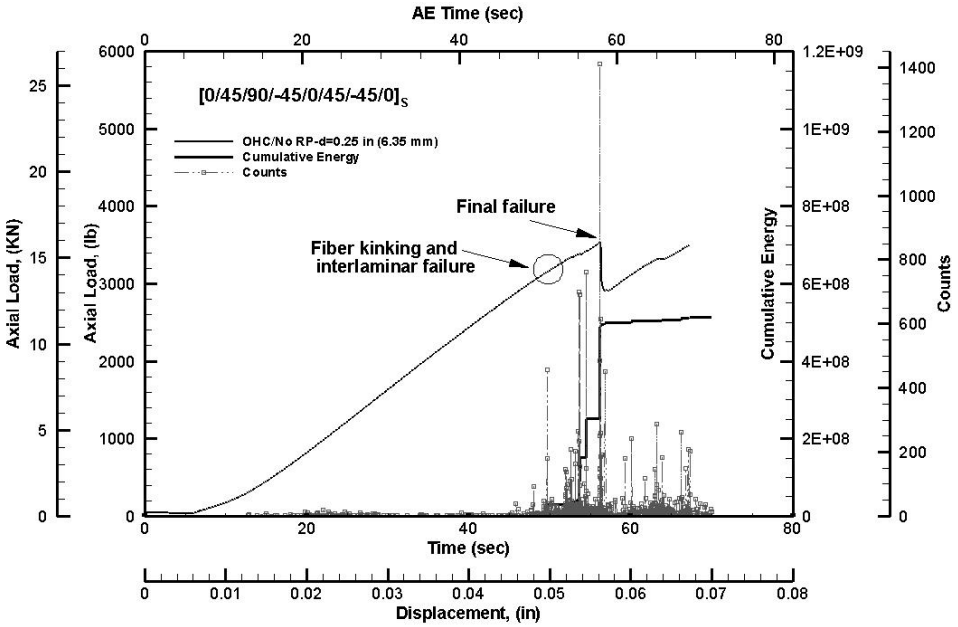


**Figure 4.18** Temporal Load and cumulative acoustic energy in multidirectional specimens without the resin pocket and with the hole size d=0.375 in (9.52mm)[143]

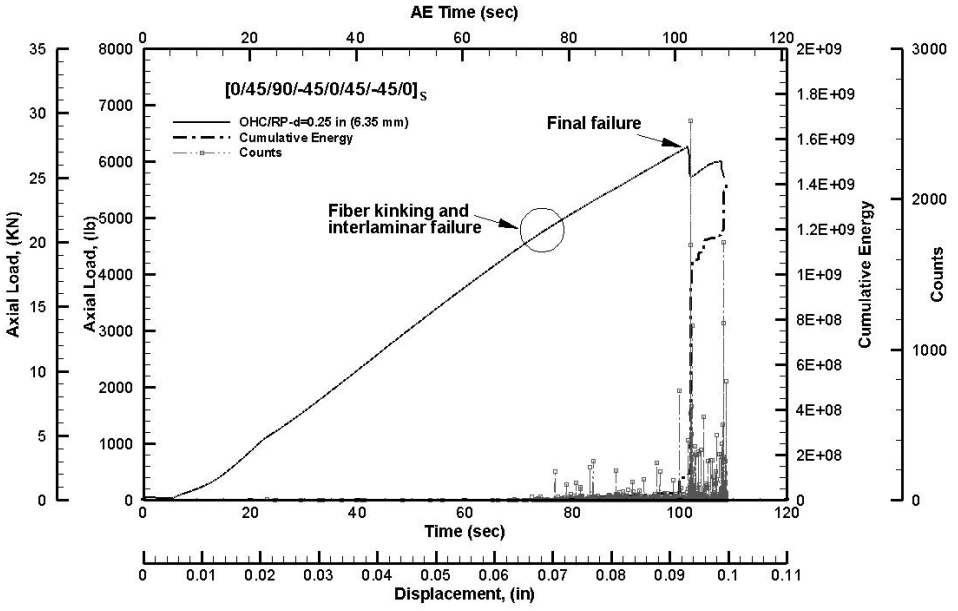


**Figure 4.19** Temporal Load and cumulative acoustic energy in multidirectional specimens with resin pocket and the hole size d=0.25 in (6.35mm)[138]

The kinking failure occurred at 53sec with about 760 counts. Figure 4.19 shows the results for the multidirectional laminates in the presence of the resin pocket. Figure 4.19 shows the matrix cracking starts from 60 seconds with the number of counts under 150. The fiber kinking and delamination onset appears from 78 seconds between the numbers of about 500 counts. However, Figure 4.19 also shows a change in the laminate stiffness after the kinking and delamination. The AE results show a relatively large energy jump ahead of the fiber fracture pertaining to kinking band broadening at 105sec. The AE signal associated with the kinking band broadening zone is increased to almost double the amount to 1000 counts at final failure. The energy burst in the kinking zone is contributed by matrix and fiber fracture. The fiber failures in the gage section create a large burst of emissions also showing an abrupt drop in the load-displacement plots by more than 1500 counts in the final failure.

Delaminations are seen between layers at the time of local buckling in advance of the fiber fracture. In comparison with unidirectional laminates, interlaminar delaminations (mostly appearing between 0 and cross-ply layers) are much more significant. Figure 4.20 shows the results for the larger hole sizes and illustrates a distinctive load drop associated with the developed fiber kinking through thickness. Figure 4.20 also shows the kinking, interlaminar delamination and kinking band broadening as the sequence for the failure mechanisms by considering AE counts and energy jump.

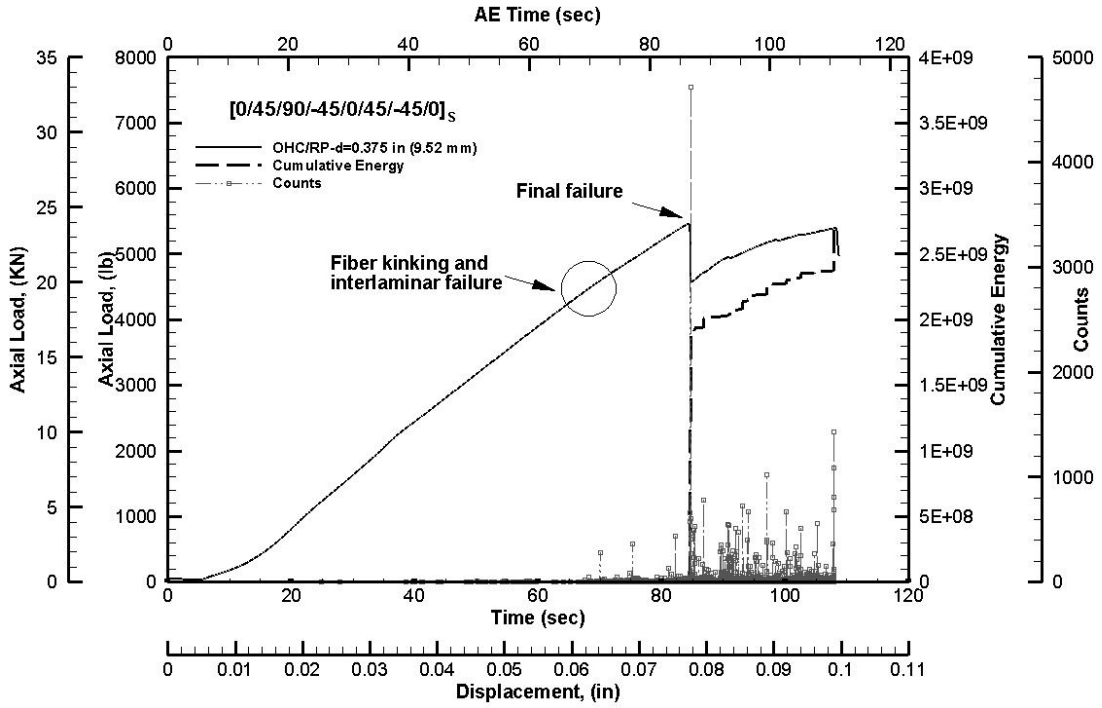


**Figure 4.20** Temporal Load and cumulative acoustic energy in multidirectional specimens with the resin pocket and the hole size d= 0.375 in (9.52 mm)[138]

Figure 4.21 shows how the specimens with resin pockets have a higher load capacity compared to the specimens with no resin pockets. Note that the final failure in specimens without the resin pocket are controlled by the fiber kinking while in specimens with the resin pocket, the final failure has been shown to be governed by the fiber kinking. In specimens with the resin pocket, the crack is initiated from the notch and moves toward the free edge through the resin pocket. The debonding failure has been seen to occur at the interface of the resin pocket with the $0^o$ ply. Since the resin pocket supports the wavy fibers against local buckling, it is obvious that the kinking strength can be increased. This is also the reason for under estimation of the kinking strength for specimens with the resin pocket by using the analytical model. After kinking formation in specimens with the resin pocket, fibers are still capable to carry the compressive load before

fracture while without resin pocket, the fiber fracture occur earlier after the kink formation. Figure 4.21 shows minor changes in average failure load for unidirectional and multidirectional laminates which is compatible with the results of Lee et al. [146] as the final failure is controlled by waviness and the notch size effect is not significantly affects the load bearing capacity. For the specimens without resin pocket, the kinking failure load is occurred adjacent to final failure. Final failures are found as the kinking band broadening across the width and through the thickness.

But in specimens with the resin pocket, the kinking band broadening is not coincident with the kinking failure. The laminate can bear more loads until final failure. Results in Figure 4.21 also show the notch size effect is influential on specimens with resin pocket however these specimens still possessing better performance than specimens without resin pocket.

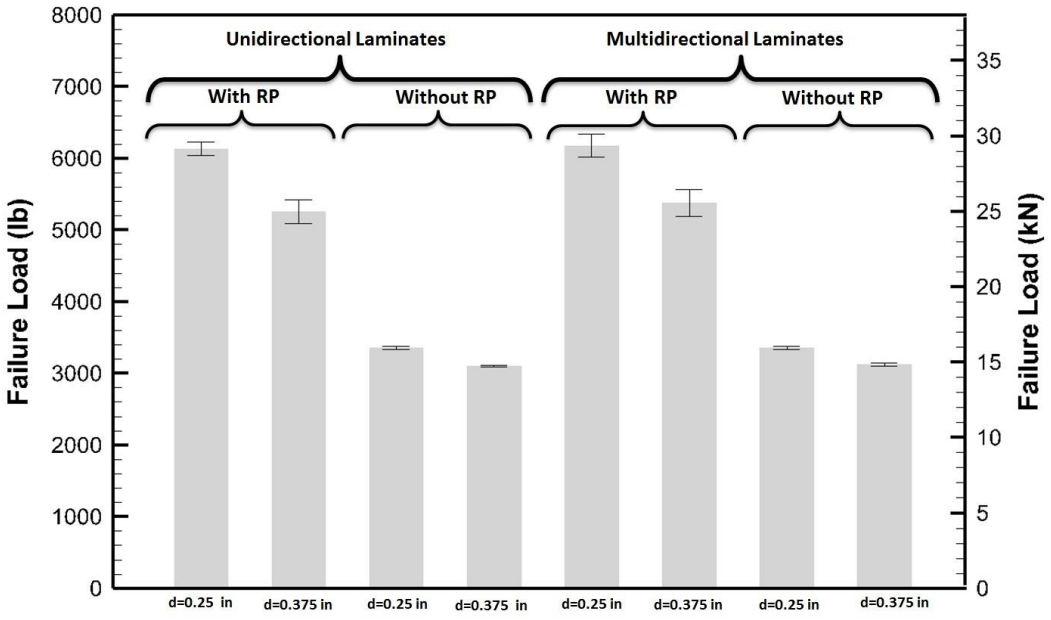


**Figure 4.21** Resin pocket effects on final failure of laminates with the fixed waviness size and various notch sizes

By using Equation 3.4, the ultimate stress of the Multidirectional laminate have been obtained and compared with experiments showing in Table 4.7. The interlaminar strength which is considered as an effective shear stress in multidirectional case has been replaced with in-plane shear plastic yield strength.

**Table 4.7** Analytical predictions of compressive strength for the unidirectional laminate with a waviness amplitude and hole sizes

| Amplitude 0.83mm (0.032in) | $X_C$ experiment Mpa (Ksi) | $X_C$ Analytical (Equation 3.4) Mpa (Ksi) | Error% |
|---|---|---|---|
| Multidirectional | R1:168.9 (24.5 )<br>R2:157.2 (22.8) | *R1:166.8 (24.2)<br>*R2:170.3 (24.7) | 1.5<br>-7.8 |

This is noteworthy that the notch size does not have a significant impact on the final failure load as we have seen in the unidirectional laminate for examined notch sizes. A comparison of Tables 4.6 and 4.7 reveals an important conclusion of examination of these two layup in possessing relatively similar values of failure strength. It can be interpreted that the examined multidirectional layup, in presence of waviness defects, demonstrate better performances in the compression test.

Before displaying the results of the finite element model a results are summarized as following statements:

- The failure mechanism in the OHC test is primarily a local fiber microbuckling failure based on the loss of stability of the fibers in the matrix phase.

- The kinking band inclination is caused by the need to balance compressive and shear deformations. Subsequently, the final failure happens as a result of interlaminar delamination, the kink band broadening and fiber fracture.

- The microscopic observations show the kink band dominates laminate failure leading to major matrix cracking, interlaminar failure and fiber breakage.

- The OHC specimens with waviness show a localized failure at the fiber waviness location and a larger likelihood of a kinking type failure compared to the un-notched specimens. For the high amplitude waviness, the compression load induces shear and transverse stresses. These local stresses dominate the behavior of the specimen.

- The back surface and through the thickness view of the fractured specimens illustrate the fiber splitting and shear failure mechanisms contributing to the final failure. It is worth noting that the failure on the front face is a neat fiber fracture along the waviness zone for both unidirectional and multidirectional specimens.

- Multidirectional laminates in open hole compression testing do not show the same pattern in damage progression. The role of angle plies is highlighted whilst the interlaminar stresses are significantly involved. The interlaminar stress rises at free edges of the hole and specimen's sides to reach to the interlaminar strength.

- As the kinking is a matrix driven failure phenomenon and the in-plane shear strength at plastic yielding point is close to interlaminar shear strength, the failure sequence between kinking and interlaminar failure cannot be easily distinguished.

The results of the finite element model displays a distinctive behavior which may less observed in experiments. The fiber splitting in multidirectional laminates has not been observed as a failure mechanism in experiments. The damage zone is less propagated through the laminate (Figure 4.22) where the damage is mainly limited to waviness zone. The hole and free edge stress

raisers play the main role in driving the damage propagation. In contrast to the unidirectional specimens, the damage sequence can be separated through all four damage modes.

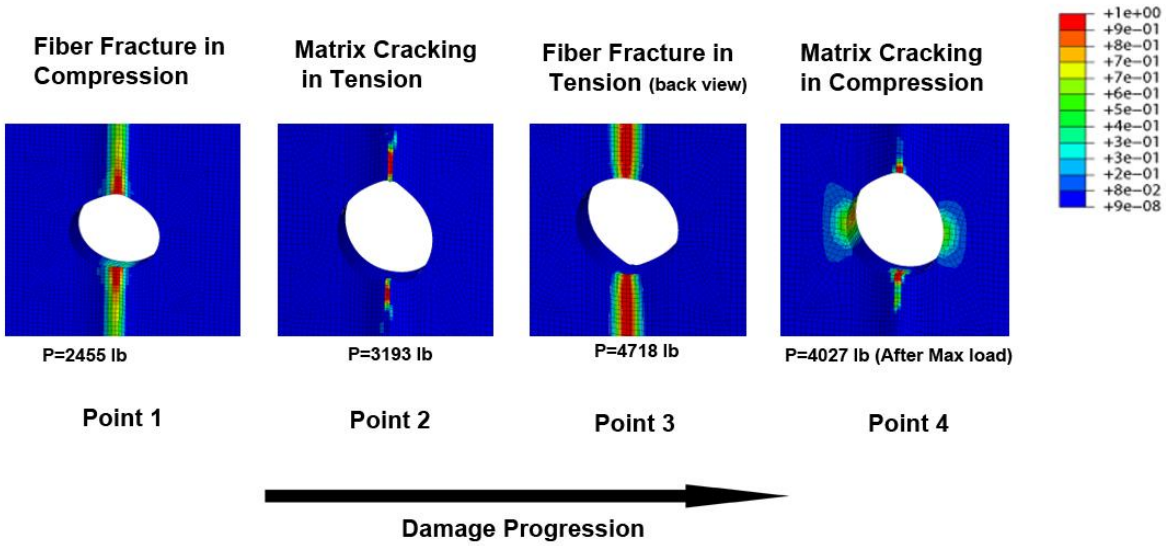


**Figure 4.22** Failure progression associated with four failure modes of Hashin's criteria in the OHC multidirectional laminate[140]

Decreasing the amplitude of waviness results in decreasing the contribution of the kinking stress whereas the effect of the interlaminar stress at the free edge is increased. However the overall results of the kinking strength are not affected by the angle plies in multidirectional laminates. The highest ply mismatch appears to favor the path of delaminations at -45°/90° and 0°/45° as it can be clear in Figure 4.17 showing a close-up of the waviness zone in representative multidirectional specimens. Matrix failure in tension for the multidirectional laminates is initiated at the hole in the vertical direction along the waviness zone.

Figure 4.23 contains a comparison between the two types of failure criteria where the model with the interlaminar strength prediction has better and conservative match with experiment.

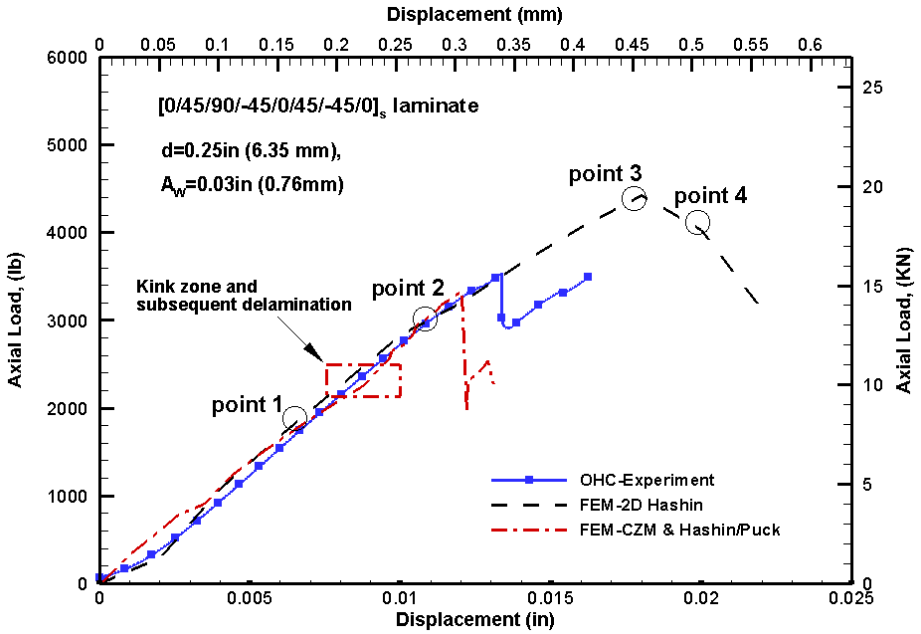


**Figure 4.23** Failure initiation associated in multidirectional OHC laminate

The results of the three modelling approaches are tabulated in Table 4.8.

**Table 4.8** Numerical and experimental comparison of Unidirectional and multidirectional laminate strength in a OHC specimen

| Waviness amplitude 0.83mm (0.032in) | $X_C$ experiment, R=0.25in (6.35 mm) Mpa (Ksi) | $X_C$ FE[1], R=0.25in (6.35 mm) Mpa (Ksi) | $X_C$ FE[2], R=0.25in (6.35 mm) Mpa (Ksi) |
|---|---|---|---|
| Unidirectional | 169.6 (24.6) | 165.7 24.0 | 161.1 23.3 |
| Multidirectional | 168.9 (24.5 ) | 192.3 27.9 | 163.6 23.7 |

FE[1] 2D Hashin model

FE[2] CZM and Hashin/Puck model

## 4.3 Damage evolution in tension tests

The OHT tests have been performed for multidirectional laminates with two levels of waviness and for unidirectional laminate with one level of waviness. The test observation demonstrates the dominancy of the interlaminar failure for both unidirectional and multidirectional specimens (Fig. 4.24 and 4.25). As it can be seen from Table 4.10, the strength is almost doubled relative to the OHC tests for multidirectional laminates.

The specimens were tested in tension according to the ASTM D5766 [65] standard for the open-hole tension strength of polymer composites with the exceptions of the deviations noted with layups and the proposed inclusion of the fiber waviness zone. Sample preparation and measurement of specimen dimensions was performed according to [147].

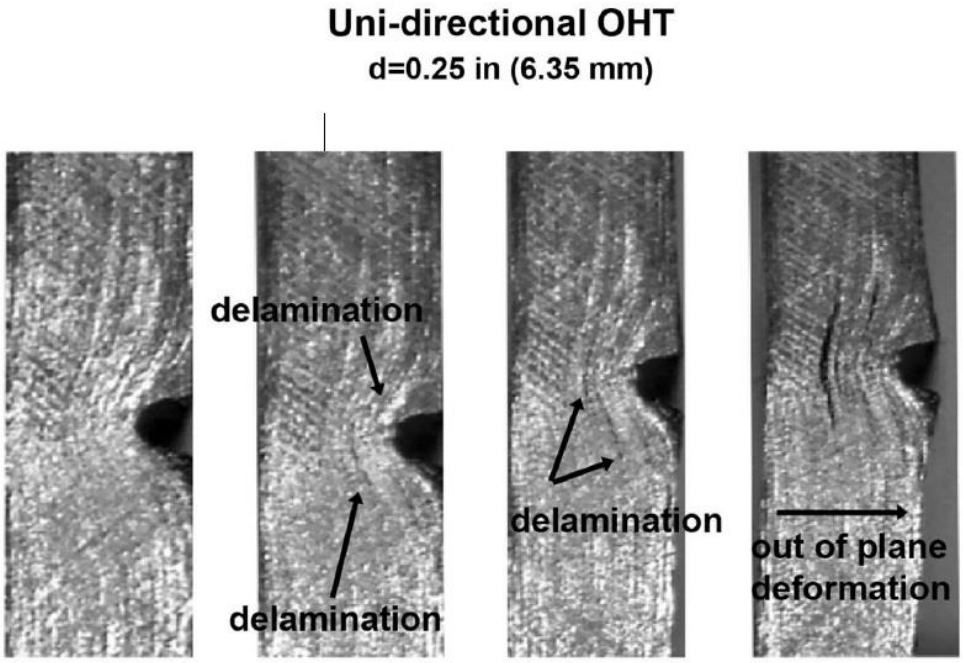


**Figure 4.24** Optical micrographs showing the failure sequence in unidirectional OHT specimens through the thickness of the specimen[140]

The Optical Micrographs (Fig 4.24) showss the failure sequence in unidirectional OHT specimens through the thickness of the specimen where the bending is progressively increased at the waviness zone. The out of plane bending deformation derive interlaminar crack onset. The interlaminar crack initiation propagates in between layers causing significant delaminations.

The load displacement response is largely linear until final failure observed for both the specimens with the two levels of waviness. This is mainly due to the high stress concentration near the hole which dominates the overall laminate failure as the kinking mechanism is diminished. No quasi-brittle damage deformations are captured in the load-displacement curves before final failure.

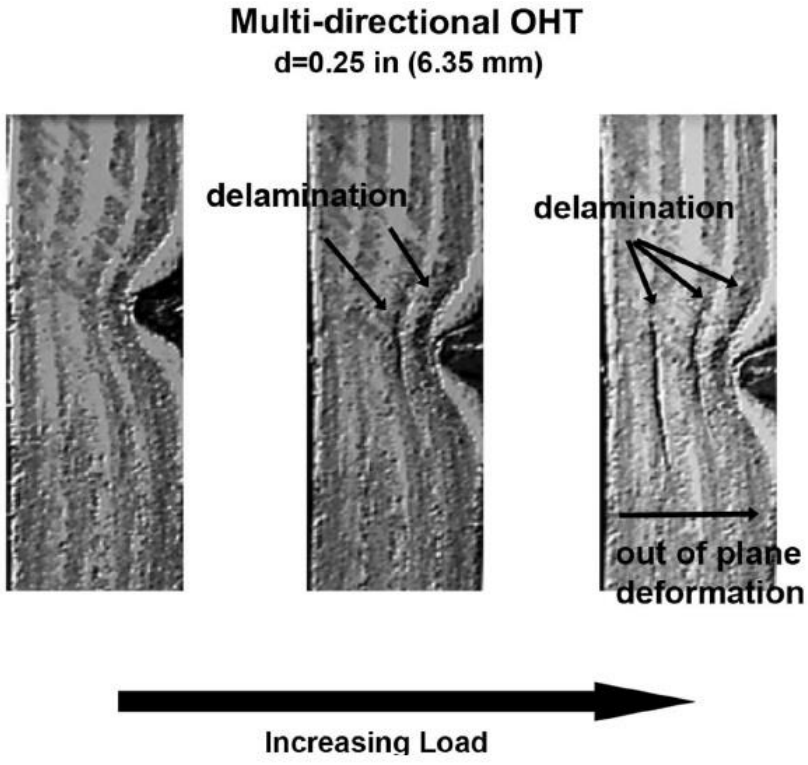


**Figure 4.25** Optical micrographs showing the failure sequence in multidirectional OHT specimens through the thickness of the specimen

Optical Micrographs (Figure 4.25) demonstrates the same damage response as unidirectional specimens. The failure sequence in multidirectional OHT specimens through the thickness of the specimen shows less undesired bending at waviness zone since part of the remote stresses are transferred as in-plane shear through the layers.

The front view of the OHT test (Figure 4.26) shows the shear failure in multidirectional specimens appears at the angled plies at the waviness zone near free edges.

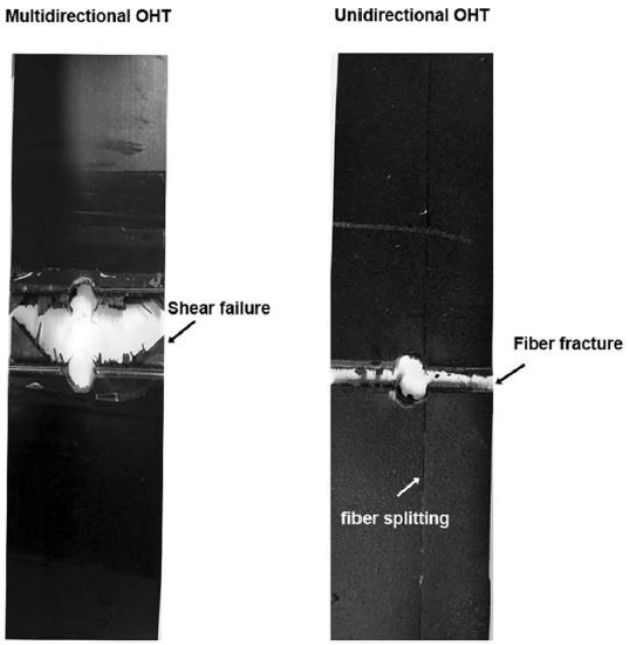


**Figure 4.26** Photograph of OHT specimens after ultimate stress[140]

Figure 4.27 shows the FE results of the damage onset for the multidirectional laminates. As it can be seen from Fig. 4.27, the failure load of the OHT is relatively higher than the OHC tests for multidirectional laminates. The free edge failure is almost disappeared from the damage onset however it is propagated towards the free edges as the damage propagates. Kinking failure is obviously diminished from the entire failure process.

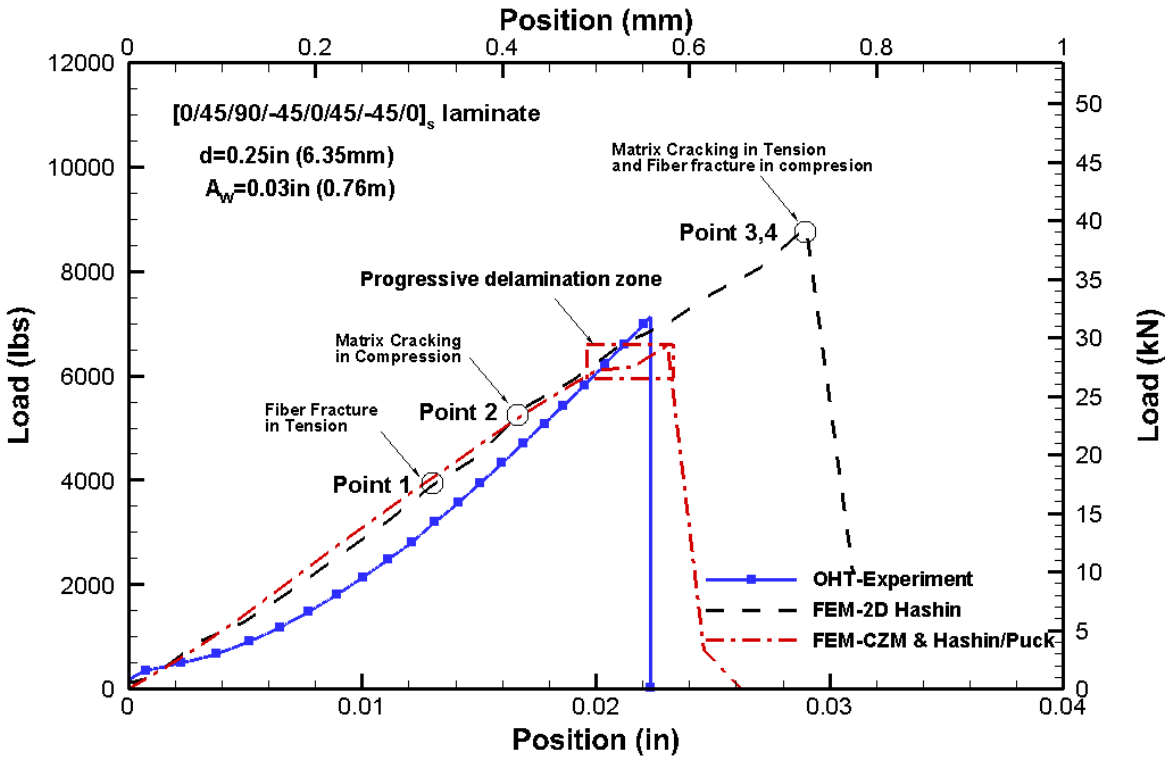


**Figure 4.27** FE prediction of the damage initiation and propagation sequence in a Multidirectional laminate OHT test[140]

Figure 4.27 shows the Hashin/Puck's with CZM approach can predict the load carrying capacity of the wrinkled specimens with about 7% error.

The investigation shows that only point 3 at the end of the final failure shows free edge failure where the entire waviness region experiences the failure (No free edge failure in Figure 4.28 in the cut view). Note that the fiber failure in tension is also deactivated until final failure which occurs for the fiber on the back of the laminate.

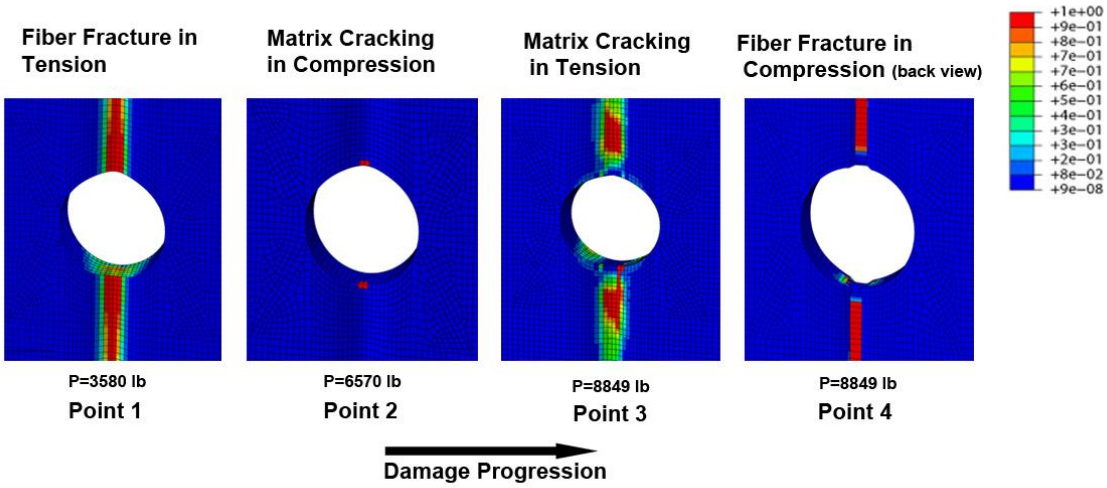


**Figure 4.28** Damage progressions in multidirectional OHT specimens[140]

The optical measurements were performed using a 3D DIC system which previously described. Figure 4.29 shows how the out of plane displacement is increased due to the presence of the waviness zone. This correlates well with the deformation pattern observed in the finite element model. The waviness zone creates a local eccentricity in the load path creating the localized bending in the specimen.

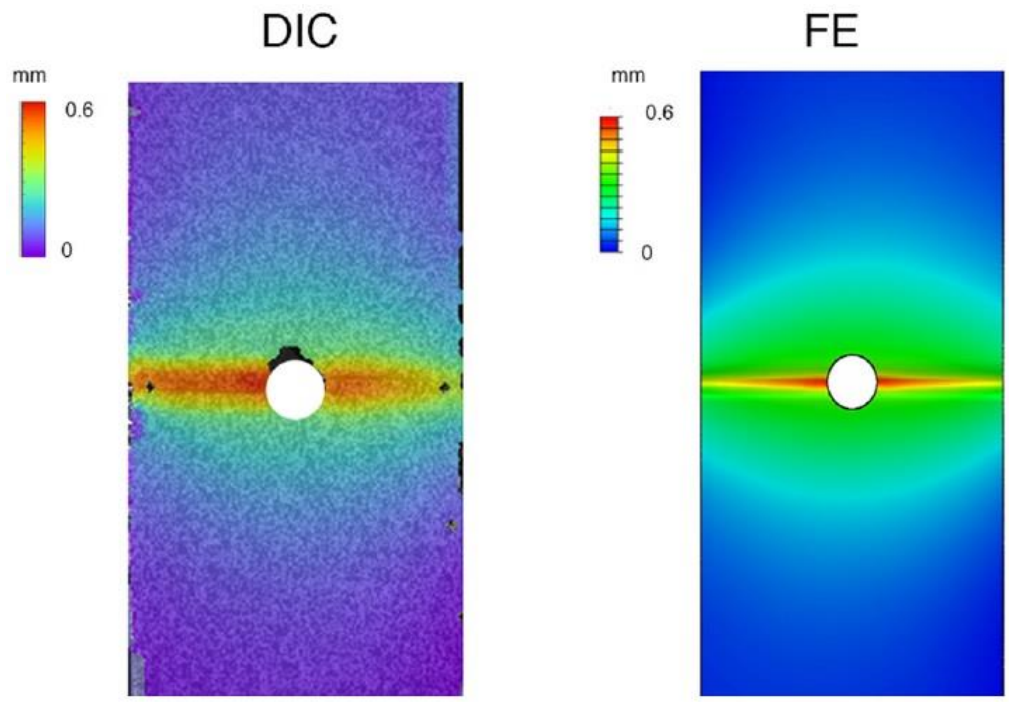


**Figure 4.29** Out of plane displacement of an OHT multidirectional specimen with a defect from 3D-DIC and FE model near the ultimate stress level of 5500 lbs (24.5 kN)

The failure progression of the OHT unidirectional laminate with the amplitude of 0.03 in waviness is obtained from the FE model is shown in Figure 4.30. Table 4.9 summarizes the failure stresses of the specimens in a notch size and a representative waviness. The experiment and the FE analysis have shown a conservative correlation with CZM and Hashin/Puck model confirming the effect of interlaminar failure effects.

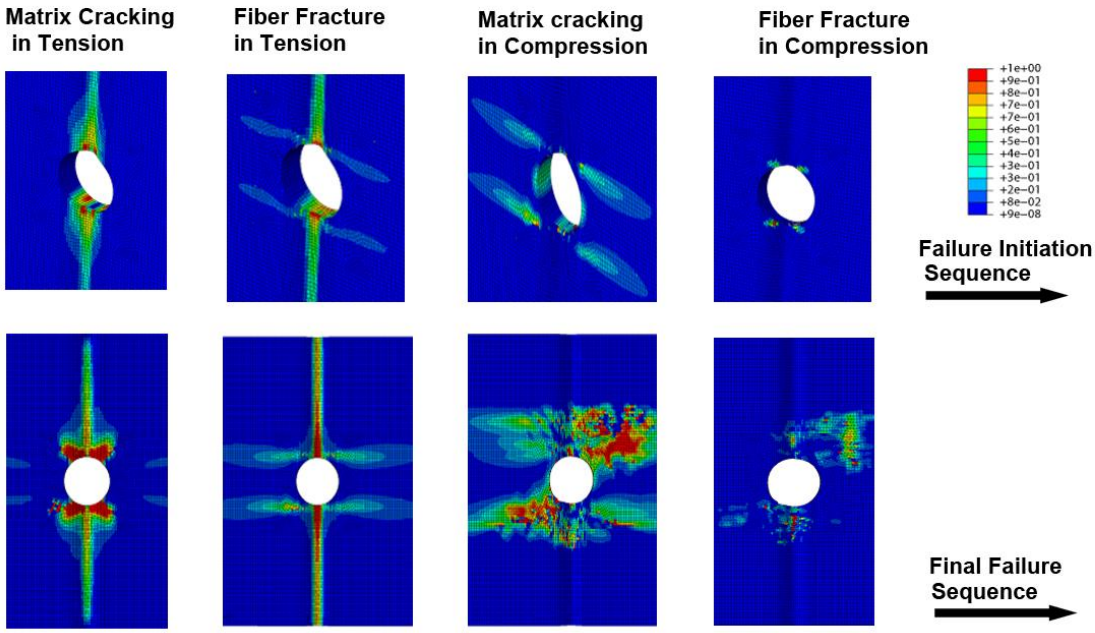


**Figure 4.30** Final failure associated with four modes of Hashin's criteria in the OHT unidirectional laminate[148]

**Table 4.9** Summary of test results from open-hole tension multidirectional specimens

| $A_w$ mm (in) | $X_T$ Experiment, Mpa (Ksi) | $X_T$ FE[1] Mpa (Ksi) | $X_T$ FE[2] Mpa (Ksi) |
|---|---|---|---|
| 0.889 (0.0350) | 350.16 (50.786) | 423.3 61.4 | 329.6 47.8 |

R=0.25 in (6.35 mm)

FE[1] 2D Hashin model

FE[2] CZM and Hashin/Puck model

These main differences observed in failure mechanisms between the OHT and the OHC tests of waviness specimens makes the OHC samples vulnerable to premature failures.

Fiber fracture initiation in the tension mode of failure begins asymmetrically emerging in the laminate asymmetric bending and twisting under the effects of defects.

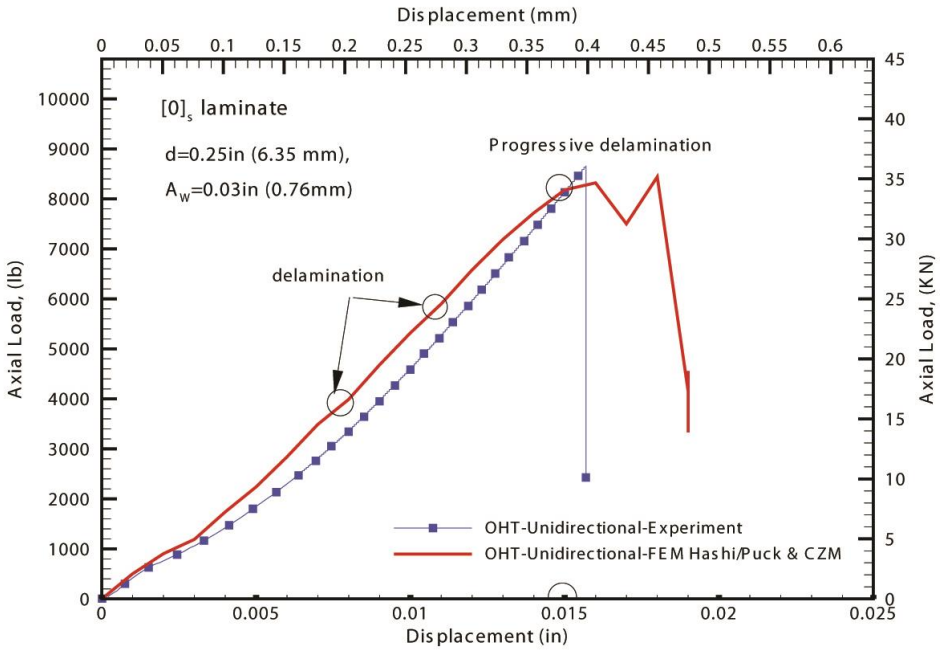


**Figure 4.31** FE prediction of the damage initiation and propagation sequence in a unidirectional laminate OHT test

The results of the experiments are compared with the FE model in Figure 4.31. There is a comparable agreement with the numerical results and the experiments.

# CHAPTER 5

# LIMIT POINT DETERMINATION

This chapter is devoted to proposing a new method determining the limit point in composite materials which can be used in design considerations of laminated composite structures. The limit point is proposed based on the z-displacement or out-of-plane displacement tracking using an image correlation method to determine the start of incipient interlaminar delamination in continuous fiber reinforced composite materials. The maximum principal strain is used to identify the hot spot stress location for construction of an evaluation line. The z-displacement along this evaluation line is then tracked as the specimen is loaded. Differentiation of the z-displacement field results in peaks that are subsequently used to identify the limit point of the composite material.

## 5.1 Limit point determination using the DIC method

In this study, a new methodology to determine the limit point is proposed based on the z-displacement or out-of-plane displacement tracking using an image correlation method to determine the start of incipient interlaminar delamination in continuous fiber reinforced composite materials. The method is based on using a two-camera 3D-DIC setup for observation of the surface of the composite material during a normal tension test for capturing of the in-plane and out-of-plane deformations. The maximum principal strain is used to identify the hot spot stress location for construction of an evaluation line. The z-displacement along this evaluation line is then tracked as the specimen is loaded. Differentiation of the z-displacement field results in peaks that are subsequently used to identify the limit point of the composite material.

In this section, procedure used to identify the limit point and the onset of interlaminar damage is discussed. The procedure is based on tracking the changes of the surface topography of the specimen. The procedure involves the following:

(1) The test specimen is loaded until failure in a typical fashion as is currently performed and is observed with a pair of CCD cameras and recorded by the DIC system. The specimen surface is observed. The test is only stopped at ultimate failure of the specimen. The collected data is then used for analyzing the surface topology in the post processing stage.

(2) Using the obtained DIC measurements and load-frame information, the maximum principal engineering strain right before fracture or after images were no longer captured is identified to reveal the location where the failure is likely to occur. Note that the actual value of the strain is dependent on the smoothing parameters, but for this procedure, the actual value is not critical since we are using it here as a method for identifying the evaluation line to capture the deformations. An evaluation line of length 20 mm (8 to 10

times the thickness of the specimen) is drawn perpendicular to this region to encompass the entire high strain region. This line is used to interrogate the surface topography changes as shown in Figure 5.1.

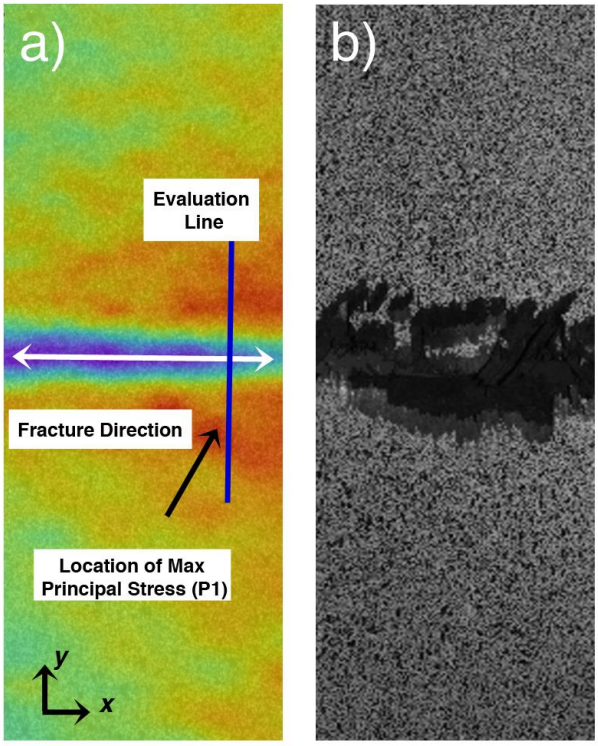


**Figure 5.1** An unnotched tension specimen with center wrinkle. In a) full-field image of maximum principal strain used to determine the evaluation line perpendicular to the fracture direction; b) shows the speckle pattern and the specimen after final fracture[149]

(3) The surface topography (z-displacement) along the evaluation line is determined from DIC post processing for all the captured images in the time history. Figure 5.2 shows the z-displacement along the evaluation line at different times during the test. Note that in the figure we show the displacement at every 10 steps to illustrate the changes. The maximum

displacement is seen from the image captured right before fracture.

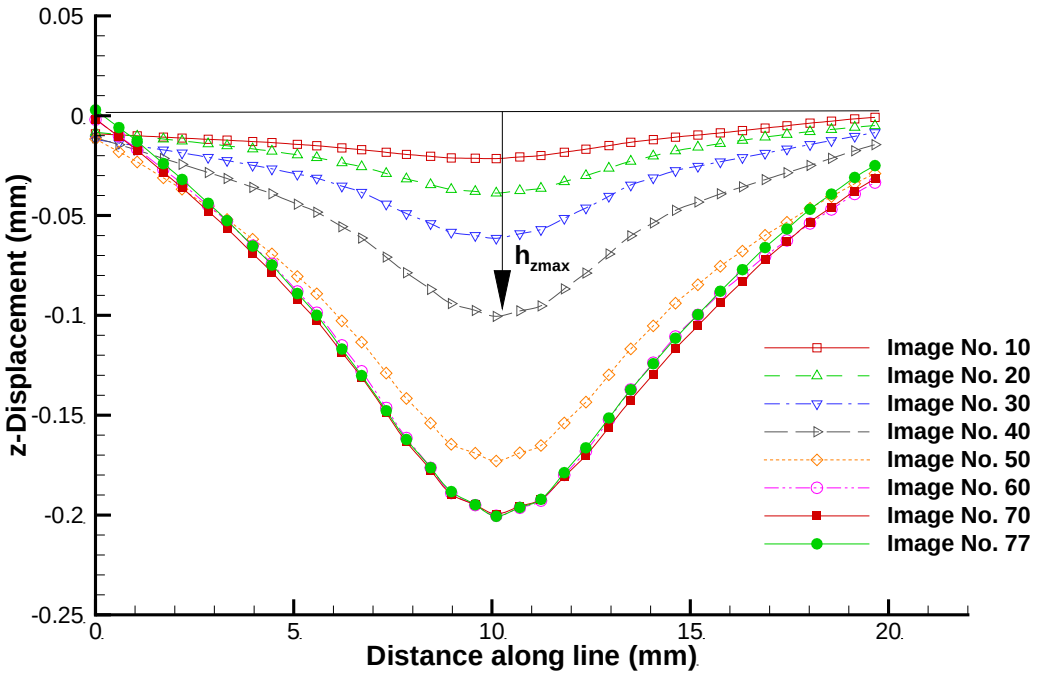


**Figure 5.2** Variation of the z-displacement along the evaluation line for Specimen 2 obtained from the 3D DIC method[149]

(4) The change in displacement is noted relative to the zero point and maximum value along the evaluation line. The change between the zero point assuming in-plane loading and the maximum observed z-displacement measurement is referred to as the z-displacement increment, $h_{z\max}$.

(5) The derivative of $h_{z\max}$ with respect to image number is then plotted to identify the limit point by identifying the jumps in the $h_{z\max}$ response in the history of images collected from the test.

## 5.2 Experiments

2D digital image correlation (DIC) was used to capture the strains on the surface of the composite specimen. The DIC technique uses a random speckle pattern applied to the specimen that is captured using a couple-charged device (CCD) camera. These images are then processed using correlation algorithms to compare strained maps to a reference image taken before the loading is applied. The procedure has been previously validated by the author on this material by comparing strain results obtained from DIC to finite element predictions for carbon/epoxy laminates with through thickness cutouts [150]. The digital image correlation was performed using the Dantec Dynamics Q-400 system. A resolution of 5 megapixels is used for the CCD camera together with a 50 mm Schneider Xenoplan lens. The DIC method is used for the purpose of comparing the strain fields with the FE models and detecting whether there has been unloading in certain areas of the specimen. Unloading was used as an indicator of subsurface delamination and/or possible twisting deformations. Prior to testing, a white flat spray paint is used to cover the surface of the composite. This is followed with application of a speckle pattern using black paint to create random small drops. Figure 5.3 shows the test specimen in the loading frame with the 2 CCD cameras used for 3D digital image correlation.

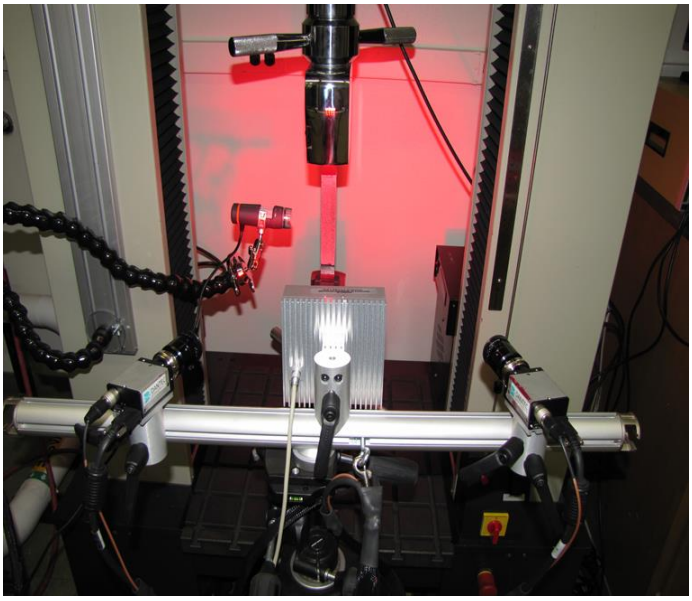

**Figure 5.3** Photo of test setup showing specimen in grips with stereo-camera setup and light emitting diode (LED) lighting. A video microscope is included to monitor the delaminations on the side of the specimen

Prior to observing the specimens during test, a series of calibration steps are performed on a calibration plate. The system interface displays real-time tracking of target markers and automatically acquires a series of 12 images of this calibration target positioned at different angles. This procedure allows for real-time evaluation of the success of the calibration process. Calibration is used for determination of the imaging parameters (intrinsic and extrinsic) of each of the cameras in addition to the position of the cameras relative to the overall coordinate system. An acceptable calibration was considered if the residuum was less than 0.3 pixels. The field of view observed contained the specimen and was approximately 150 mm. No filters were applied on the acquired images.

An output signal from the loading system is synchronized with the image correlation system so that each frame is correlated to the actual loads applied to the specimen at that point.

Approximately 80-100 images were recorded during each test at a frequency of 0.5 Hz. The initial image in the unloaded state was used for the reference for all the subsequent images. At the post processing stage, a grid size of 12 pixels and a facet size of 17 pixels were used for the evaluation. The specimens were tested in tension according to the ASTM D3039 [98] standard for tensile properties of polymer composites.

**Table 5.1** Description of specimens tested and DIC observation surface

| **ID** | **Wrinkle Height, A, mm** | **Wrinkle Length, L mm** | **3D-DIC Observation** | **Layup** |
|---|---|---|---|---|
| Specimen1 | 0.8 | 4.6 | Back | [0/45/90/-45/0/45/-45/0]s |
| Specimen2 | 0.8 | 4.6 | Back | [0/45/90/-45/0/45/-45/0]s |
| Specimen3 | 0.6 | 3.5 | Front | [0/45/90/-45/0/45/-45/0]s |
| Specimen4 | 0.6 | 3.5 | Front | [0/45/90/-45/0/45/-45/0]s |
| Specimen5 | 0.6 | 3.5 | Back | [0/45/90/-45/0/45/-45/0]s |
| Specimen 6 | 0.3 | 1.3 | Back | [0/45/90/-45/0/45/-45/0]s |
| Specimen 7 | 0.3 | 1.3 | Front | [0/45/90/-45/0/45/-45/0]s |
| Specimen 8 | 0.5 | 2.3 | Back | $[0/45/90/-45/0/45/-45/0]_s$ |
| Specimen 9 | 0.5 | 2.3 | Front | $[0/45/90/-45/0/45/-45/0]_s$ |
| Specimen 10 | 0.28 | 1.7 | Front | $0_{16}$ |
| Specimen 11 | 0.28 | 1.7 | Back | $0_{16}$ |
| Specimen 12 | 0.35 | 2.7 | Back | $0_{16}$ |
| Specimen 13 | 0.35 | 2.7 | Front | $0_{16}$ |

[1]Front denotes surface where resin pocket occurs.

The experiments were performed in a displacement control mode at a rate of 0.5 cm/min. No tabbing was performed on the specimens containing the waviness since the waviness zone creates an adequate stress concentration to cause the failure in the gage section.

During the tests, the cross-head displacement and load were recorded. The load was applied using an electromechanical test system with a 200 kN (22 kips) capacity. The details of the specimens tested are shown in Table 5.1. The failure near the waviness zone was also captured for some of the specimens using an optical microscope that was synchronized with the loading regime. The experimental setup consists of a pair of digital cameras observing the surface of a multidirectional carbon-epoxy specimen loaded in tension (Figure 5.4)

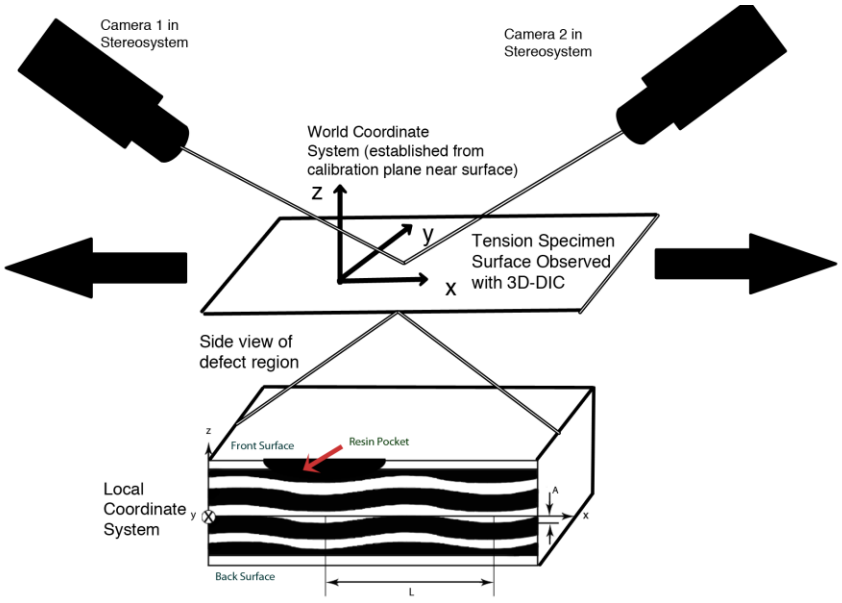


**Figure 5.4** Schematic of test setup and specimen details[149]

The calibration of the 3D-DIC setup is performed near the surface of the specimen. The measured deformations are captured relative to this coordinate system on the composite specimens.

**5.3 Results**

Full field observations of the deformation on the surface of the composite specimen allows for overall tracking of the specimen through small movements during the test. In addition to being able to extract the gage strains on the specimens using DIC, the deformation information provides even more useful information about the material state. It is apparent from this information that the defects introduced in the specimen result in the development of localized bands of out-of-plane deformations in the vicinity of the defect zones (Figure 5.5).

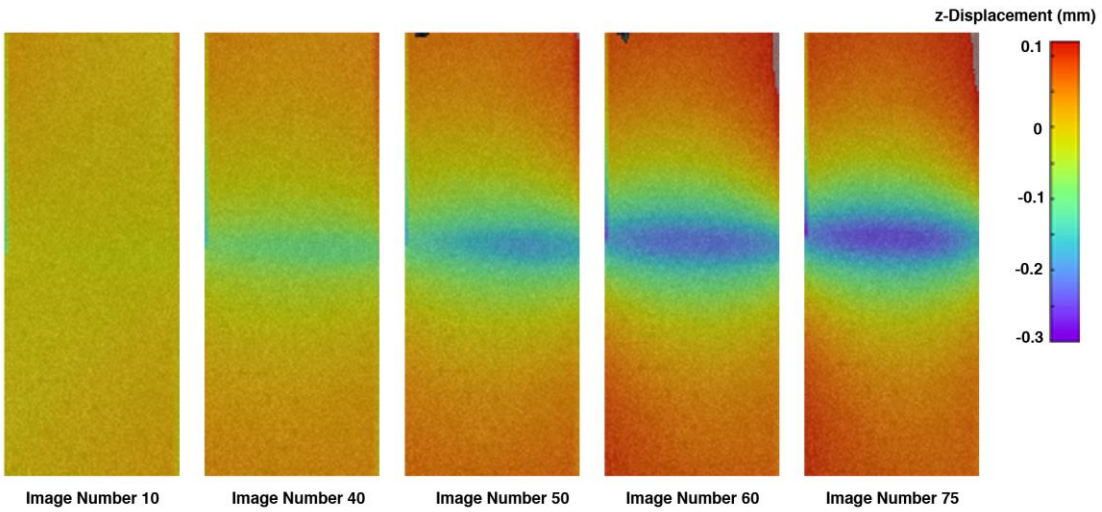


**Figure 5.5** Development of out-of-plane z-displacement field on the back surface during the tension test (specimen 2). Note the defect zone near the center[149]

These deformations develop due to the eccentricity in the load path introduced by the defect at the local level and the disruption of the material symmetry at the local level. The out-of-plane deformation away from the defect zone is relatively small and is typical of a uniaxial test on a symmetric laminate. The direction of the out-of-plane movement is found to be dependent on the face the specimen is observed (Table 5.2).

**Table 5.2** Limit point stresses and z-displacements obtained using the proposed technique

| ID | Limit Point z-displacement, mm | Limit Point Stress, MPa | Ultimate Stress (with defect), MPa | Ratio of Limit to Ultimate Stress (with defect) | Ratio of Limit to Ultimate Stress (control[1]) |
|---|---|---|---|---|---|
| Specimen1 | -0.04 | 81.9 | 433.3 | 0.19 | 0.11 |
| Specimen2 | -0.06 | 110.6 | 414.4 | 0.27 | 0.14 |
| Specimen3 | 0.12 | 213.5 | 596.7 | 0.36 | 0.28 |
| Specimen4 | 0.10 | 189.7 | 529.1 | 0.36 | 0.25 |
| Specimen5 | -0.06 | 203.5 | 504.0 | 0.40 | 0.27 |
| Specimen 6 | -0.018 | 180.5 | 530.5 | 0.34 | 0.24 |
| Specimen 7 | 0.023 | 229.7 | 586.1 | 0.39 | 0.30 |
| Specimen 8 | -0.02 | 221.8 | 535.0 | 0.41 | 0.29 |
| Specimen 9 | 0.06 | 169.8 | 447.3 | 0.38 | 0.22 |
| Specimen 10 | 0.08 | 434.8 | 971.4 | 0.44 | 0.24 |
| Specimen 11 | -0.045 | 419.0 | 966.6 | 0.43 | 0.23 |
| Specimen 12 | -0.09 | 241.1 | 729.9 | 0.33 | 0.14 |
| Specimen 13 | 0.06 | 251.5 | 720.4 | 0.35 | 0.14 |

[1]The ultimate stress on control specimens without defects were previously reported in [12]

Since the images captured are correlated to the stress level it is also possible to accurately measure any small changes or jumps in the displacement response. The jumps in the z-displacement are caused by internal instabilities caused by the defect and identification of the times where these instabilities occur allow for identification of the limit point of the composite material.

The experimental results show consistent observations regarding the out-of-plane or z-displacement observed for all the specimens. Figures 5.6 to 5.11 [149]show the z-displacement increment $h_{z\max}$ versus stress for the specimens tested.

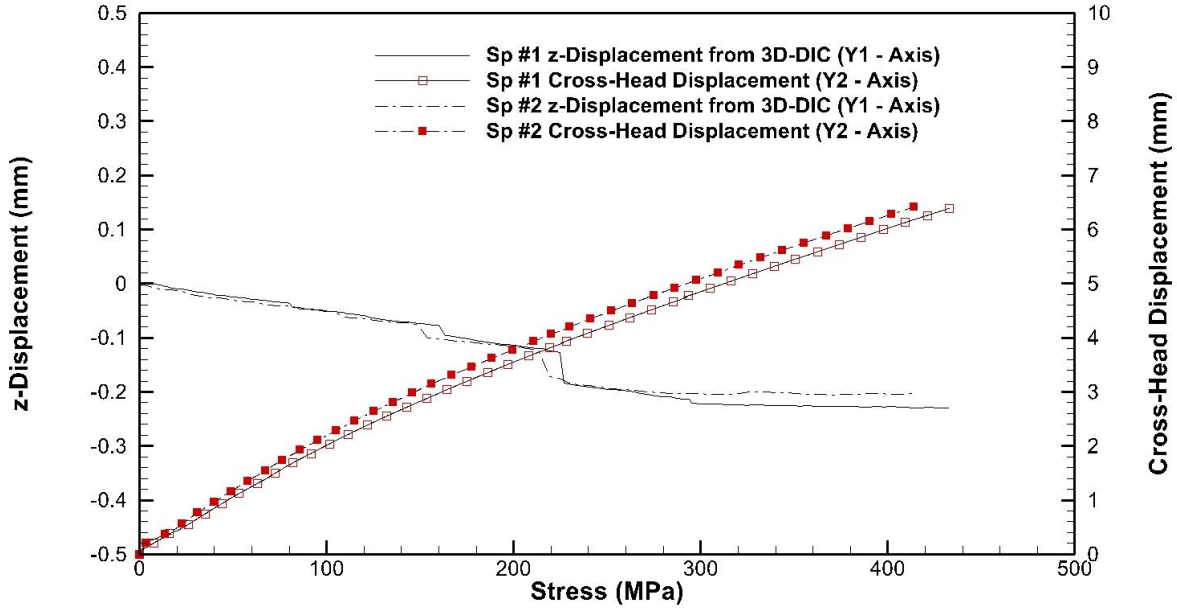


**Figure 5.6** Z-displacement increment, $h_{z\max}$ versus axial stress (Sp#1,2). Also plotted is cross-head displacement (on Y-2 axis) versus stress for the same specimens

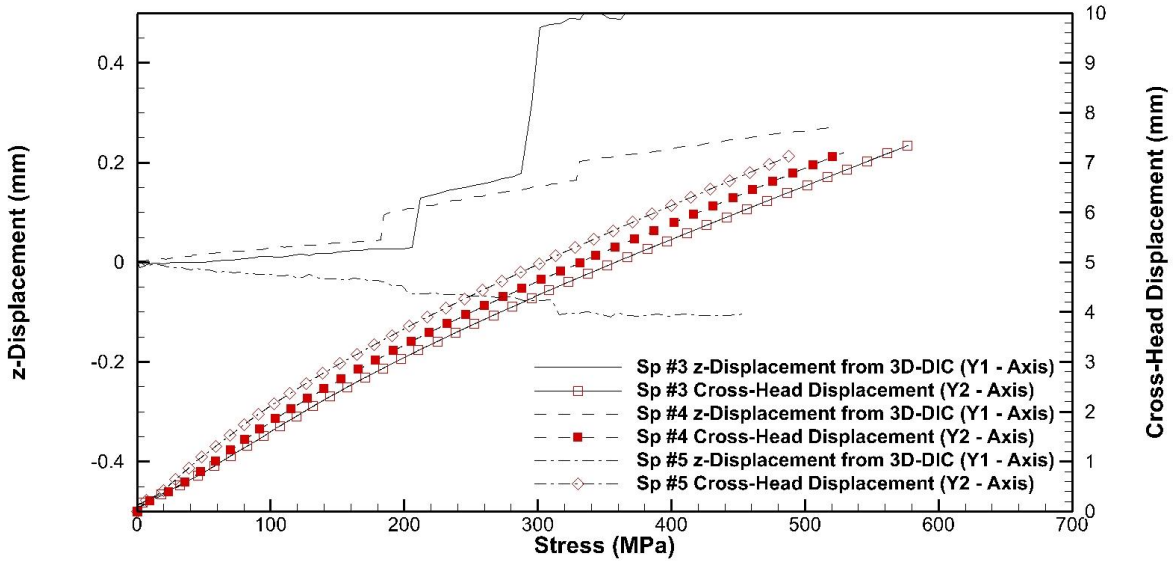


**Figure 5.7** Z-displacement increment, $h_{z\max}$ versus axial stress (Sp#3, 4, 5). Also plotted is cross-head displacement (on Y-2 axis) versus stress for the same specimens

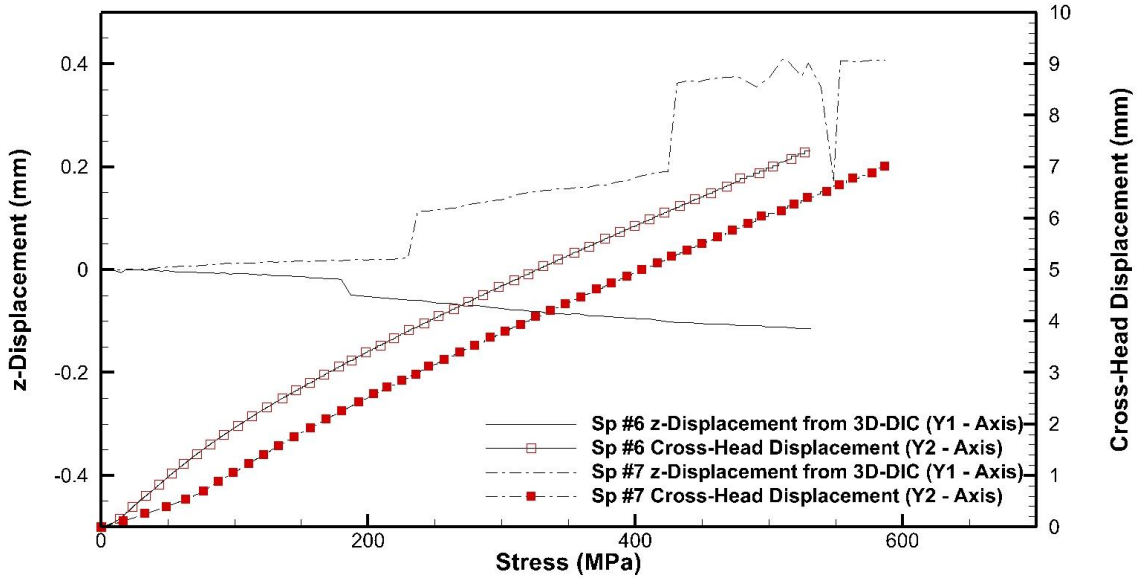


**Figure 5.8** Z-displacement increment, $h_{z\max}$ versus axial stress (Sp#6, 7). Also plotted is cross-head displacement (on Y-2 axis) versus stress for the same specimens

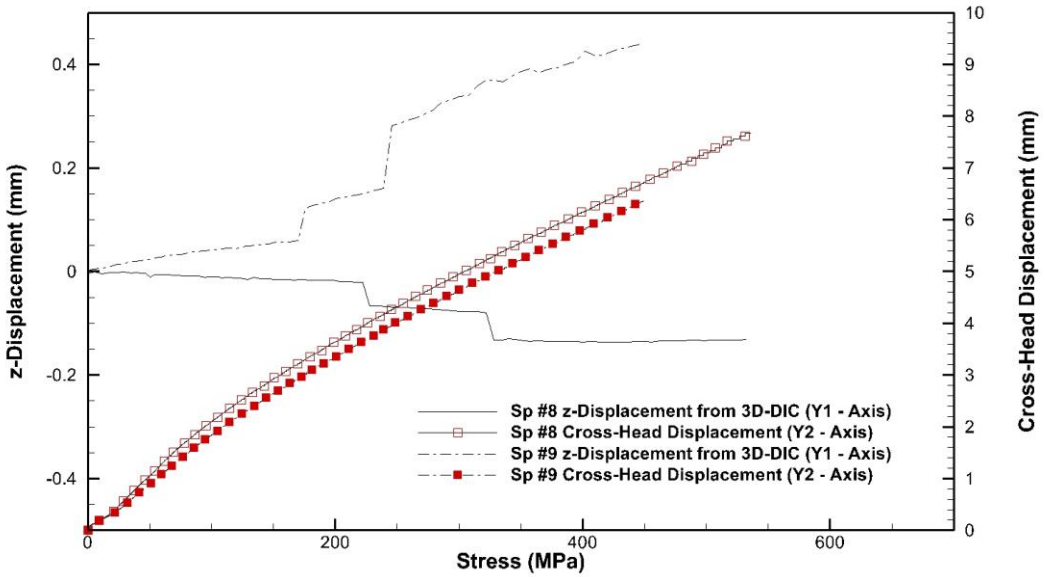


**Figure 5.9** Z-displacement increment, $h_{z\max}$ versus axial stress (Sp#8, 9). Also plotted is cross-head displacement (on Y-2 axis) versus stress for the same specimens

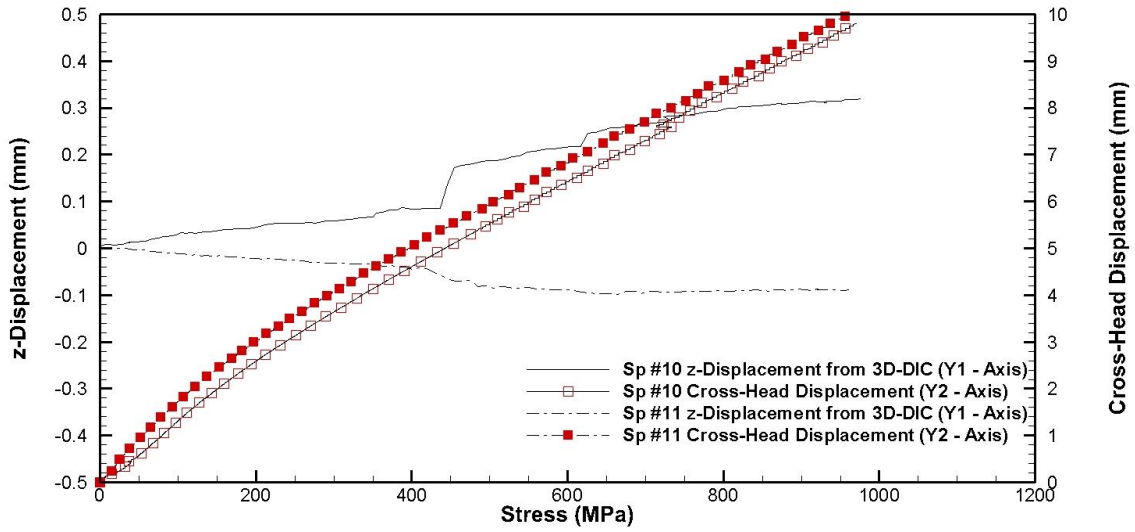


**Figure 5.10** Z-displacement increment, $h_{z\max}$ versus axial stress (Sp#10, 11). Also plotted is cross-head displacement (on Y-2 axis) versus stress for the same specimens

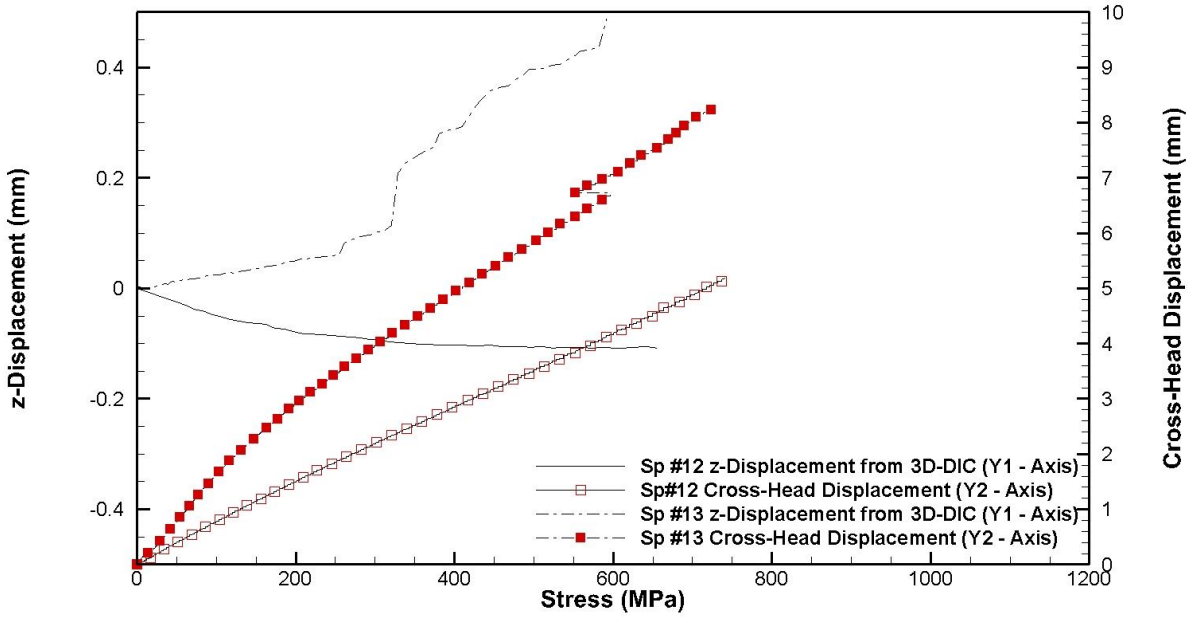


**Figure 5.11** Z-displacement increment, $h_{z\max}$ versus axial stress (Sp#12, 13). Also plotted is cross-head displacement (on Y-2 axis) versus stress for the same specimens

Some specimens were tested with the DIC observation on the front face containing the wrinkle resin pocket and some were tested with the DIC observation on the back face which did not show any resin pocket accumulations (Table 5.1). Both surfaces of the specimens were completely flat whether they had a resin pocket or not. The results of the post-processing show that the face containing the resin pocket displays a positive z-displacement map in the vicinity of the fiber waviness zone whereas the specimens observed on the back surface indicated a negative z-displacement. Consistent with the microscopic observation, the displacement measured was less than 0.25 mm for the back surface and less than 1mm for the front surface observations as shown in Figure 5.6 to 5.11. The displacement value is higher when observed from the front side (or that containing a resin pocket) and is likely due to the limited constraint and higher Poisson's ratio of the resin pocket compared to the back surface inspection where such conditions do not exist.

There was also a correlation observed between the z-displacement observed and the severity of the fiber waviness in the specimen where a more severe waviness defect results in a higher absolute displacement value. This observation may have an impact on nondestructive examination of composite structures where the z-displacement can be used as an indicator of waviness damage after application of a test load.

An examination of the $h_{z\max}$ response versus the stress on the specimen shows clear jumps in the response. Note that these jumps in the z-displacement are not correlated with any observable load drops in the cross-head displacement versus the axial stress on the specimen. Figure 5.12 shows a side view of the specimen and the interlaminar damage as it develops through load application as observed inside the specimen.

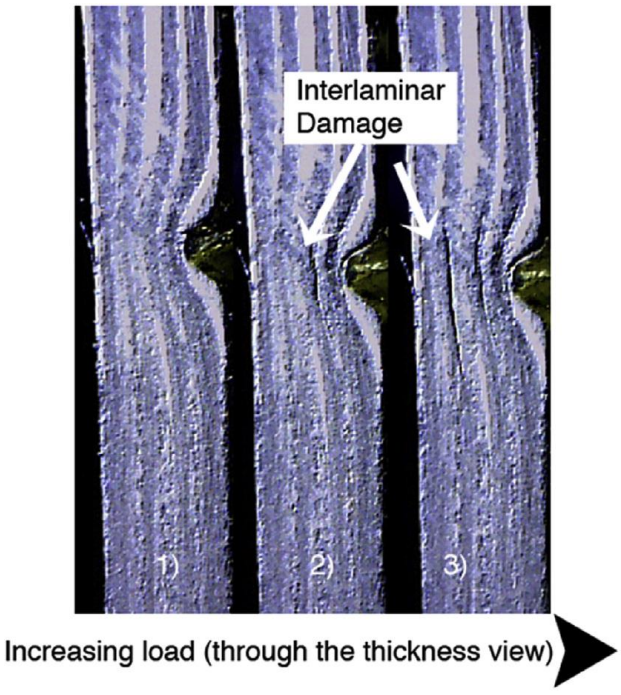


**Figure 5.12** Progression of damage in the tension coupon as viewed using a microscope at the side of the specimen.

It is confirmed that the jumps in the z-displacement observed are related to the interlaminar damage events observed using the optical video microscopy method. The peaks of the z-displacement used to identify the limit points of the composite material are determined by considering the derivative of, $h_{z\max}$ with respect to time. This can be seen in Figures 5.13 to 5.18 [149]where $\Delta h_{z\max} / \Delta t$ is plotted versus image number.

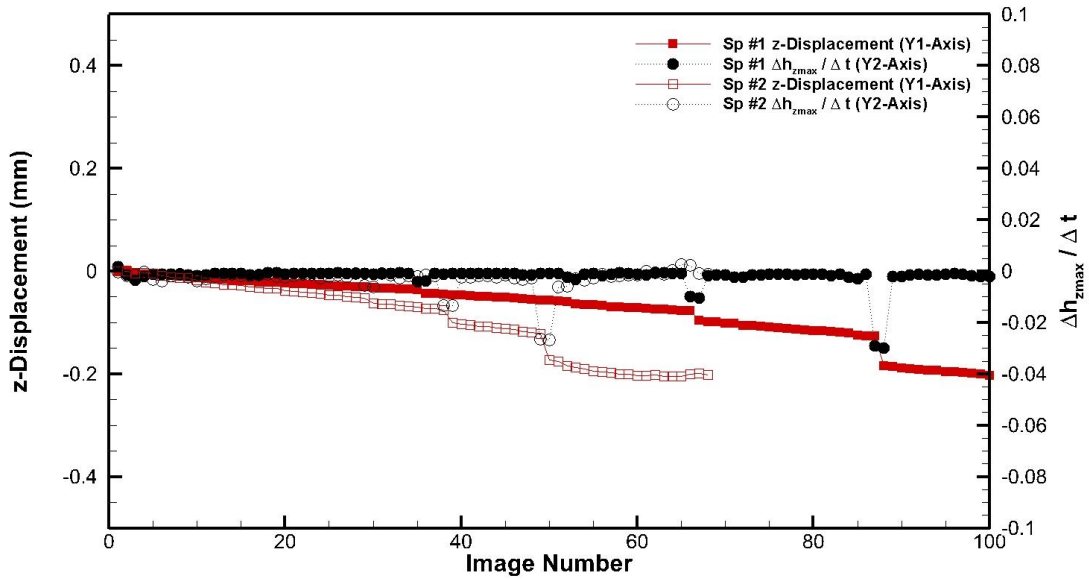


**Figure 5.13** Z-displacement increment, $h_{z\max}$ versus image number and superimposed with the derivative of the z-displacement to identify the limit point in the tension specimens 1 and 2

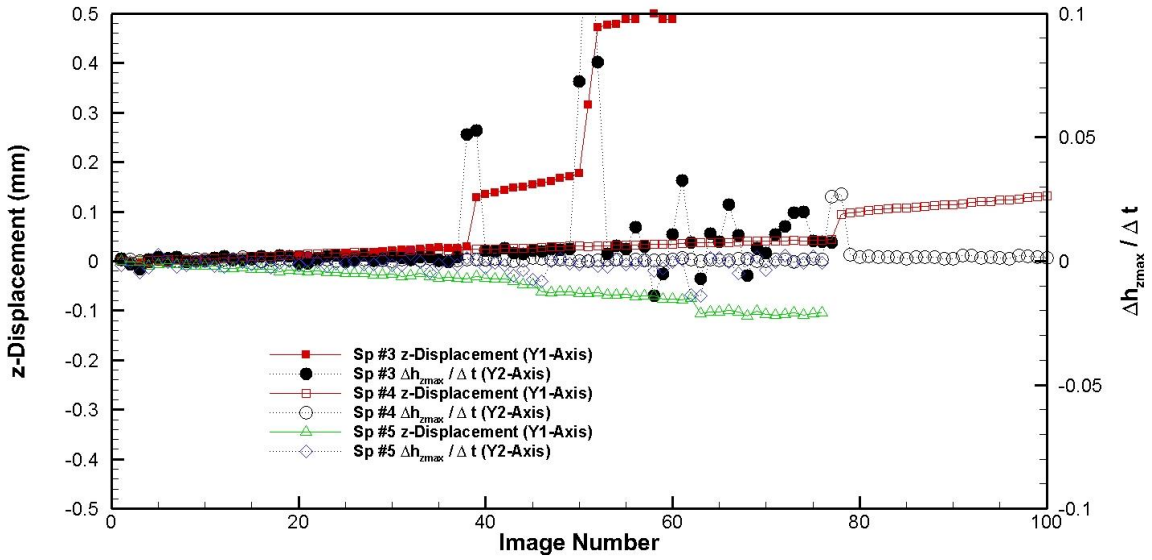


**Figure 5.14** Z-displacement increment, $h_{z\max}$ versus image number and superimposed with the derivative of the z-displacement to identify the limit point in the tension specimens 3, 4 and 5

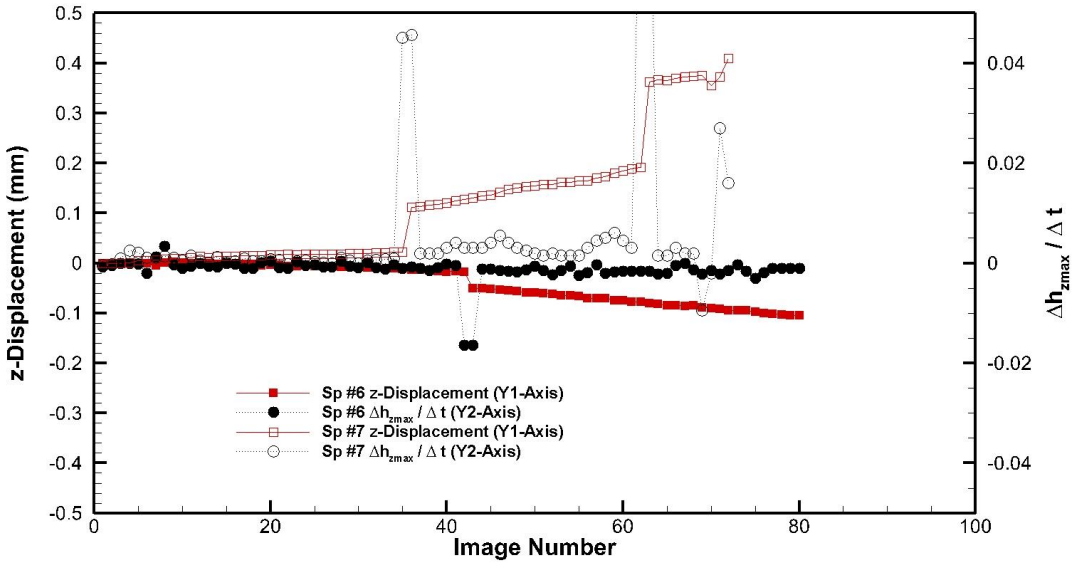


**Figure 5.15** Z-displacement increment, $h_{z\max}$ versus image number and superimposed with the derivative of the z-displacement to identify the limit point in the tension specimens 6 and 7

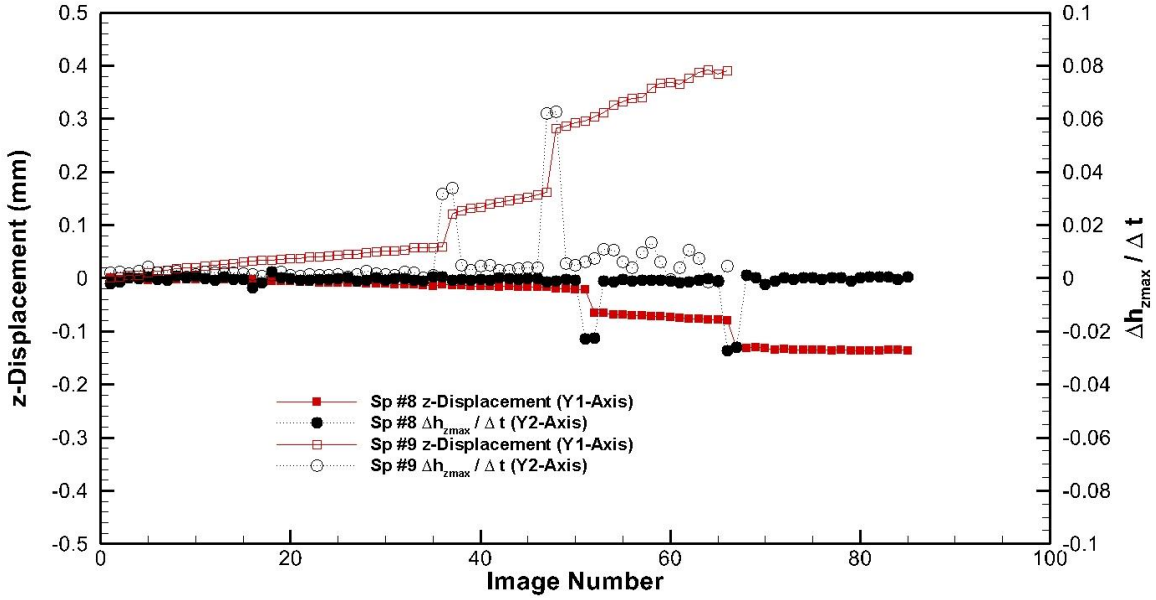


**Figure 5.16** Z-displacement increment, $h_{z\max}$ versus image number and superimposed with the derivative of the z-displacement to identify the limit point in the tension specimens 8 and 9

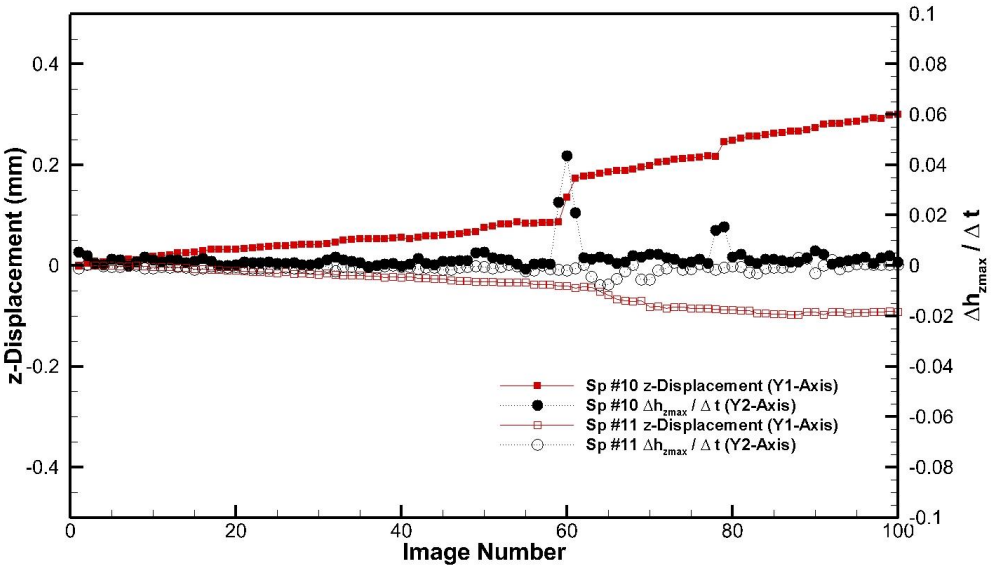


**Figure 5.17** Z-displacement increment, $h_{z\max}$ versus image number and superimposed with the derivative of the z-displacement to identify the limit point in the tension specimens 10 and 11

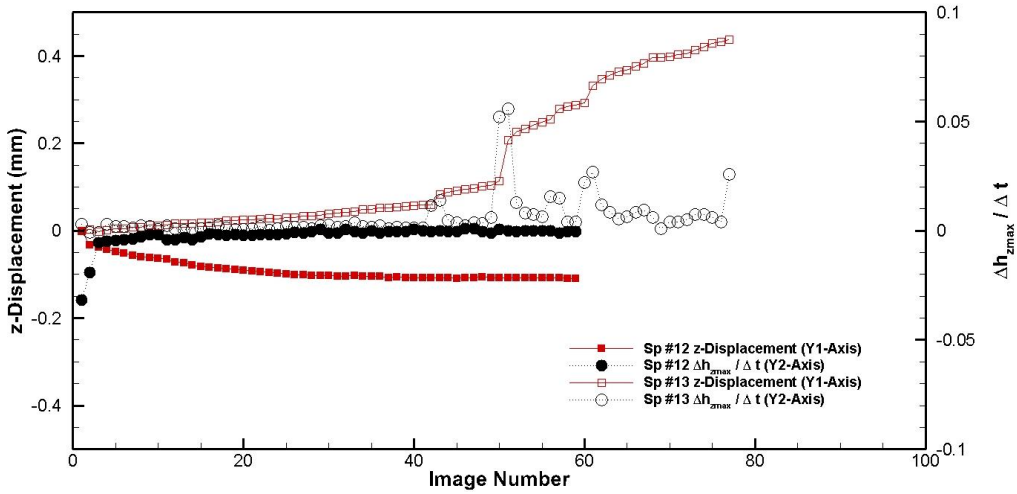


**Figure 5.18** Z-displacement increment, $h_{z\max}$ versus image number and superimposed with the derivative of the z-displacement to identify the limit point in the tension specimens 12 and 13

Several peaks are seen in this plot corresponding to internal instabilities in the material during the test caused by internal interlaminar failures. The first peak in this plot is used to identify the limit point of the composite material. Since the 3D-DIC measurements are synchronized with the loading machine it is possible to then determine the limit point stresses (Table 5.2). Note that the displacement measurement is preferred over in-plane strain since the strains do not show the same sensitivity to internal instabilities such as delamination initiation and growth. They are also more dependent on the post-processing approach than displacement fields. Note that specimen 12 with lower stiffness was preloaded to 600 MPa and then re-tested with DIC. No jumps in the z-displacement response was observed suggesting that a material that has been loaded beyond its limit point will not show jumps in the z-displacement behavior when reloaded. A comparison of the ratio of the limit point stresses to ultimate stresses is shown in Table 5.2. The ratio is shown

as a function of ultimate stresses from the specimens containing defects studied in this paper and control specimens with no defects previously reported in the literature.

**Limitations:** The method presented here is feasible for determining the limit points in unidirectional and multidirectional composite materials tested under tension, thus while one material is shown here on carbon-fiber/epoxy, further validation on other material systems is necessary.

The additional study of some of the test parameters shows that the frame rate can also affect the peak amplitude. However, for the three frame rates selected in a sub-study, the peak was easily identifiable (Figure 5.19a). A local regression filter can also improve the peak detection in some cases. The results in Figure 5.19b show that a local regression filter can help reduce the noise near this localized deformation event thus enabling better detection of the limit point.

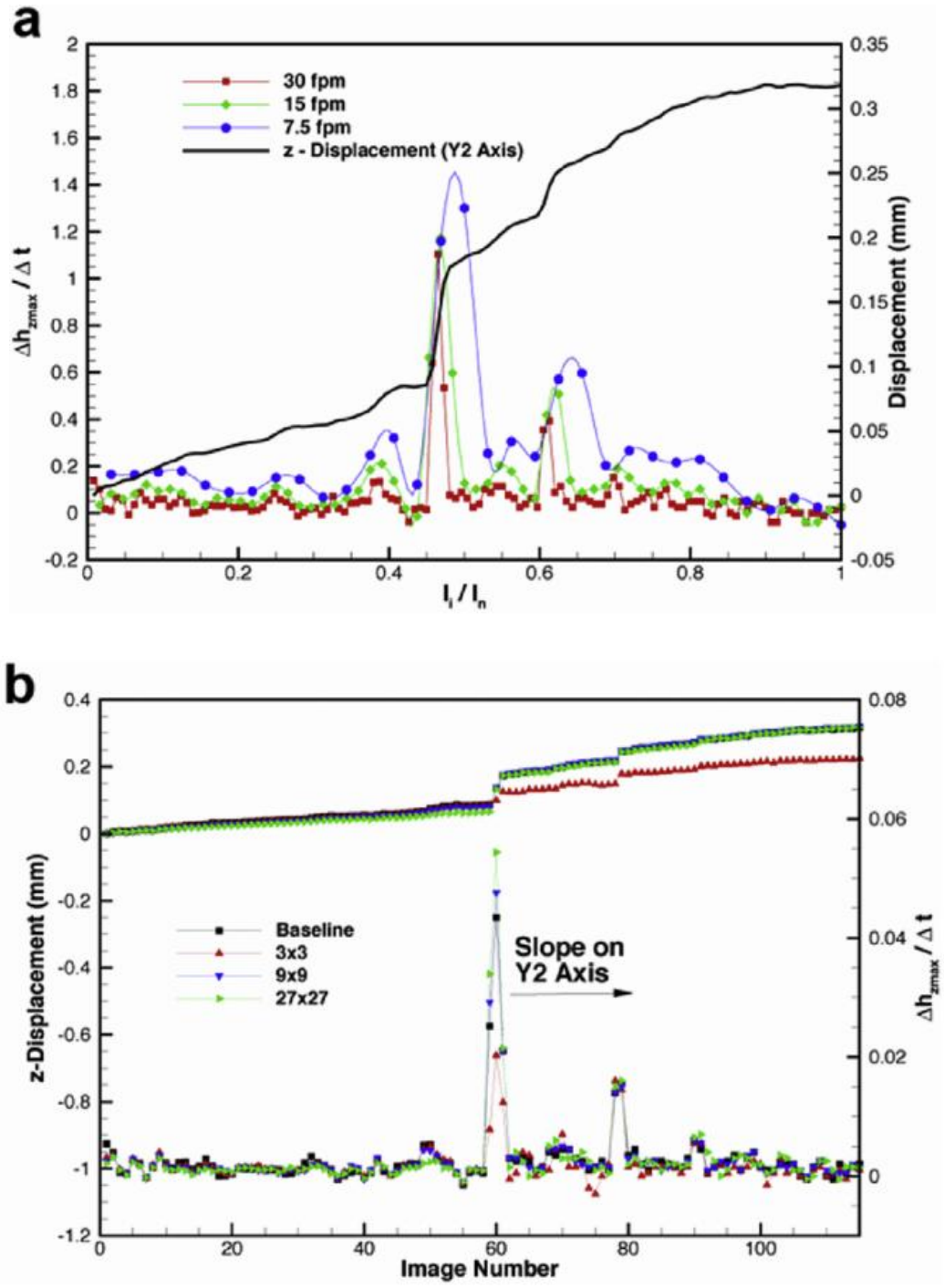


**Figure 5.19** Effects of (a) image acquisition rate (b) local regression filter on limit load peaks[149]

Noise in the experimental measurements can cause some small jumps to be missed especially in materials with low levels of fiber waviness. One approach to handle this issue is to establish an amplitude and slope threshold for a given material system to detect the peaks. It is also possible to smooth the original out-of-plane displacement curve before performing the derivative function to detect the zero crossings associated with the peaks. However, there are drawbacks with this approach that can result in over smoothing and removing the peaks.

# CHAPTER 6

# HYBRID NUMERICAL AND HYPERSPECTRAL IMAGING APPROACH

A structural application is proposed to link Chapters 3 (modeling) and 4 (experiments) focuses on using advanced industrial based Hyperspectral Near Infrared Imaging (NIR) method to model the waviness map of a manufactured panel. Then the numerical model and experiments are developed to predict the behavior of composites with un-uniform waviness defects under the bending load. It is proposed to use NIR hyperspectral imaging and progressive damage finite element analysis for advanced distributed damage characterization in composite structures. Our approach overcomes the obstacles facing accurate mechanical analysis of the structure as it is built without simplifying assumptions of defect levels. A finite element mesh generation technique with the capability of meshing layers separately has been developed to transform the resin thickness maps to a finite element mesh with a ply-by-ply representation including cohesive layer failure interfaces in between the plies. The proposed method is demonstrated on a continuous plain weave fabric carbon fiber/epoxy laminate.

### 6.1 Hyperspectral Imaging and Flexural testing

In the absence of reliable stochastic or multi-physics models that account for manufacturing, it is not possible at this point to accurately predict the locations where defects occur before manufacturing. Even if the wrinkle defect is visible, it is not currently possible to reliably determine its depth non-destructively using methods that are commonly used, such as ultrasonic inspection. In other cases, excess resin on the composite surface might result from a wrinkle in the bagging material, so there is no underlying composite feature. NDI methods based on ultrasound can detect resin pockets in excess of 1000 microns but cannot accurately measure pockets that are less than 1000 microns deep. Thermoelastic stress analysis methods have also been proposed to identify resin pockets and wrinkles, but these require a cyclic application of load [81]. Thus there exists the need for robust, portable and accurate methods for providing identification and depth measurement of wrinkles in composite structures.

Chemometric data processing methods can be used to characterize the relationship between the spectra and the resin thickness and provide the correlation to predict a point-by-point local resin thickness and thus produce thickness maps of the scanned resin surface. Recent advances in hyperspectral near infrared (NIR) sensing and data processing technologies have made real-time infrared methodologies a viable solution for accurate analysis of composite structures. NIR imaging can accurately measure surface resin on composite materials from 125 to 2500 microns thick, detecting virtually all resin pockets, resin-filled surface wrinkles and other surface resin features [82]. The resin-rich areas on the surface are usually an indicator that wrinkles are affecting some or all of the plies in a laminate stack. In the proposed method developed in this thesis, a push-broom near infrared (NIR) hyperspectral imaging approach is used to scan the composite structure and produce a map of the resin depth on the surface. This map is subsequently used to generate a

morphed finite element model corresponding to the non-uniform wrinkling in the structure. A progressive damage-based finite element method is used to predict the elastic and failure response at any desired location. The result is not only a defect map, but also a detailed structural health assessment of the distributed damage due to the non-uniform ply waviness in the structure. The steps involved in this method are comprised of the following:

1) In the push-broom NIR hyperspectral imaging approach, a line of pixels is measured and the sample is moved along a path that is perpendicular to the imaging line. The push-broom approach to imaging is capable of high spatial resolution to completely define the resin features by generating a 3D profile of the resin features on the surface of the composite structure (Figure 6.1).

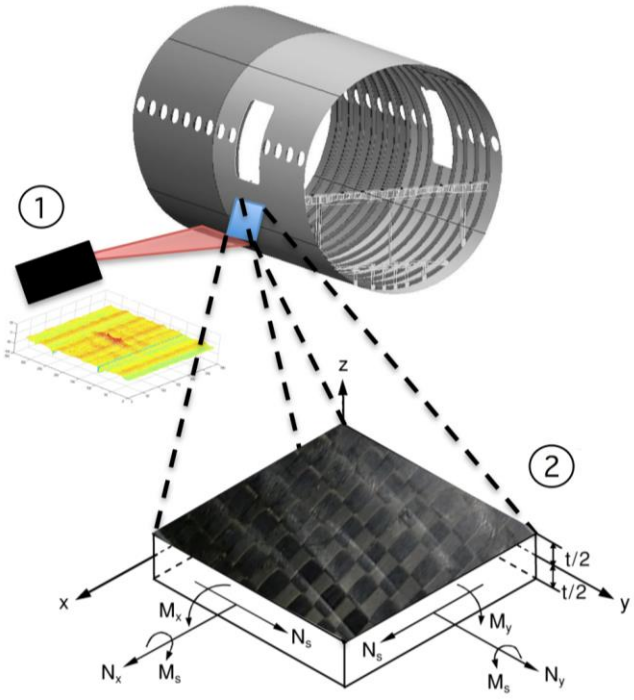


**Figure 6.1** Schematic of analysis framework (1) Composite part is scanned with hyperspectral NIR imaging for surface resin pockets and wrinkles (2) Progressive Damage Analysis is performed on sub-zone or entire structure if needed[151]

2) The 3D profile of the resin is subsequently used to modify the finite element mesh of the structure in question. Information from the resin profile is used to introduce wrinkles on the 3D surface resin map. The mesh-morphing program is capable of adjusting the thickness of the plies to the newly imposed constraints. Optical microscopy confirms the link between wrinkle depth and the resin thickness on the surface.
3) A progressive finite element method comprising continuum damage zone theory and cohesive layers is used to compute the structural stiffness and strength for the structure or sub-zone of the structure under the given loading combination.

One study has shown how waviness can be created with oversized plies that conform to a given geometry [137]. In this study, the oversized ply method is used to create the random wrinkle distribution in the specimen. The oversized composite prepreg layers were packed into an aluminum mold. A silicon sheet of 5 mm thickness is applied over the composite to assist with consolidation. The laminates were cured using a 'hot-press' approach where uniform heat and pressure are applied per the recommended 121 degrees Celsius (250 degrees Fahrenheit) cure cycle. The NIR data was collected using a hyperspectral imaging system (Via-Spec Stage (MRC-920-044) with a SWIR hyperspectral camera (MRC-303-005-01), Middleton Spectral Vision, Middleton, WI).

We targeted the pressure and temperature deviations and the resin migration as the most parameters acting in practice. We packed the stacked up layers in an aluminum mold under boundaries pressure by exceeding the layer dimensions over the mold dimensions. Figure 6.2 shows the layup which has been placed in the hot press. Silicon mold allows resin to migrate over the fabric producing resin pockets.

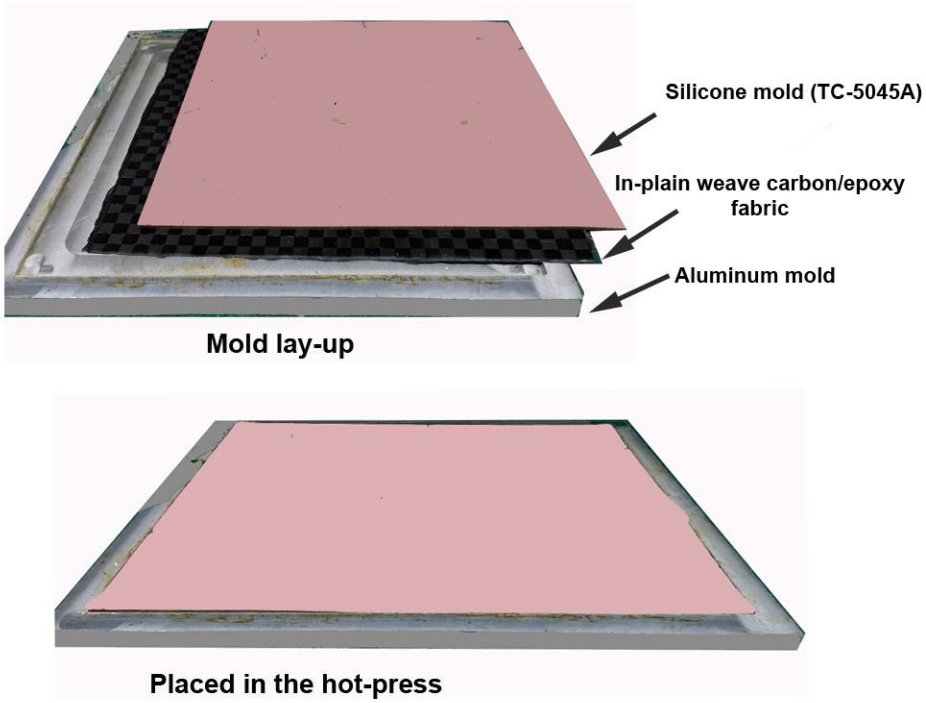


**Figure 6.2** The oversized layup placed in a mold

The curing process has been differed from the original manufacturer suggestion by increasing the temperature from 250ºF to 290ºF and decreasing the applying pressure from 3.5psi to 3psi. The specimens were trimmed from 304 × 304 mm (l2 ×12 in) panel cured using the process described. The width of the specimen is 12.7 mm (0.50 in) and the length is 68.6 mm (2.7). The specimens were trimmed from a 304 × 304 mm (l2 ×12 in) panel cured using the process described above. The width of the specimen is 12.7 mm (0.50 in) and the length is 68.6 mm (2.7 in). Figure 6.3 shows the panel after curing, with cross-sections from optical microscopy showing the random waviness profile spread over the specimen.

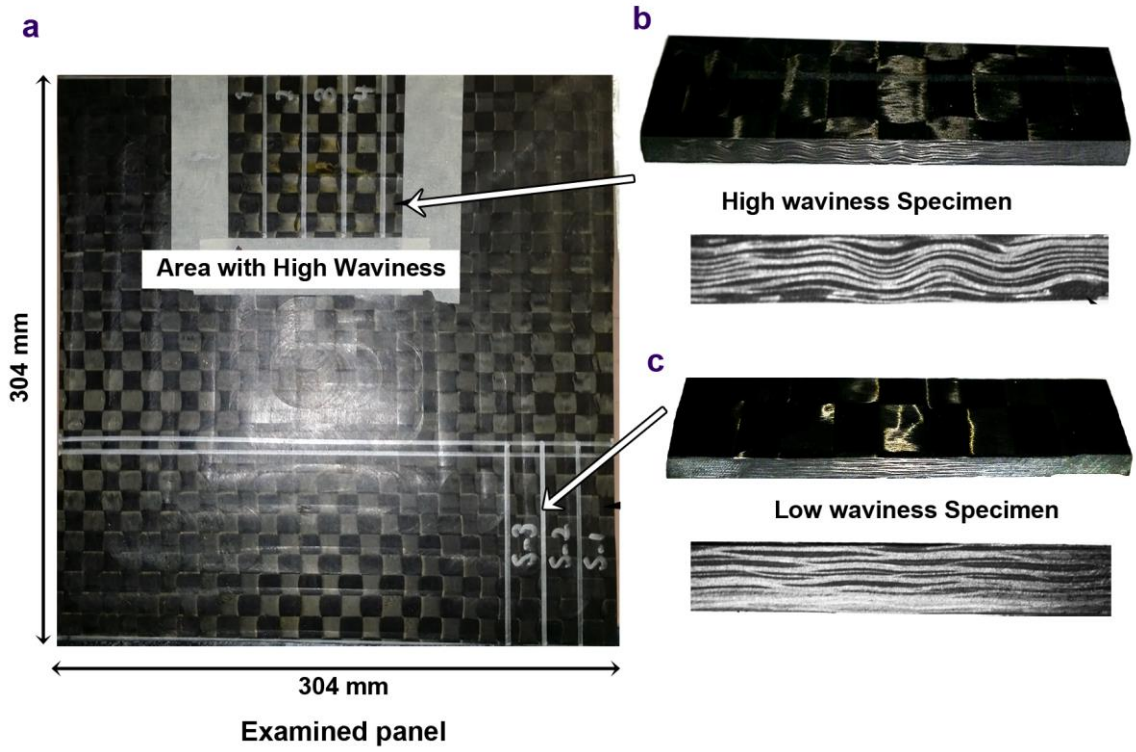


**Figure 6.3** Composite panel showing non-uniform ply waviness across different regions

The panel shows the successful creation of waviness zones that are randomly spread over the panel with different features with a particularly high waviness region as shown in Figure 6.3. The high amplitude waviness zone itself also contains wrinkles with non-uniform features such as amplitude, length and number of successive waves. This is typical of waviness formed in the manufacturing environment as observed by the authors. The specimens from different areas representing different defect levels are tested using 3 point-flexure (Figure 6.4) according to ASTM D7264 [152]. The extracted specimens were examined by optical microscopy and key features of the cross-section are shown in Table 6.1.

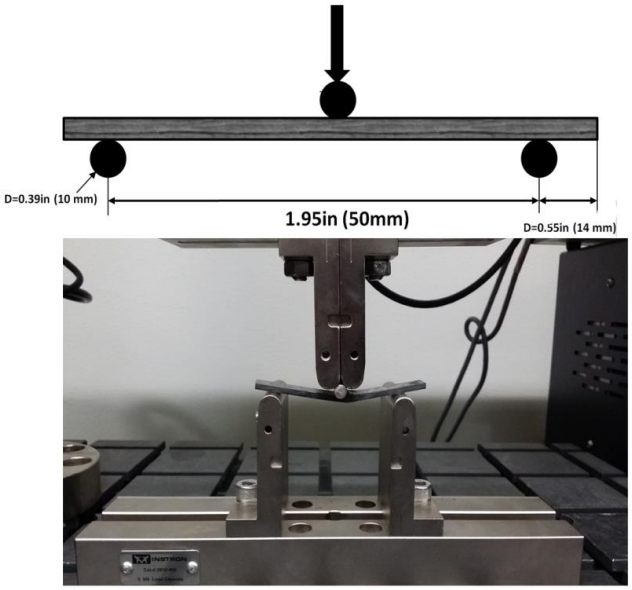


**Figure 6.4** 3-point bending test according to ASTM D7264

**Table 6.1** Wrinkle geometry of test specimens using optical microscopy

| **Specimen ID[1]** | **Number of wrinkles (Right)** | **Number of Wrinkles (Left)** | **Maximum Amplitude (Right), mm** | **Maximum Amplitude (Left), mm** |
|---|---|---|---|---|
| Specimen 1 | 3 | 5 | 0.078 | 0.333 |
| Specimen 2 | 6 | 3 | 0.382 | 0.184 |
| Specimen 3 | 2 | 3 | 0.290 | 0.117 |
| Specimen 4 | ~ | ~ | 0.020 | 0.031 |
| Specimen 5 | ~ | ~ | 0.019 | 0.021 |

[1]The flexure specimens are examined on the long ends.

The amplitude of waviness in specimens 4 and 5 are considered the baseline for the woven material and are from properly consolidated regions with no resin pooling. Prior to sectioning the specimens, Step 1 of the procedure was implemented, in which the intact specimens were scanned using the near infrared hyperspectral imaging method.

## 6.2 Hyperspectral imaging test

Near Infrared hyperspectral imaging is used to study the surface wrinkle distribution in the fabricated composite panel. In the near-infrared wavelength region the overtones and combination bands of the fundamental molecular vibrations are measured. The chemical specificity of such molecular vibrations allows the identification and quantification of materials and material mixtures [153, 154]. The specific absorption of the overtones and combination range is lower than that of the fundamental vibrations, thus materials, such as the excess resin on carbon composite parts can be investigated *in situ* without the need for dilution. The hyperspectral imaging method is similar to the conventional reflectance spectroscopy with a source illuminating the surface at an appropriate angle and optics detecting the reflected light within a particular wavelength range. With push-broom hyperspectral imaging, a camera integrated with a spectrograph is used to collect spectra at all locations on the sample one line at a time. Near-infrared light in the 1000-1700 nm range penetrates the resin and is scattered back from the carbon filaments so that light passes through the resin twice. The double transmission spectra detect the chemical signature of the resin, and the amplitudes of the spectral features are proportional to the resin depth at that point. The resin thickness is then calculated from the near infrared spectrum measured at each spatial point.

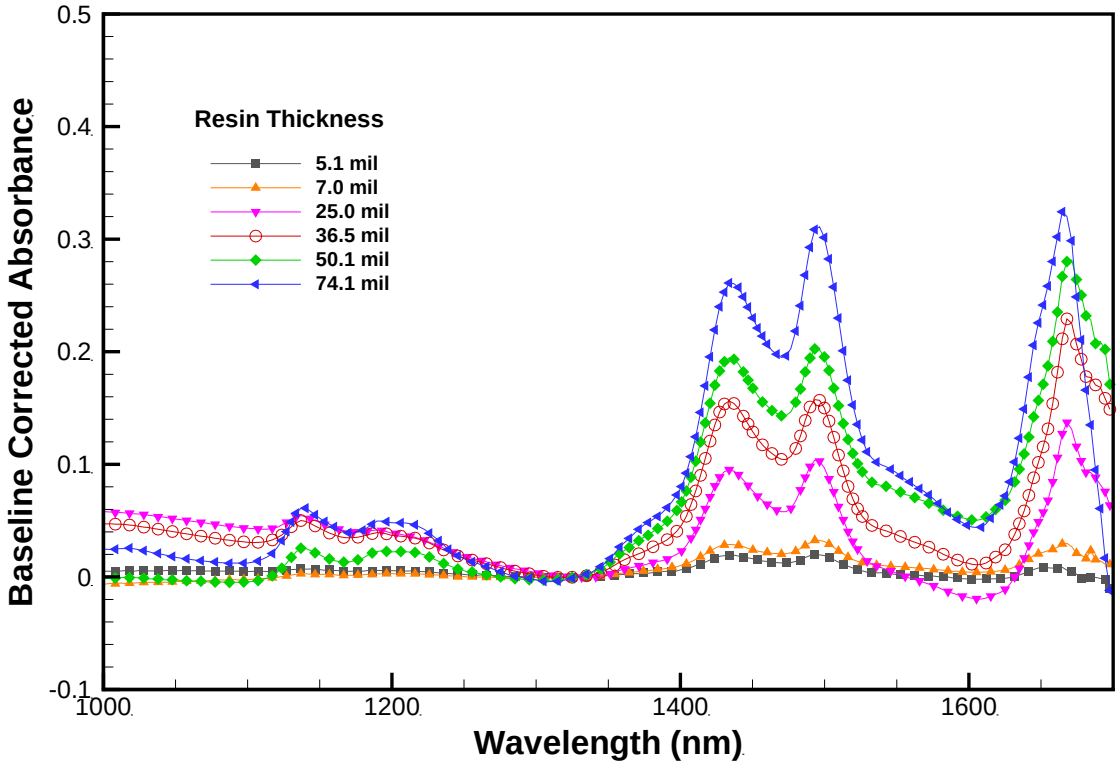


**Figure 6.5** a) Baseline corrected near infrared spectra (1000 to 1700 nanometer range) for a range of epoxy resin thicknesses. A calibration is created to correlate the measured absorbance with resin thickness at each scanning point[151]

Figure 6.5 shows the reflectance spectra obtained on resin standards with different thicknesses that were made on test coupons to mimic the composite structure with resin on its surface. The method is accurate to approximately ±150-micron resin depth.

The short wave infrared (SWIR) hyperspectral camera with full near-infrared wavelength range (1000-2500 nm) was used to scan the fabricated composite panels (Figure 6.6).

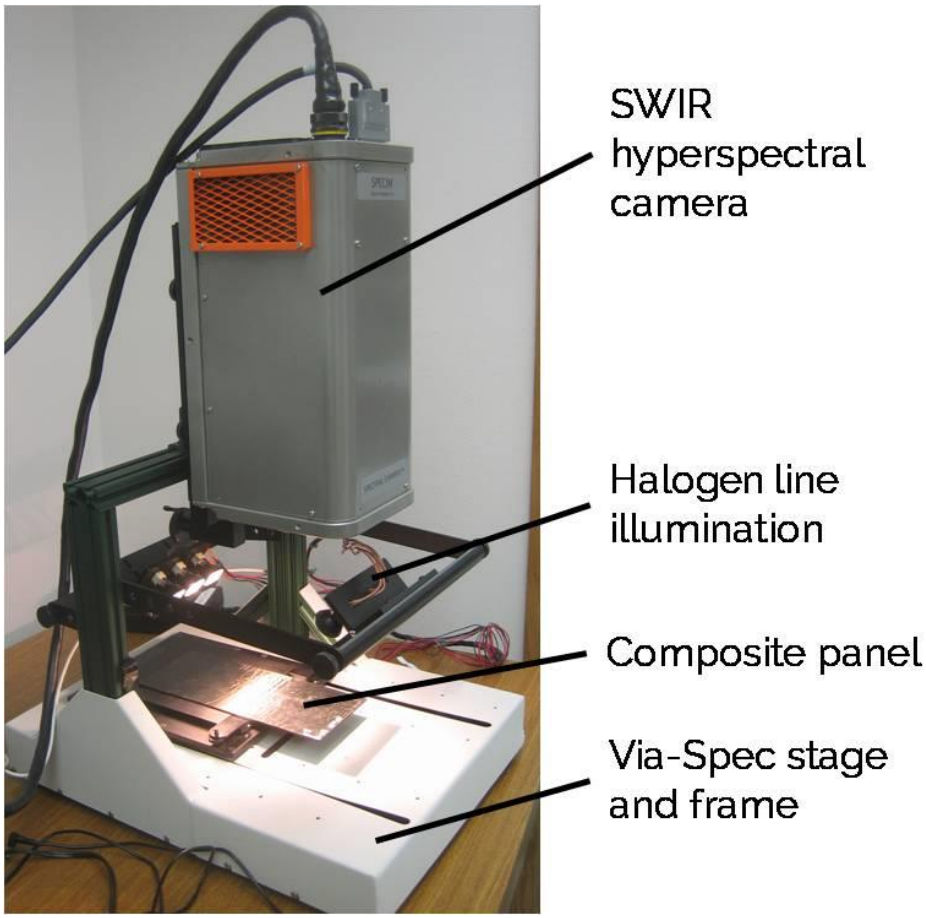


**Figure 6.6** Test setup for near infrared hyperspectral imaging of composite panel with spatially distributed non-uniform waviness[151]

The short wave infrared (SWIR) hyperspectral camera with full near-infrared wavelength range (1000-1700 nm) was used to scan the fabricated composite panels. For the hyperspectral analysis in this thesis, that region was used because the thicker resin causes optical saturation in the longer wavelength region. Figure 6.1 shows the detected and measured resin pockets on the composite panel, focusing on the region containing the waviness. Three distinct regions were selected from within the panel. In one region, there was a large amount of waviness with non-uniform wrinkle size and a random distribution. Three specimens with different levels of waviness

have been cut from the waviness region of the panel and two specimens were cut from a region away from the high waviness zone. In the specimens extracted from the region with high waviness, significant spatial variability and non-uniformity of the wrinkling was observed. The waviness is non-uniform even within the same specimen.

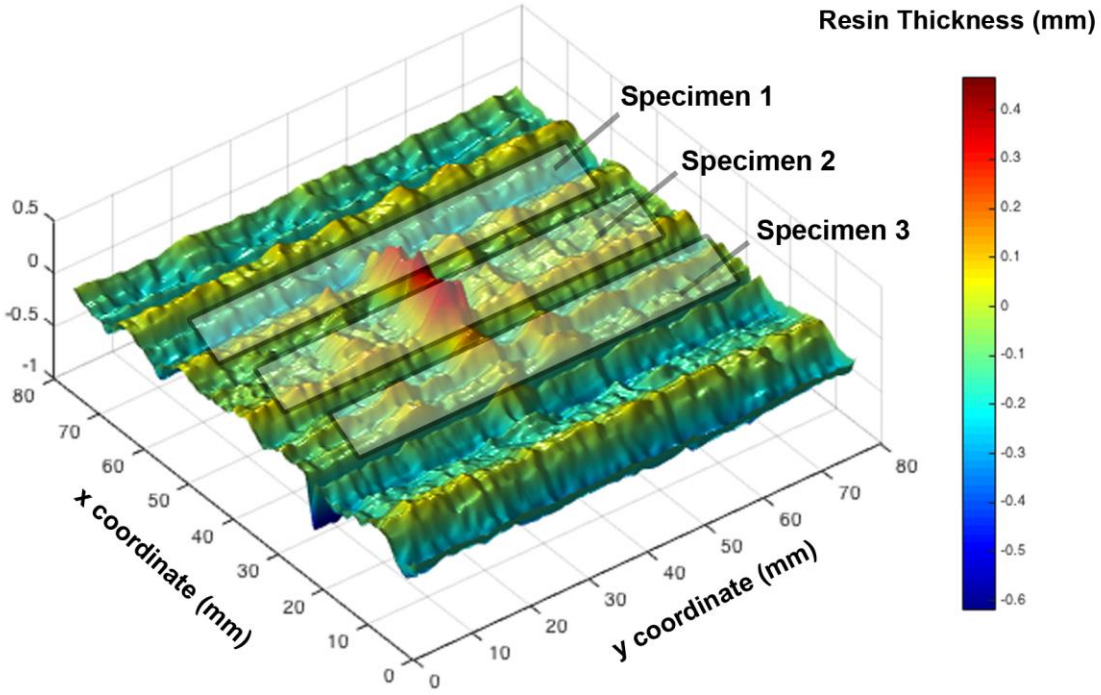


**Figure 6.7** The 3D surface map of resin pocket depth as measured by the near infrared hyperspectral imaging method[151]

For example, Specimen 1 has a high-amplitude wrinkle on one side, which then degrades to a low-amplitude wrinkle on the other side. Similar variations are seen in other specimens to various degrees. The proposed model is capable of providing strength and stiffness estimation regardless of the variability as the actual resin geometry with incorporated into the model.

## 6.3 Progressive Damage Modeling

The proposed modeling approach uses the high sensitivity of the hyperspectral NIR method with its capability to detect superficial resin pockets as small as 30 microns. These resin-filled surface pockets are directly correlated to regions where the fibers are wrinkled through the thickness of the composite laminate. At the first step of the modeling process, The STL file format is used to create a surface of the random waviness from hyperspectral imaging (Figure 6.8).

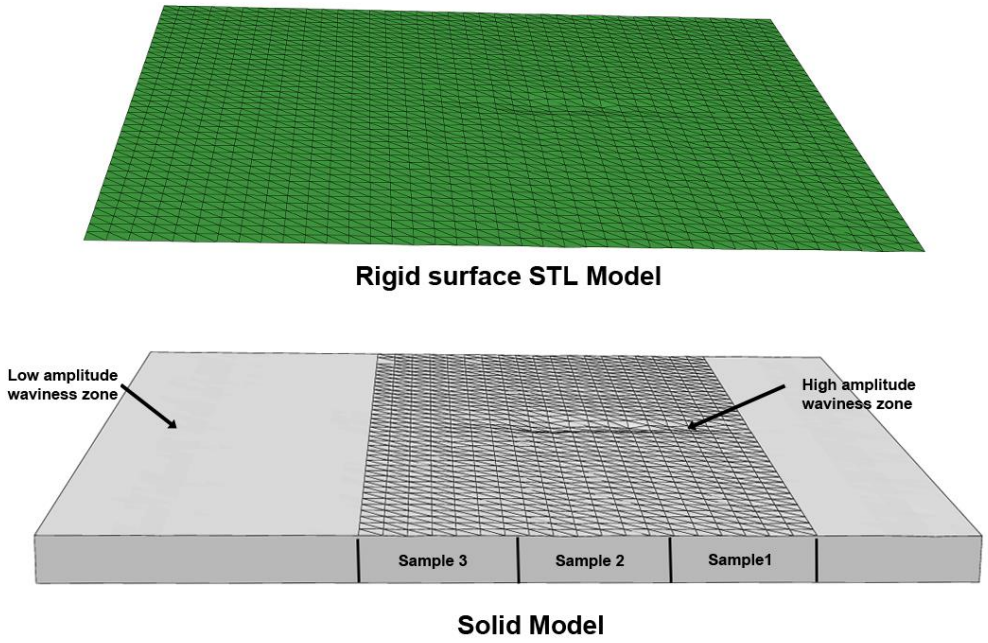


**Figure 6.8** a) The standard tessellation file created by Mathcad and b) the solid file created by CAD software

This is confirmed by cross-section examination of specimens. In the progressive modeling process, the ply-by-ply finite element (FE) models are morphed into the actual geometry using the 3D surface resin thickness maps from the NIR hyperspectral images (Figure 6.9).

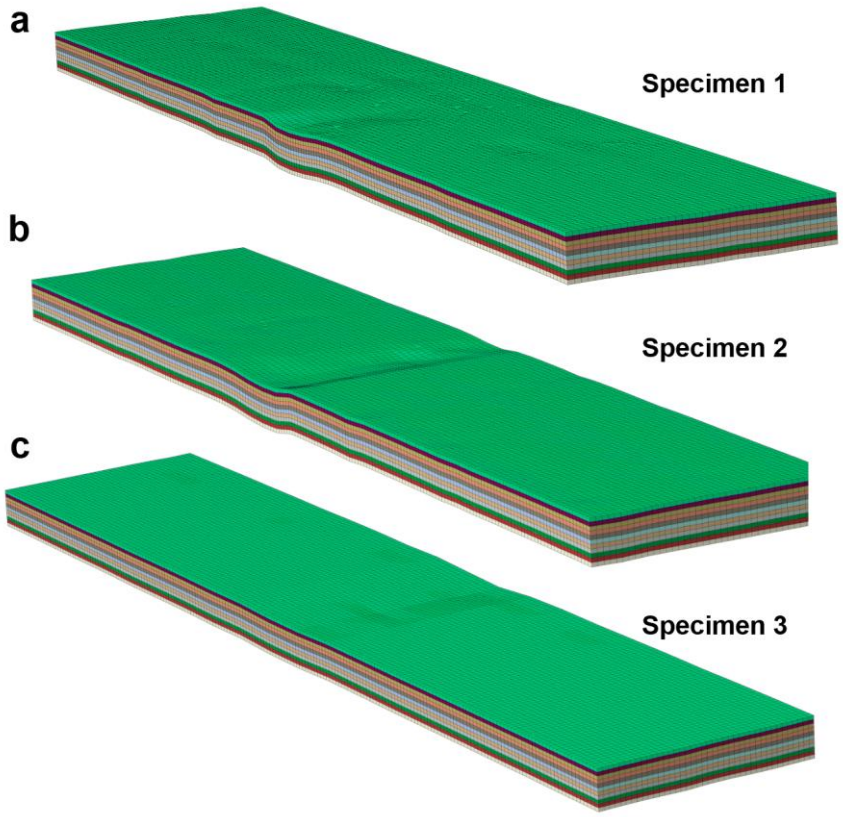


**Figure 6.9** Finite element meshes of specimens representing non-uniform spatially distributed wrinkling (a) Specimen 1 containing distributed regions of waviness (b) Specimen 2 containing severe non-uniform waviness (c) Specimen 3 with low amounts of waviness[151]

The mesh morphing process uses the 3D surface obtained from the NIR method to reconfigure the pristine mesh into a new mesh capturing the random and non-uniform waviness

profiles. These structural morphing process steps were accomplished using a software program developed by the authors. In the morphed model, the damage mechanisms for the plain weave composite laminates are included (i.e. matrix cracking, fiber-matrix debonding, fiber fracture and interlaminar delamination). Due to the high transverse shear, translaminar failures may dominate the behavior of the flexure specimens. In order to investigate the relevant failure modes in this problem, the 3D Hashin-Puck's criteria [155, 156] was employed with cohesive zone modeling for the interlayers. The numerical analysis has been incorporated as a two-step, multi-scale progressive damage analysis based on the 3D Hashin/CZM criteria (Sec. 3.2.3) to study the damage behaviors of 2D plain weave composites under various uniaxial and biaxial loadings [157, 158]. In the model, a direct method is used to model the interlaminar shear stress using solid brick elements. For the delamination failure modes, a cohesive surface interaction has been applied between layers from the top layer through the thickness. The interface in the cohesive zone model is modeled as a constitutive behavior specified by a traction-separation relationship. The derivation and finite element implementation of the cohesive damage model are described in [116, 159]. Eight-node linear reduced integration brick with the reduced integration feature and hourglass control advantage (C3D8R) were used in separate layers. This feature provides a basis for accurate estimation of transverse shear stresses in a composite section where delaminations are possible.

### 6.4 Results of hybrid analysis

A reasonable correlation is observed in the elastic and failure load between experiments and the progressive damage model of non-uniform waviness produced using the hyperspectral NIR method. The maximum load capacity of the specimens drops from 42% to 17% depending on the waviness profile and the location from which the specimen is extracted (Figure 6.10).

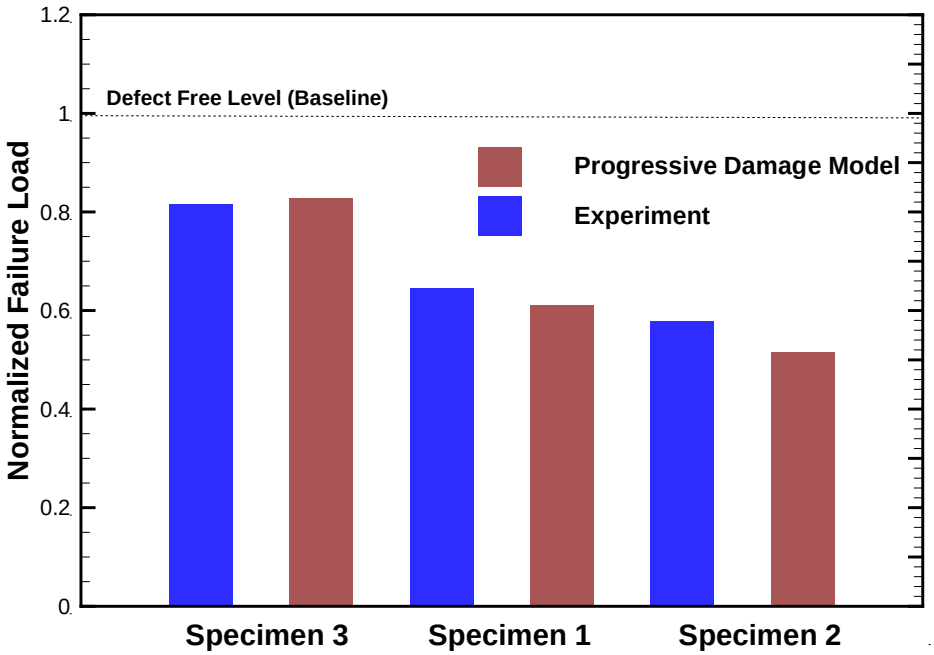


**Figure 6.10** Failure loads for specimens extracted from different regions in panel with spatially distributed non-uniform wrinkles[151]

A remarkable correlation is observed between the model prediction and the failure loads of the extracted specimens. Specimens 1 to 3, which were extracted from a region having high waviness, have lower failure loads than Specimens 4 and 5, which were taken from regions having negligible waviness (Figure 6.10). For the specimens from the high waviness zone, note the link between the maximum force values and the specimen geometry related to the location shown in Figure 6.8.

The series of experiments and simulations performed using this methodology also shed some light on damage mode transitions in the specimens related to the waviness profile and location. The progressive damage model failure modes observed show similar observations to the experimental results. The results are also consistent with previous studies in this area, the finite

element method has been previously used to study the effects of wrinkles on composite properties [160]. Wisnom et al. [67] used a non-linear finite element analysis showing the same mechanism of shear instability due to fiber waviness occurring under pure bending as under pure compressive loading.

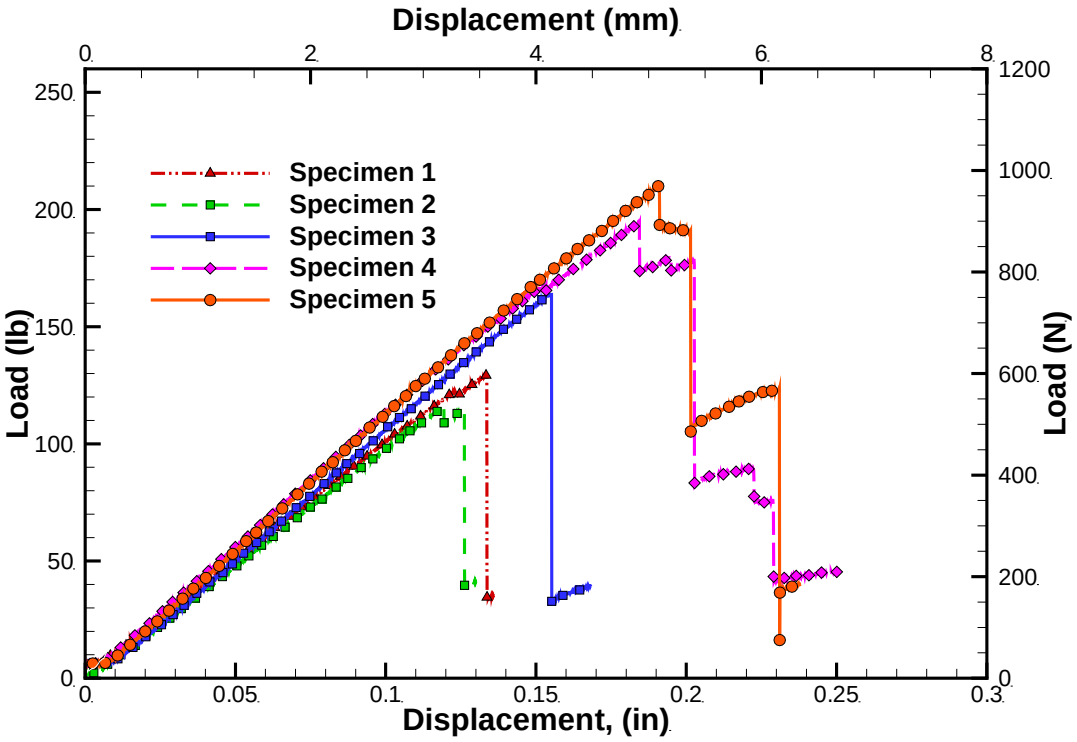


**Figure 6.11** Force versus displacement curves under 3-point flexural loading[151]

They showed that the maximum stress in bending was up to 73% higher than in compression. The results show that where failure is controlled by shear instability due to fiber waviness, compressive strength can be expected to be a function of stress gradient and therefore cannot be regarded as a true material property.

The hyperspectral imaging enhanced progressive damage models and the experiments show that delamination occurs at the highest fiber misalignment angle near the ply waviness apex. Delaminations appear as a result of kink band formation and interlaminar shear damage growing over the layers. Optical microscopy of the specimen edges during the flexural test shows two distinct failure mechanisms associated with varying regions of delamination.

In the specimen with the repeated high amplitude waviness profiles, the most dominating failure is delamination growth and propagation between the layers, particularly where the resin pocket is deepest. Large amounts of delamination occur before final failure occurs in the tension zone of the specimen. The fiber kink band formation is confined to small zones. The onset of delamination is observed in both cases to occur at the point of highest fiber misalignment. The optical micrographs of Specimen 2 as it progresses to failure are shown in Figure 6.12a.

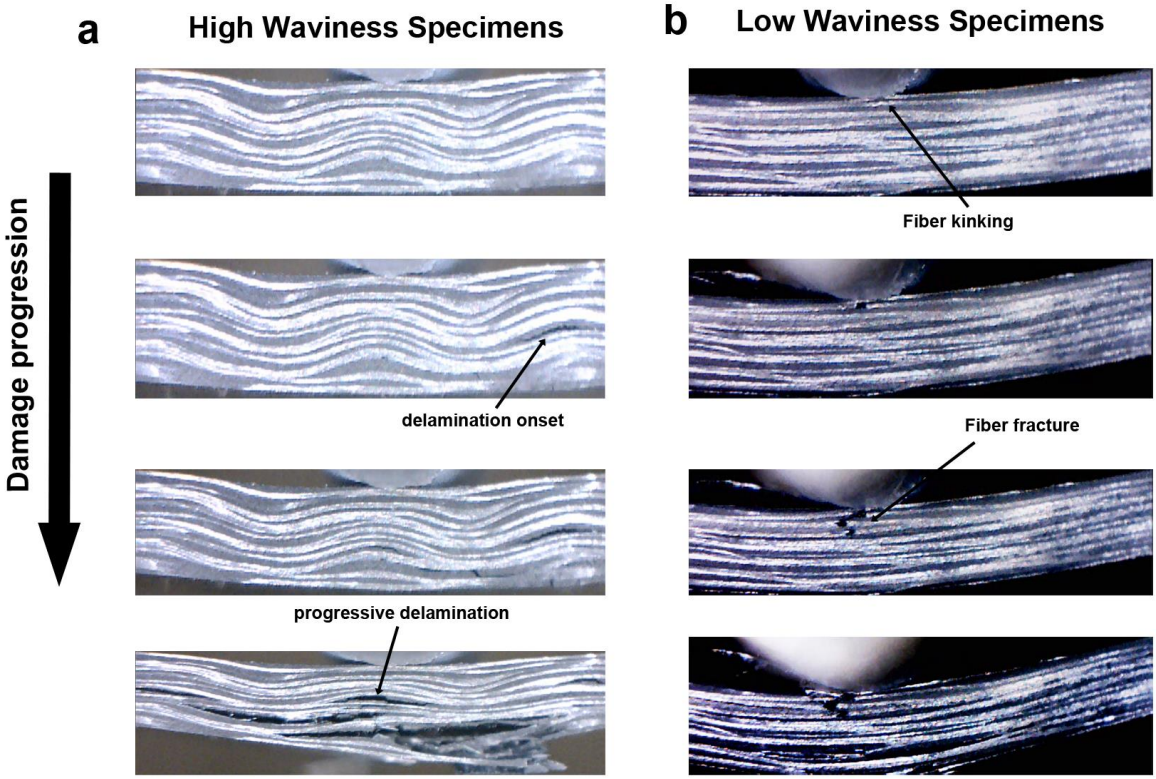


**Figure 6.12** Failure progressions using optical microscopy of a) the high waviness amplitude specimen number 2 and b) low waviness amplitude specimen number 3[151]

For both experimental and numerical analysis, delamination occurs at the highest fiber misalignment angles nearby the waviness apex. Delaminations appear as a result of kinking formation and interlaminar shear damage growing in-between layers as shown in Figure 6.12 a.

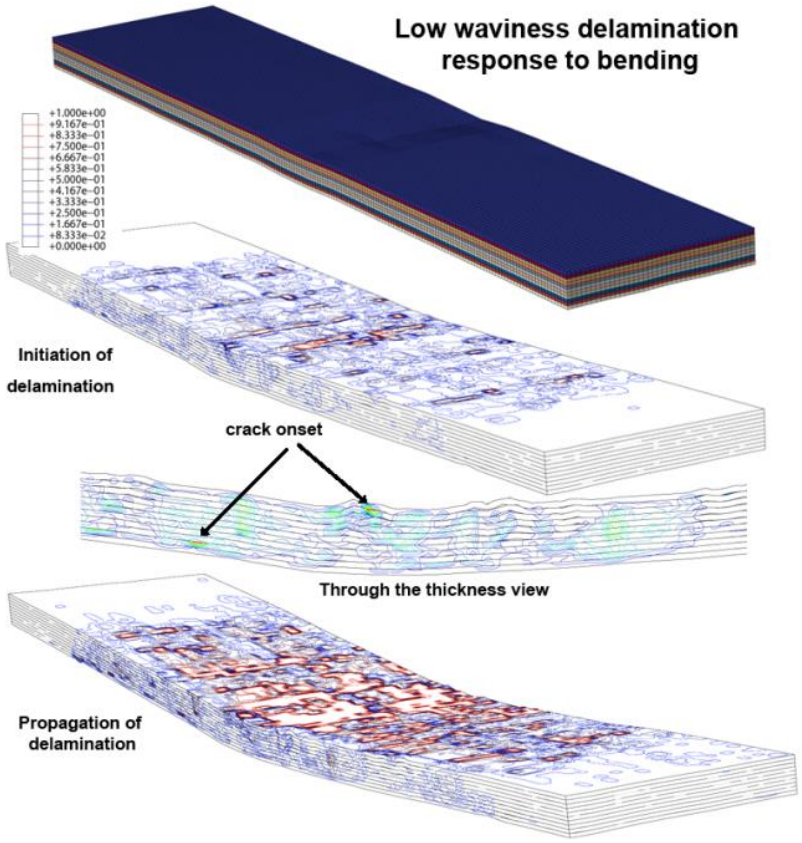


**Figure 6.13** Numerical demonstration of the kinking of fibers under compression for the low waviness specimen (Specimen 3)

For the specimens with high amplitude waviness, the most dominated failure is delamination initiating and propagating between layers where the resin pocket is deeper. The fiber kinking is narrowly appeared in microscopic view of the experiments (Figure 6.12 b) and the numerical analysis (Figure 6.13). It is obvious that the delamination onset is originated in higher fiber misalignment points.

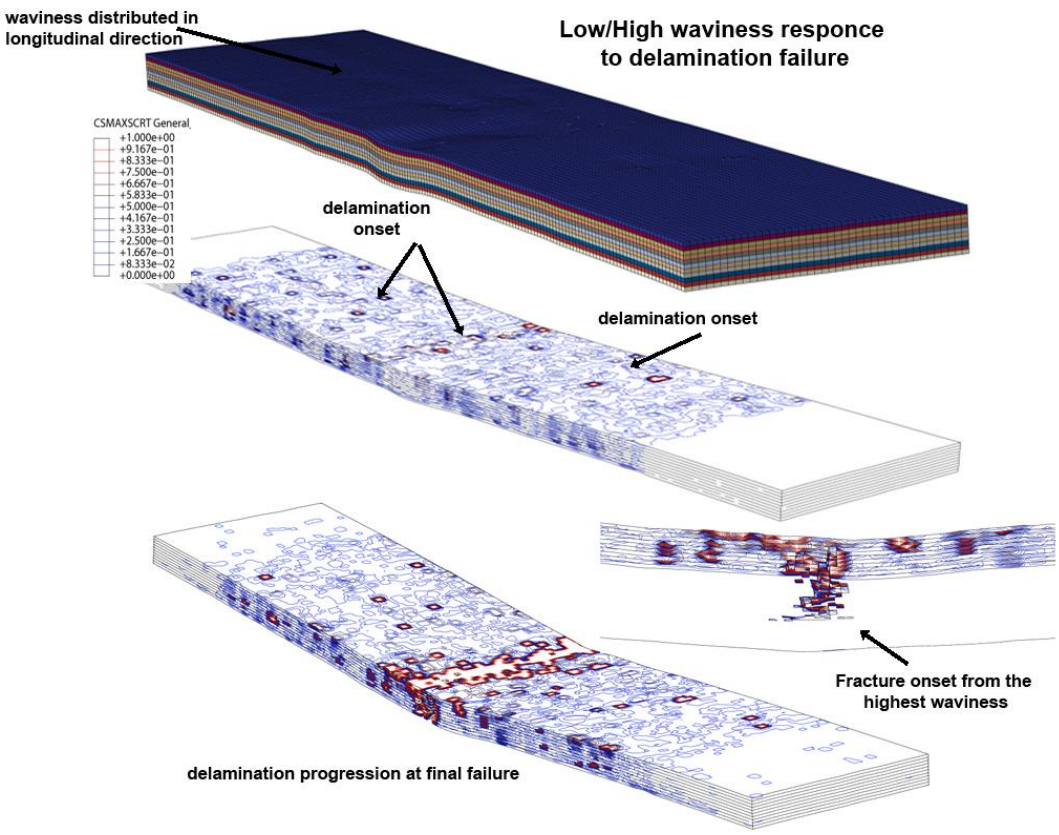


**Figure 6.14** Delamination failure mode for the specimens with high/low waviness amplitude (Specimen 1)

The final failure is shown in Figure 6.14 for high waviness and low waviness specimens. The domination of the delamination failure in the specimens with higher amplitude can be seen at the fiber kinking leading to delamination at the resin pocket zone and fiber fracture. Consequently the fiber fracture starts from the highest waviness toward the low waviness side as shown in Figure 6.15.

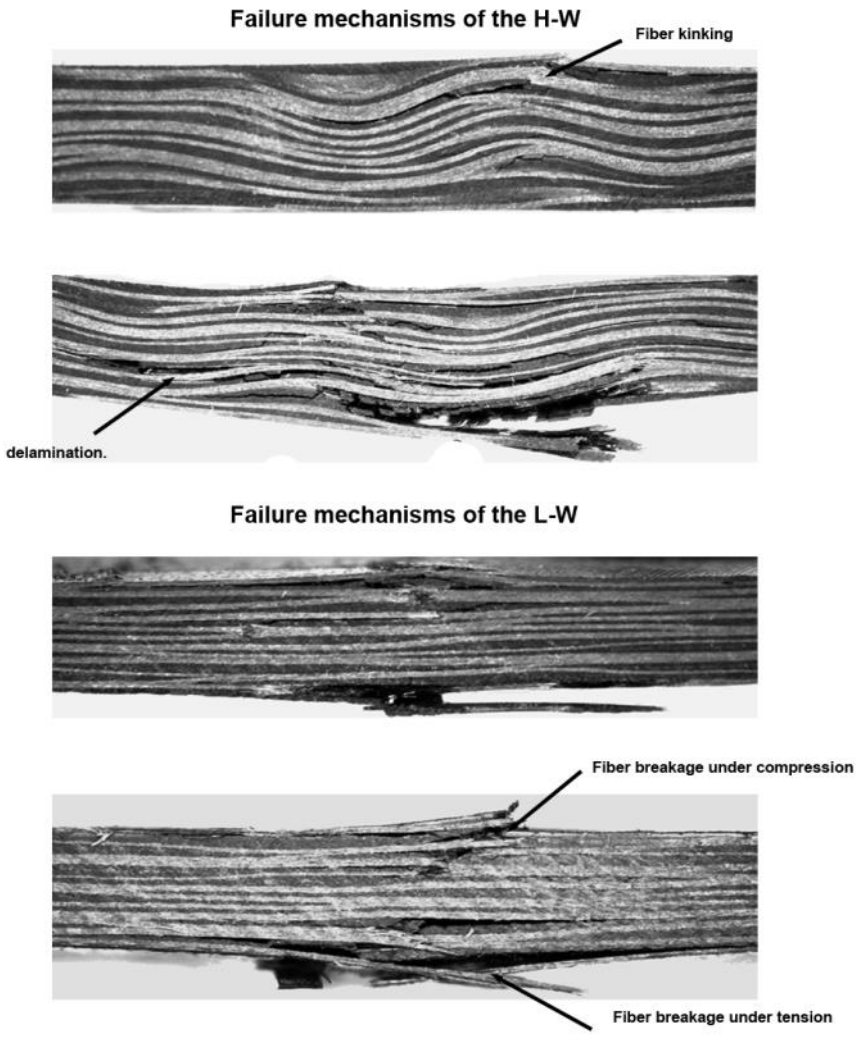


**Figure 6.15** Final failures show the fiber failures are emerged in the fiber kinking and delamination for both high and low waviness specimens

The domination of the delamination failure in the specimens with the higher amplitude can be understood with the fiber wrinkling leading to delamination at the resin pocket zone and finally to the fiber fractures. Consequently, the spatial propagation of failure in these specimens starts from the highest waviness side and progresses across the width into the low waviness zone on the other edge. This is trackable in numerical analysis assisting to trace the failure all over the

specimens and in between layers. Figure 6.16 shows the interlaminar failure progression in specimen 2 where damage index implying delamination.

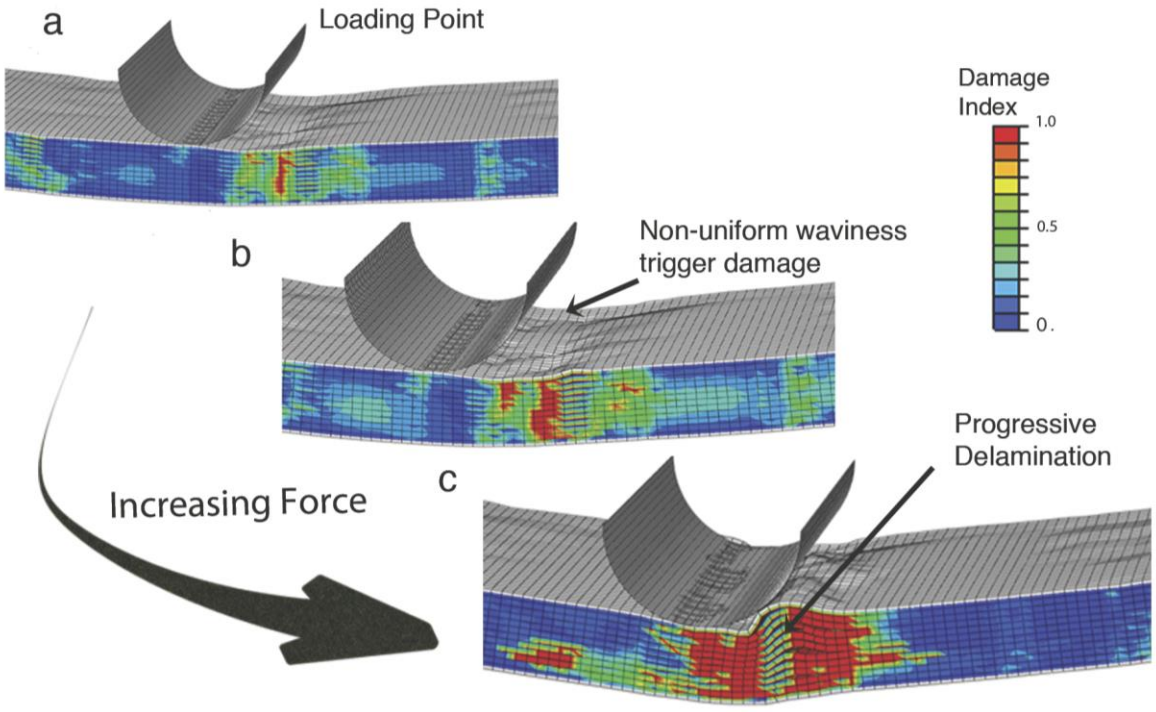


**Figure 6.16** Model results from Specimen 2 showing progressive growth of delamination under increasing force. In (a), the damage index represents regions where delamination has begun to occur. In b) and c) delamination grows from the initiation site occurring away from highest bending moment location under the load and affecting multiple plies[151]

It is shown in Figure 6.16 (a) and (b) the delamination failure is initiated and propagated at the location of highest waviness earlier than under the applied load. The micro delamination of the upper layers of the low waviness specimen (Specimen 2) shows how the failure in the low waviness

specimens is initiated by kink band formation and then the specimen breaks in a sublaminate zone (Figure 6.16b). In Specimen 2, the top plies that are under compression show a narrow band of kinking where the matrix shear is dominant. The cracks grow at the fiber/matrix interface in the sublaminate region until the bottom fibers in the region experience a localized fracture in bending. Thus, in this specimen, the few wavy layers on the surface dominate the entire failure response of the specimen.

This is noteworthy that for the lower waviness specimen (specimen 3), the interlaminar damage spreads out through layers. This observation contradicts with the failure mechanisms of specimens 2 and 3 -possessing higher waviness- where the delamination is localized in waviness zones. This failure behavior is occurred since the laminate beam can take higher stresses under the absence of high waviness defects and the transverse shear stresses can reach critical values in between layers resulting dispersed interlaminar damages. However localized high transverse shear stress concentration points at high waviness specimen will be led to consequent fiber fracture at lower load level than specimen 4 and 5. The change at the displacement response is derived by the out of plane stresses at waviness areas which is randomly distributed over the specimens.

The transvers shear stress also has been examined through the thickness for the high and low waviness specimens (specimens# 2 & 3). Figure 6.17 shows the shear stress through the thickness at the load and at the point of highest fiber misalignment angle.

The transverse shear stresses at the point under the load and at the point of high misalignment angle have been investigated in numerical analysis results. By investigation, the shear stress at the point of high misalignment angle for the high amplitude waviness specimen (specimen #2) changes from 4.27 ksi (29.5 Mpa) to -2.7 ksi (18.6 Mpa) and for the low waviness specimen has been limited between 0.96 ksi (66.2 Mpa) and -2.2 ksi (15.2 Mpa) shown in Fig.

6.15. By investigating the transverse shear stress under the applying load, the extremum values have not been significantly changed. This comparisons confirms the importance of the waviness to cause premature failures and progressive damage.

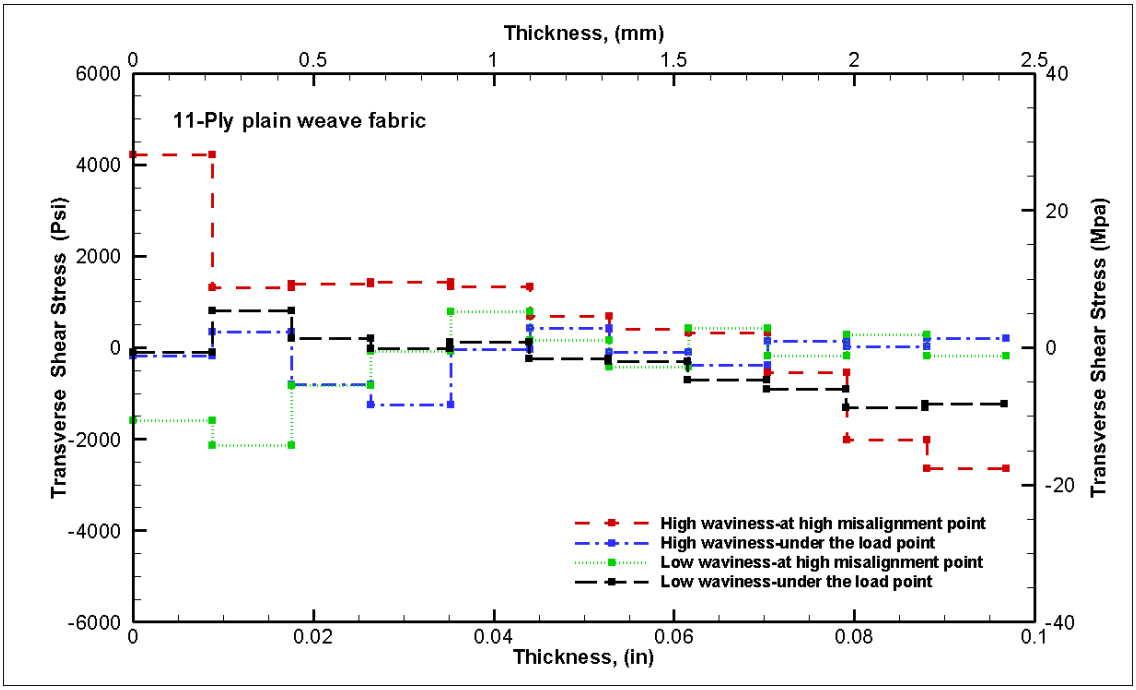


**Figure 6.17** The out of plane shear stress (S13) variations through the thickness of the high and low waviness specimens (specimens # 2 & 3)

Since the waviness is not even through the thickness of the specimens, the results of the numerical analysis are used to determine the exact location of the failure initiation. The distributions of the transverse shear stress through the thickness of the specimen #1 which contains low waviness at one side and high waviness at the other side have been shown in Figure 6.18 and 6.19. The specimen #1 has been chosen to investigate since the points with different waviness at

the same line along the width of the sample are accessible. Therefore, the points of high and low waviness are in the same distance from the applied load. All of the points are located in free edges supposing to pose magnifies transvers shear stress. Curves in Figure 6.18 clearly show higher $S_{13}$ shear stress level for the point with the higher waviness.

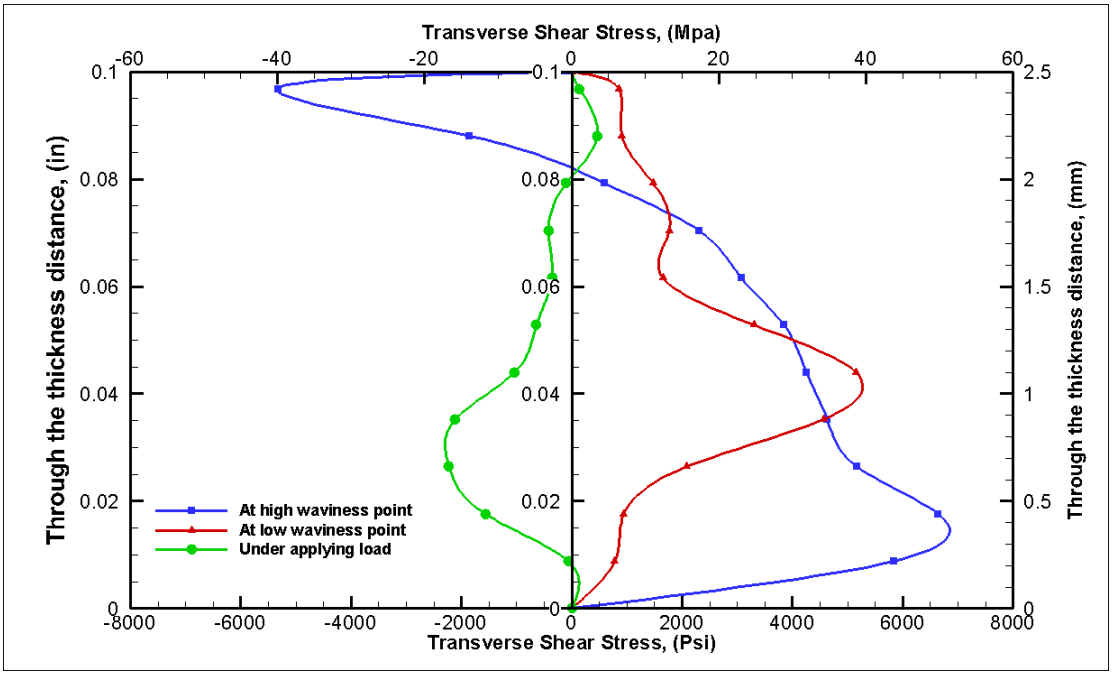


**Figure 6.18** Transverse shear stress (S13) in the specimen with high/low waviness (specimen #1)

The points of waviness are exposed to high shear stresses relative to the point under the load which possesses very low waviness.

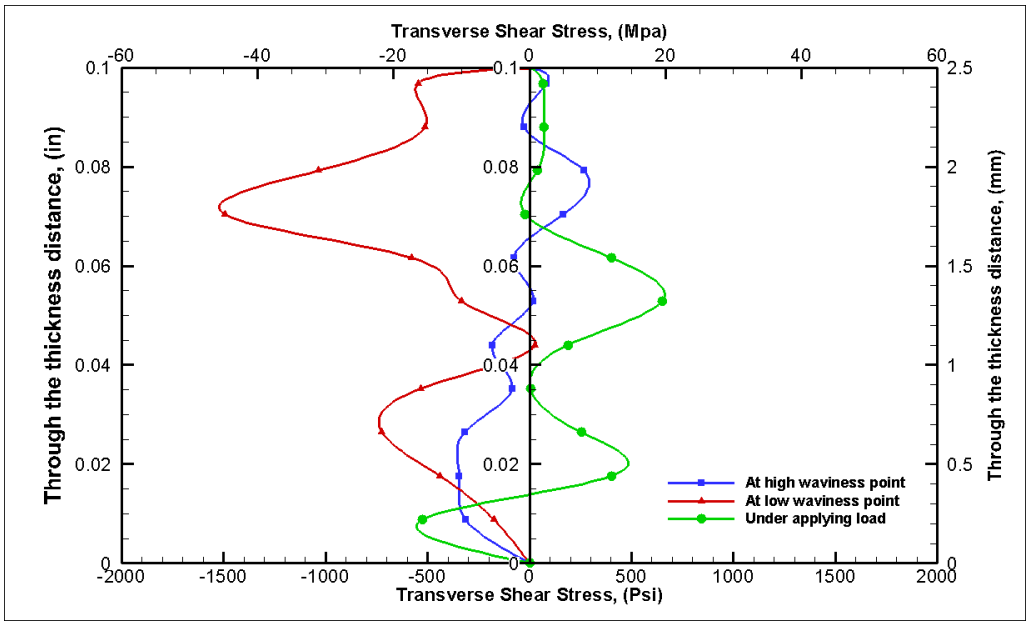


**Figure 6.19** Transverse shear stress ($S_{23}$) in the specimen with high/low waviness (specimen #1)

The transverse shear stress $S_{23}$ is a third of $S_{13}$ and larger at low waviness point. The largest value of the $S_{23}$ can be originated in transforming waviness through the width of the sample from high to low amplitude. It is worth mentioning that the waviness curve midpoint where the fiber misalignment angle have its highest values can be achieved in warp ($0^o$) and fill ($90^o$) directions for the in plain weave fabrics. This misalignment peaks can be advanced the transverse shear stresses in warp and fill directions deriving delamination to be propagated between layers over the width of the specimens.

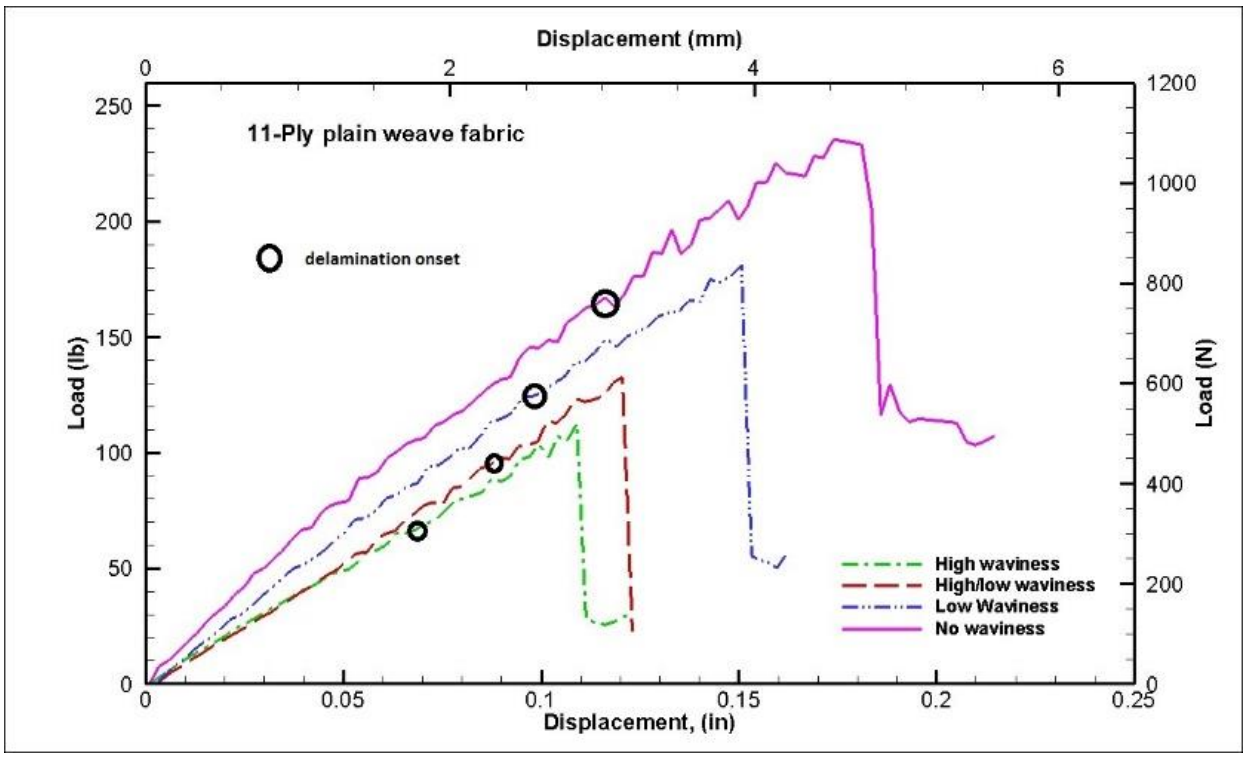


**Figure 6.20** Load-displacement curves of FE models with different waviness levels

The load deflection curves of the numerical models have been performed with the proposed numerical approach (Fig. 6.20). The peak loads and load-displacement curve slopes are reduced by increasing the waviness amplitude implying strength and stiffness degradations resulting from delamination failure vulnerability. The numerical model advantages capable to determine the delamination onset by tracking the cohesive contact failure at any load levels across inter plies.

# CHAPTER 7
# Conclusions

In the following chapter, the significant results of this dissertation is summarized. The conclusion is classified under the main engineering improvements in investigating the effects of waviness defects in composite laminates including analytical, numerical and experimental approaches. This dissertation have opened future studies up to researchers which some of them are addressed in this chapter.

### 7. 1 Analytical closed form approach

Analytical approach is discovered to include the effects of stress concentrations at the notch zone and the fiber misalignment angle at the waviness zone predicting the failure under standard Un-notched compression/tension and OHC tests. An analytical model based on synthesizing orthotropic stress concentration factor and a generalized expression using traction continuity through the kink band is developed for the strength predicting of the OHC tests. In development of the fiber waviness and kink-zone failures models, first an orthotropic laminate uniaxial loaded along the principal axis having the maximum stress occurs at the notch boundary is considered. A compressive failure model which includes the inclined kink band and induces transverse stresses at the initiation of kinking based on Budiansky and Flek kinking model is used. This combined model considers a combined stress plasticity law using a quadratic yield condition in the case of elastic-plastic strain hardening behavior assuming Ramberg–Osgood law. The analytical approach used shows a reasonable correlation with the experimental measurements. It is good to mention that the analytical model has been derived for kinking within a band of finite width and infinite extent for fibers with high amplitude waviness and a notch border beyond the waviness zone. The analytical model for predicting the failure strength shows good correlation with experiments and is capable of capturing both the waviness and notch size effects.

### 7.2 Numerical (FE) analysis approach

A numerical approach based on a combined continuum damage analysis and cohesive zone interlaminar behavior is used to simulate the failure initiation and propagation responses. The proposed FE modeling approach will attempt to predict the response of laminate structure with different levels of waviness. Specimens having controlled waviness definition and also random

and non-uniform wrinkling profiles were fabricated and modeled using the progressive damage model with ply-by-ply layer definition. The combined Hashin/Puck's with CZM model which used in this thesis can predict the load carrying capacity of the wrinkled specimens comparable with experimental results. The numerical FE model provides a vision by following the stress flow over ply levels of the laminate. The ultimate stress distributions at reaching of defined failure criterion can be illustrated the distinctive failure mechanisms and their interactions. The numerical results using the proposed method confirm the ability to predict strength reductions observed in the test specimens. They also provide important information about the failure progression and different failure modes. The proposed method is more informative than other approaches because of its capability to visibly and quantitatively follow all possible failure mechanisms including matrix cracking, delamination and fiber fracture. The continuum-based damage model with cohesive zone layers has demonstrated good agreement with the experimental results, but the proposed methodology does not preclude using other damage models.

### 7.3 Experimental Observations

Experiments have been designed to characterize the waviness geometries and to handle data acquisitions during tests. With the face-stabilized OHC fixture, the influence of the onset of kink zone formation on final failure features has been investigated. Using carefully controlled steel bars of different diameters to induce the desired waviness levels artificially creates the waviness levels required. Synchronized AE and microscopic techniques have been known to be useful in tracking the failure modes. As a significant result of the designed setup test, the damage evolutions of face stabilized defected specimens including kink band formation, crack onsets, delamination and fiber fractures are demonstrated to be characterized. The experimental evidence demonstrates

the influence of the waviness defects on the formation of the fiber kink band leading to the fiber fracture and the kinking band broadening.

An image correlation method is proposed to determine the start of incipient interlaminar delamination in continuous fiber reinforced composite materials. This new methodology is used to determine the limit point based on the z-displacement or out-of-plane displacement tracking. The limit point of the composite material represents the point after which permanent damage or inelastic behavior is expected to occur.

The results show how the tension load can trigger internal delaminations and out-of-plane deformations around common fiber defects found in carbon-epoxy laminates. It is discovered that the z-displacement increment on the surface of the specimen (at the constructed evaluation line) one is able to detect the instant these instabilities occur as confirmed by microscopic examination. The limit point is obtained by considering the first peak in the response. The results show that using the proposed 3D-DIC method together with a standard tension test setup, the limit point in the composite material can be exactly identified and thus providing useful material information that was previously not available using the standard test methods.

Hyperspectral near infrared spectroscopy is used to create a 3D profile of the surface resin pockets with the capability of measuring resin thickness from approximately 125 to 2500 lm. These resin pockets are directly correlated to underlying ply level wrinkling as confirmed by optical microscopy. The 3D mapped resin plane obtained from the hyperspectral imaging is used to morph a ply-by-ply finite element model of a carbon-fiber/epoxy resin laminated plate using a progressive damage failure methodology.

### 7.4 Potential Applications to Structures

Near Infrared hyperspectral imaging is used to study the surface wrinkle distribution in the fabricated composite panel. Hybrid infrared imaging surfaces with a bottom-up design discretization approach have been developed to build the finite element model. The proposed method to predict the failure response of composite structures containing random and non-uniform out-of-plane waviness is demonstrated on laboratory size specimens. In the proposed method, NIR hyperspectral imaging is used to measure the actual surface resin profile and incorporate this shape to morph the mesh in a progressive damage based finite element model to predict the onset and propagation of damage in the composite structure. The proposed technique can be applied to a variety of composite structures where wrinkling of the plies can be related to small amounts of resin pooling on the surface. The results show different failure modes with a transition from localized fiber kink band formation in a sub-laminate region followed by fracture, to wide scale delamination depending on the location of the specimen. The proposed method overcomes the limitations of current wrinkle assessment methods by connecting the high sensitivity near infrared hyperspectral measurements to direct structural models. The proposed approach can be used on composite articles in a production or service environment, thereby allowing for a cost-effective, rapid, and non-invasive full-field structural integrity evaluation. As a final significant design consideration, this work will allow the ability to identify the failure onset load and its location and consequently used to determine the limit point in composite structures.

### 7.5 Future Studies

Understanding of damage evolutions resulting from preexisting defects in composite materials, can lead to new strategies for repair of specimens impacted by fiber-waviness by reducing the

interlaminar stresses and retardation of kink band formation. Overlay patch repair on the front side and back side of the specimen can be investigated with sensitivity analysis about all parameters related to the patch sizing. In addition, the following are considered areas worthy of future research.

- Exploring other test equipment to handle visual identification of the damage evolutions in composites with defects. The 3D CT scan can be used for kink band observation using high magnification and resolution. It will help researchers to track damage progression at the kinking initiation through the thickness which is currently unobservable.
- For numerically analyzing composite structures, the commercial FEA code provides diversiform element types associated with different constituent definitions which can be chosen according to the specific applications of composite structures. Meanwhile there is an undeniable difficulty related to the time of modeling and processing which impact the cost of analysis. There is a need to develop reliable elements to achieve convergent solutions in a shorter time. Also the future use of the FE method would be reliable by automating the process from the nondestructive imaging to the discretized element modeling. Using developed P-method can reduce the processing time.
- Fiber splitting failure mechanism is not included in numerical and analytical methods which may need to be examined for occurrence inside the kink band and at its boundaries. Important parameters (if splitting actually appear) would be their position (in relation to the kink band), location (matrix / interface between matrix and fibers), the stage in which they are formed and the number of fibers between splitting.
- The notch sizes less than waviness wave length needs to be explored. The size may go to micro level where the stress magnifications at waviness zone may be alleviated by using

Micro-drilling technology. The parameters which might be discovered through this technology include the drill sizing, drilling locations and patterns and data acquisition system.

- In plane fiber waviness is another common defect in composite laminates. The interactions of out of plane waviness with possible in plane waviness would be another area of concern for researcher in the field of effects of defects. All failure interactions for both waviness features can be defined as an individual study such as delamination and fiber failure dominancy as well as wave length and amplitude interactions.

- In order to accommodate the effects of defects on design performance, a reliability design optimization and safety analysis is strongly needed to perform. The objective of reliability design optimization is to discover a design that achieves a targeted probability of the composite structure failure containing defect and ensures expected optimum performance. In structural reliability analysis, reliability of the structure can use a failure criterion based on more likely damage mechanisms upon loading conditions and former defects. The analysis can be integrated with general finite element code.

## References


1. J., S., *Manufacturing defects in fibre-reinforced plastics composites*. Vol. 36. 1994, Northampton, ROYAUME-UNI: British Institute of Non-Destructive Testing.
2. D.J., W., *Effects of Defects in Composite Materials.* ASTM Special Technical Publication, 1984. **STP-836**.
3. M, H.R.a.S., *Review of defects and damage pertaining to composite aircraft components.* Composite Polymers, 1990. **3(2), 103-133**.
4. Cantwell, W.J. and J. Morton, *The significance of damage and defects and their detection in composite materials: A review.* The Journal of Strain Analysis for Engineering Design, 1992. **27**(1): p. 29-42.
5. Tsukrov, I., et al., *Finite Element Modeling to Predict Cure-Induced Microcracking in Three-Dimensional Woven Composites.* International Journal of Fracture, 2011. **172**(2): p. 209-216.
6. Shams, S.S. and R.F. El-Hajjar, *Overlay patch repair of scratch damage in carbon fiber/epoxy laminated composites.* Composites Part A: Applied Science and Manufacturing, 2013. **49**: p. 148-156.
7. Bayraktar, H., et al., *PREDICTING CURE-INDUCED MICROCRACKING IN 3D WOVEN COMPOSITES WITH REALISTIC SIMULATION TECHNOLOGY.* 2012.
8. Trey W. Riddle, D.S.C.a.J.W.N., *Characterization of Manufacturing Defects Common to Composite Wind Turbine Blades: Flaw Characterization.* 52nd AIAA/ASME/ASCE/AHS/ASC Structures, Structural Dynamics and Materials Conference, April 2011.
9. Riskalla, P.M.G.a.M.G., *Development of Probabilistic Design Methodology for Composite Structures*, August 1997, Vought Aircraft Company,DOT/FAA/AR-95/17.
10. Avdeev, I. and M. Gilaki, *Structural analysis and experimental characterization of cylindrical lithium-ion battery cells subject to lateral impact.* Journal of Power Sources, 2014. **271**: p. 382-391.
11. Huang, H. and R. Talreja, *Effects of void geometry on elastic properties of unidirectional fiber reinforced composites.* Composites Science and Technology, 2005. **65**(13): p. 1964-1981.
12. El-Hajjar, R.F. and D.R. Petersen, *Gaussian function characterization of unnotched tension behavior in a carbon/epoxy composite containing localized fiber waviness.* Composite Structures, 2011. **93**(9): p. 2400-2408.
13. Hsiao, H.M. and I.M. Daniel, *Elastic properties of composites with fiber waviness.* Composites Part a-Applied Science and Manufacturing, 1996. **27**(10): p. 931-941.
14. Soutis, C. and J. Lee, *Scaling effects in notched carbon fibre/epoxy composites loaded in compression.* Journal of Materials Science, 2008. **43**(20): p. 6593-6598.
15. Ratwani, M.M., *Effect of Damage on Strength and Durability.* NATO Research and Technology Organisation, May 2010 **RTO-EN-TR-AVT-156 AC/323(AVT-156)TP/333**
16. Dorri Moghadam, A., et al., *Direct Synthesis of Nanostructured in Situ Hybrid Aluminum Matrix Nanocomposite.* Industrial & Engineering Chemistry Research, 2016. **55**(22): p. 6345-6353.
17. Times, S. *Boeing finds new problem in 787, installing Patch*. 2009 [cited 2011 January 22, 2010]; Available from:

http://seattletimes.nwsource.com/html/localnews/2009664552_apusboeing7874thldwritethru.html. .
18. Chun, H.J., J.Y. Shin, and I.M. Daniel, *Nonlinear behavior of thick composites with uniform fiber waviness.* Aiaa Journal, 2000. **38**(10): p. 1949-1955.
19. Chun, H.J., J.Y. Shin, and I.M. Daniel, *Effects of material and geometric nonlinearities on the tensile and compressive behavior of composite materials with fiber waviness.* Composites Science and Technology, 2001. **61**(1): p. 125-134.
20. Hsiao, H.M. and I.M. Daniel, *Nonlinear elastic behavior of unidirectionai composites with fiber waviness under compressive loading.* Journal of Engineering Materials and Technology-Transactions of the Asme, 1996. **118**(4): p. 561-570.
21. Markatos, A., *Degradation of Mode-I Fracture Toughness of CFRP Bonded Joints Due to Release Agent and Moisture Pre-Bond Contamination.* The Journal of Adhesion, 2014. **90**(2): p. pages 156-173.
22. Mohammadi, T., B. Wan, and K.A. Harries, *Bond–slip behavior of fiber-reinforced polymer/concrete interface in single shear pull-out and beam tests.* Journal of Reinforced Plastics and Composites, 2015.
23. Mohammadi, T., et al., *Prediction of Load Capacity Variation in FRP Bonded Concrete Specimens Using Brownian Motion.* Mathematical Problems in Engineering, 2015. **2015**: p. 9.
24. Lee, S.H. and A. Waas, *Compressive response and failure of fiber reinforced unidirectional composites.* International Journal of Fracture, 1999. **100**(3): p. 275-306.
25. Arif, M.F., et al., *In situ damage mechanisms investigation of PA66/GF30 composite: Effect of relative humidity.* Composites Part B: Engineering, 2014. **58**: p. 487-495.
26. Seattle Times, *Boeing finds new problem in 787, installing Patch.* http://seattletimes.nwsource.com/html/localnews/2009664552_apusboeing7874thldwritethru.html., (August 14, 2009). **Last Accessed, January 22, 2010**.
27. J, L. and S. C, *A study on the compressive strength of thick carbon fibre–epoxy laminates.* Aerospace Engineering, 2007. **67(10):2015-2016.**
28. Ghazanfari, M.R., M. Kashefi, and M.R. Jaafari, *Investigation of stabilization mechanism and size controlling of Fe3O4 nanoparticles using anionic chelating agents.* Applied Surface Science, 2016. **375**: p. 50-56.
29. Ghazanfari, M.R., M. Kashefi, and M.R. Jaafari, *Optimizing and modeling of effective parameters on the structural and magnetic properties of Fe3O4 nanoparticles synthesized by coprecipitation technique using response surface methodology.* Journal of Magnetism and Magnetic Materials, 2016. **409**: p. 134-142.
30. Ghazanfari, M.R., M. Kashefi, and M.R. Jaafari, *Modeling and optimization of effective parameters on the size of synthesized Fe3O4 superparamagnetic nanoparticles by coprecipitation technique using response surface methodology.* Journal of Magnetism and Magnetic Materials, 2016. **405**: p. 88-96.
31. Potter, K., et al., *Variability, fibre waviness and misalignment in the determination of the properties of composite materials and structures.* Composites Part a-Applied Science and Manufacturing, 2008. **39**(9): p. 1343-1354.
32. Mohammadi, T. and B. Wan, *Sensitivity analysis of stress state and bond strength of fiber-reinforced polymer/concrete interface to boundary conditions in single shear pull-out test.* Advances in Mechanical Engineering, 2015. **7**(5).

33. Kugler, D. and T.J. Moon, *Identification of the Most Significant Processing Parameters on the Development of Fiber Waviness in Thin Laminates.* Journal of Composite Materials, 2002. **36**(12): p. 1451-1479.
34. Omrani, E., et al., *Mechanical and tribological properties of self-lubricating bio-based carbon-fabric epoxy composites made using liquid composite molding.* Tribology International, 2015. **92**: p. 222-232.
35. Lee, J. and C. Soutis, *A study on the compressive strength of thick carbon fibre–epoxy laminates.* Aerospace Engineering, 2007. **67(10):2015-2016.**
36. Kugler, D., P.J. Joyce, and T.J. Moon, *Investigation of the Effect of Part Length on Process-Induced Fiber-Wrinkled Regions in Composite Laminates.* Journal of Composite Materials, 1997. **31**(17): p. 1728-1757.
37. Wisnom, M.R. and J.W. Atkinson, *Fibre waviness generation and measurement and its effect on compressive strength.* Journal of Reinforced Plastics and Composites, 2000. **19**(2): p. 96-110.
38. Bradley, D.J., D.O. Adams, and H.E. Gascoigne, *Interlaminar strains and compressive strength reductions due to nested layer waviness in composite laminates.* Journal of Reinforced Plastics and Composites, 1998. **17**(11): p. 989-1011.
39. Hsiao, H.M. and I.M. Daniel, *Effect of fiber waviness on stiffness and strength reduction of unidirectional composites under compressive loading.* Composites Science and Technology, 1996. **56**(5): p. 581-593.
40. Piggott, M.R., *The effect of fibre waviness on the mechanical properties of unidirectional fibre composites: a review.* Composites science and technology, 1995. **53**(2): p. 201-205.
41. Altmann, A., P. Gesell, and K. Drechsler, *Strength prediction of ply waviness in composite materials considering matrix dominated effects.* Composite Structures, 2015. **127**: p. 51-59.
42. Mukhopadhyay, S., M.I. Jones, and S.R. Hallett, *Compressive failure of laminates containing an embedded wrinkle; experimental and numerical study.* Composites Part A: Applied Science and Manufacturing, 2015. **73**(0): p. 132-142.
43. El-Hajjar, R. and M. Lo Ricco, *Modified average stress criterion for open hole tension strength in presence of localised wrinkling.* Plastics, Rubber and Composites, 2012. **41**(9): p. 396-406.
44. Ampiah, N., A. Fam, and I. Moore, *Effect of Wrinkles on the Circumferential Strength of a Cast-in-Place Composite Polymer Liner Used in Retrofitting Pressure Pipes.* Journal of Materials in Civil Engineering, 2010. **22**(12): p. 1304-1314.
45. Fleck, N.A. and D. Liu, *Microbuckle initiation from a patch of large amplitude fibre waviness in a composite under compression and bending.* European Journal of Mechanics - A/Solids, 2001. **20**(1): p. 23-37.
46. Garnich, M.R. and G. Karami, *Localized Fiber Waviness and Implications for Failure in Unidirectional Composites.* Journal of Composite Materials, 2005. **39**(14): p. 1225-1245.
47. !!! INVALID CITATION !!!
48. Schultheisz, C.R. and A.M. Waas, *Compressive failure of composites, part I: Testing and micromechanical theories.* Progress in Aerospace Sciences, 1996. **32**(1): p. 1-42.
49. Rosen, B.W., *Mechanics of composite strengthening. fiber composite materials.* American Society of Metals, Metals Park, Ohio 1965: p. 37–75.
50. Steif, P.S., *An exact two-dimensional approach to fiber micro-buckling.* International Journal of Solids and Structures, 1987. **23**(9): p. 1235-1246.

51. Tadjbakhsh, I.G. and Y.M. Wang, *Fiber buckling in three-dimensional periodic-array composites.* International Journal of Solids and Structures, 1992. **29**(24): p. 3169-3183.
52. Budiansky, B., *Micromechanics.* Computers & Structures, 1983. **16**(1-4): p. 3-12.
53. Argon, A.S., *Fracture of Composites*, in *Treatise on Materials Science & Technology*, H. Herbert, Editor. 1972, Elsevier. p. 79-114.
54. Steif, P.S., *A model for kinking in fiber composites—I. Fiber breakage via micro-buckling.* International Journal of Solids and Structures, 1990. **26**(5–6): p. 549-561.
55. Berbinau, P., C. Soutis, and I.A. Guz, *Compressive failure of 0° unidirectional carbon-fibre-reinforced plastic (CFRP) laminates by fibre microbuckling.* Composites Science and Technology, 1999. **59**(9): p. 1451-1455.
56. Steif, P.S., *A model for kinking in fiber composites—II. Kink band formation.* International Journal of Solids and Structures, 1990. **26**(5–6): p. 563-569.
57. G., H.H.T.W.J., *Compression Failure Mechanisms in Unidirectional Composites.* NASA TM 85834, 1984.
58. Budiansky, B. and N.A. Fleck, *Compressive failure of fibre composites.* Journal of the Mechanics and Physics of Solids, 1993. **41**(1): p. 183-211.
59. Pimenta, S., et al., *A micromechanical model for kink-band formation: Part II—Analytical modelling.* Composites Science and Technology, 2009. **69**(7–8): p. 956-964.
60. Fleck, N.A., D. Liu, and J.Y. Shu, *Microbuckle initiation from a hole and from the free edge of a fibre composite.* International Journal of Solids and Structures, 2000. **37**(20): p. 2757-2775.
61. Daniel, I.M. and O. Ishai, *Engineering Mechanics Of Composite Materials.* OXFORD UNIVERSITY PRESS, 2006.
62. Whitney, J.M. and R.J. Nuismer, *Stress Fracture Criteria for Laminated Composites Containing Stress Concentrations.* Journal of Composite Materials, 1974. **8**(3): p. 253-265.
63. Nejhad, M.N.G. and T.-W. Chou, *A Model for the Prediction of Compressive Strength Reduction of Composite Laminates with Molded-In Holes.* Journal of Composite Materials, 1990. **24**(3): p. 236-255.
64. ASTM, *D 6484 Standard Test for Open-Hole Compressive Strength of Polymer Matrix Composite Laminates*, 2004: West Conshohocken, PA.
65. ASTM, *D5766 / D5766M - 11 Standard Test Method for Open-Hole Tensile Strength of Polymer Matrix Composite Laminates.* 2011.
66. Herakovich, C.T., *Mechanics of Fibrous Composites.* November 1997, ©1998.
67. Wisnom, M.R., *The effect of fibre waviness on the relationship between compressive and flexural strengths of unidirectional composites.* Journal of Composite Materials, 1994. **28**(1): p. 66-76.
68. Mandell, J., D. Samborsky, and L. Wang. *Effects of fiber waviness on composites for wind turbine blades*. in *International SAMPE symposium and exhibition*. 2003. SAMPE; 1999.
69. Allison, B.D. and J.L. Evans, *Effect of fiber waviness on the bending behavior of S-glass/epoxy composites.* Materials & Design, 2012. **36**(0): p. 316-322.
70. Hallett, S.R., *Three-point beam impact tests on T300/914 carbon-fibre composites.* Composites Science and Technology, 2000. **60**(1): p. 115-124.
71. Papadakis, N., et al., *Strain rate effects on the shear mechanical properties of a highly oriented thermoplastic composite material using a contacting displacement measurement methodology–Part A: elasticity and shear strength.* Composites Science and Technology, 2004. **64**(5): p. 729-738.

72. Alemi-Ardakani, M., A. Milani, and S. Yannacopoulos, *On Complexities of Impact Simulation of Fiber Reinforced Polymer Composites: A Simplified Modeling Framework.* The Scientific World Journal, 2014. **2014**.
73. Santiuste, C., S. Sánchez-Sáez, and E. Barbero, *A comparison of progressive-failure criteria in the prediction of the dynamic bending failure of composite laminated beams.* Composite Structures, 2010. **92**(10): p. 2406-2414.
74. Shenoy, V., et al., *An investigation into the crack initiation and propagation behaviour of bonded single-lap joints using backface strain.* International Journal of Adhesion and Adhesives, 2009. **29**(4): p. 361-371.
75. Czarnocki, P. and K. Piekarski, *Fracture strength of an adhesive-bonded joint.* International Journal of Adhesion and Adhesives, 1986. **6**(2): p. 93-95.
76. Adams, R.D. and P. Cawley, *A review of defect types and nondestructive testing techniques for composites and bonded joints.* NDT International, 1988. **21**(4): p. 208-222.
77. Sutcliffe, M.P.F., S.L. Lemanski, and A.E. Scott, *Measurement of fibre waviness in industrial composite components.* Composites Science and Technology, 2012. **72**(16): p. 2016-2023.
78. Nikishkov, G., Y. Nikishkov, and A. Makeev, *Finite element mesh generation for composites with ply waviness based on X-ray computed tomography.* Advances in Engineering Software, 2013. **58**(0): p. 35-44.
79. Pain, D. and B.W. Drinkwater, *Detection of fibre waviness using ultrasonic array scattering data.* Journal of Nondestructive Evaluation, 2013. **32**(3): p. 215-227.
80. Anastasi, R.F. *Investigation of fiber waviness in a thick glass composite beam using THz NDE*. 2008.
81. Elhajjar, R., R. Haj-Ali, and B.-S. Wei, *An Infrared Thermoelastic Stress Analysis Investigation for Detecting Fiber Waviness in Composite Structures.* Polymer-Plastics Technology and Engineering, 2014. **53**(12): p. 1251-1258.
82. Shelley, P.H., et al., *Near infrared imaging for measuring resin thickness on composites*, in *SAMPE Annual Conference*2014, Society for the Advancement of Material and Process Engineering: Seattle, Washington.
83. Tafti, A.P., et al., *Recent advances in 3D SEM surface reconstruction.* Micron, 2015. **78**: p. 54-66.
84. Tafti, A.P., et al., *3D Microscopy Vision Using Multiple View Geometry and Differential Evolutionary Approaches*, in *Advances in Visual Computing: 10th International Symposium, ISVC 2014, Las Vegas, NV, USA, December 8-10, 2014, Proceedings, Part II*, G. Bebis, et al., Editors. 2014, Springer International Publishing: Cham. p. 141-152.
85. Tafti, A.P., et al., *3DSEM++: Adaptive and intelligent 3D SEM surface reconstruction.* Micron, 2016. **87**: p. 33-45.
86. Tafti, A.P., et al., *3DSEM: A 3D microscopy dataset.* Data in Brief, 2016. **6**: p. 112-116.
87. Griffin, D.A. and M.C. Malkin. *Lessons Learned from Recent Blade Failures: Primary Causes and Risk-Reducing Technologies*. in *49th AIAA Aerospace Sciences Meeting including the New Horizons Forum and Aerospace Exposition*. 2011.
88. Goidescu, C., et al., *Damage investigation in CFRP composites using full-field measurement techniques: Combination of digital image stereo-correlation, infrared thermography and X-ray tomography.* Composites Part B: Engineering, 2013. **48**(0): p. 95-105.

89. Johanson, K., et al., *Heterogeneity of discontinuous carbon fibre composites: Damage initiation captured by Digital Image Correlation.* Composites Part A: Applied Science and Manufacturing, 2015. **68**(0): p. 304-312.
90. Dudderar, T.D. and P.G. Simpkins, *Laser speckle photography in a fluid medium.* Nature, 1977. **270**(5632): p. 45-47.
91. Hild, F. and S. Roux, *Digital Image Correlation: from Displacement Measurement to Identification of Elastic Properties – a Review.* Strain, 2006. **42**(2): p. 69-80.
92. Anandan, P., *A computational framework and an algorithm for the measurement of visual motion.* International Journal of Computer Vision, 1989. **2**(3): p. 283-310.
93. Sutton, M.A., et al., *Determination of displacements using an improved digital correlation method.* Image and Vision Computing, 1983. **1**(3): p. 133-139.
94. Périé, J.-N., et al., *Analysis of a multiaxial test on a C/C composite by using digital image correlation and a damage model.* Experimental Mechanics, 2002. **42**(3): p. 318-328.
95. Kashfuddoja, M. and M. Ramji, *Assessment of local strain field in adhesive layer of an unsymmetrically repaired CFRP panel using digital image correlation.* International Journal of Adhesion and Adhesives, 2015. **57**(0): p. 57-69.
96. Henry, T.C., et al. *Full-Field Strain Analysis of Compressively Loaded Flat Composite Laminates with Undulated Fibers*. in *Proceedings of the American Society for Composites 2014-Twenty-ninth Technical Conference on Composite Materials*. 2014. DEStech Publications, Inc.
97. Makeev, A., G. Seon, and E. Lee, *Failure predictions for carbon/epoxy tape laminates with wavy plies.* Journal of composite materials, 2009.
98. ASTM, *D3039 / D3039M - 08 Standard Test Method for Tensile Properties of Polymer Matrix Composite Materials.*
99. Dorri Moghadam, A., et al., *Mechanical and tribological properties of self-lubricating metal matrix nanocomposites reinforced by carbon nanotubes (CNTs) and graphene – A review.* Composites Part B: Engineering, 2015. **77**: p. 402-420.
100. Dorri Moghadam, A., et al., *Functional Metal Matrix Composites: Self-lubricating, Self-healing, and Nanocomposites-An Outlook.* JOM, 2014. **66**(6): p. 872-881.
101. Omrani, E., et al., *Influences of graphite reinforcement on the tribological properties of self-lubricating aluminum matrix composites for green tribology, sustainability, and energy efficiency—a review.* The International Journal of Advanced Manufacturing Technology, 2016. **83**(1): p. 325-346.
102. Barari, B., et al., *Mechanical, physical and tribological characterization of nano-cellulose fibers reinforced bio-epoxy composites: An attempt to fabricate and scale the 'Green' composite.* Carbohydrate Polymers, 2016. **147**: p. 282-293.
103. Cole, P.T., *Using acoustic emission (AE) to locate and identify defects in composite structures.* Composite Structures, 1985. **3**(3–4): p. 259-267.
104. Mehan, R.L.a.M., J. V.,, *Analysis of composite failure mechanisms using acoustic emissions.* J. Composite Matererials, 1971. **5**: p. 266-269.
105. Narisawa, I. and H. Oba, *An evaluation of acoustic emission from fibre-reinforced composites.* Journal of Materials Science, 1984. **19**(6): p. 1777-1786.
106. Qamhia, I., Lauer-Hunt, and E. E., R., , *Identification of Acoustic Emissions from Porosity and Waviness Defects in Continuous Fiber Reinforced Composites.* ASTM Journal of Advances in Civil Engineering Materials, 2013. **2**(1): p. 14.

107. Cheng, L. and G.Y. Tian, *Comparison of Nondestructive Testing Methods on Detection of Delaminations in Composites.* Journal of Sensors, 2012. **2012**: p. 7.
108. Wróbel, G.W., Ł. , *Ultrasonic methods in diagnostics of glass-polyester composites.* Journal of Achievements in Materials and Manufacturing Engineering, 2007. **Vol. 20**( nr 1-2): p. 203-206
109. Potel, C., et al., *Characterization of composite materials by ultrasonic methods: modelization and application to impact damage.* Composites Part B: Engineering, 1998. **29**(2): p. 159-169.
110. Marsh, G., *Finding flaws in composites.* Reinforced Plastics, 2002: p. 42-46.
111. G. Wróbel, S.P., *A comparison study of the pulse-echo and through-transmission ultrasonics in glass/epoxy composites.* Journal of Achievements in Materials and Manufacturing Engineering, 2007. **22**(2).
112. Slaughter, W.S., B. Budiansky, and N.A. Fleck, *Compressive Failure of Fiber Composites: The Roles of Multiaxial Loading and Creep.* Journal of Engineering Materials and Technology, 1993. **115**(3): p. 308-313.
113. Fleck, N.A. and P.M. Jelf, *Deformation and failure of a carbon fibre composite under combined shear and transverse loading.* Acta Metallurgica et Materialia, 1995. **43**(8): p. 3001-3007.
114. Carlos, D., C. Pedro Ponces, and R. Cheryl, *Failure criteria for FRP laminates.* 2005.
115. Maimí, P., et al., *A continuum damage model for composite laminates: Part I – Constitutive model.* Mechanics of Materials, 2007. **39**(10): p. 897-908.
116. Turon, A., et al., *A damage model for the simulation of delamination in advanced composites under variable-mode loading.* Mechanics of Materials, 2006. **38**(11): p. 1072-1089.
117. Krueger, R., *Virtual crack closure technique: History, approach, and applications.* Applied Mechanics Reviews, 2004. **57**(2): p. 109-143.
118. Matzenmiller, A., J. Lubliner, and R.L. Taylor, *A constitutive model for anisotropic damage in fiber-composites.* Mechanics of Materials, 1995. **20**(2): p. 125-152.
119. G.I, B., *The Mathematical Theory of Equilibrium Cracks in Brittle Fracture*, in *Advances in Applied Mechanics*, T.v.K.G.K.F.H.v.d.D. H.L. Dryden and L. Howarth, Editors. 1962, Elsevier. p. 55-129.
120. A. Hillerborg, M.M., P.E. Petersson, *Analysis of crack formation and crack growth in concrete by means of fracture mechanics and finite elements.* Cement and Concrete Research, 1976. **6, 773-782**.
121. Shams, S.S. and R.F. El-Hajjar, *Effects of scratch damage on progressive failure of laminated carbon fiber/epoxy composites.* International Journal of Mechanical Sciences, 2013. **67**: p. 70-77.
122. Abaqus, *Abaqus 6-11EF*, in *Dassault Systems*2011, Simulia.
123. Pedro P Camanho, C.G.D., *Mixed-Mode Decohesion Finite Elements for the Simulation of Delamination in Composite Materials.* NASATechnical Paper, 2002.
124. Turon, A., et al., *An engineering solution for mesh size effects in the simulation of delamination using cohesive zone models.* Engineering Fracture Mechanics, 2007. **74**(10): p. 1665-1682.
125. Ted, D., *On using a penalty-based cohesive-zone finite element approach, Part I: Elastic solution benchmarks.* International Journal of Adhesion and Adhesives, 2008. **28**(4-5): p. 237-255.

126. Camanho P.P., D.a.C.G., de Moura M.F. , *Numerical Simulation of Mixed-Mode Progressive Delamination in Composite Materials.* Journal of Composite Materials, 2003. **37 (16), 1415-1438**.
127. Benzeggagh, M.L. and M. Kenane, *Measurement of mixed-mode delamination fracture toughness of unidirectional glass/epoxy composites with mixed-mode bending apparatus.* Composites Science and Technology, 1996. **56**(4): p. 439-449.
128. Seyedmohammad S Shams, R.F.E.-H., *Multi-mode Failure Analysis of Scratched Laminated Carbon Fiber/Epoxy Composites.* SIMULIA Community Conference 2013.
129. Hashin, Z., *Failure Criteria for Unidirectional Fiber Composites.* Journal of Applied Mechanics, June 1980. **Volume 47, Issue 2, 329 (6 pages)**.
130. Puck, A. and H. Schürmann, *FAILURE ANALYSIS OF FRP LAMINATES BY MEANS OF PHYSICALLY BASED PHENOMENOLOGICAL MODELS.* Composites Science and Technology, 1998. **58**(7): p. 1045-1067.
131. Hinton, M.J., A.S. Kaddour, and P.D. Soden, *A comparison of the predictive capabilities of current failure theories for composite laminates, judged against experimental evidence.* Composites Science and Technology. **62**(12-13): p. 1725-1797.
132. Simulia, *Abaqus/Explicit VUMAT for the simulation of damage and failure in unidirectional fiber composite materials.* ABAQUS VUMAT, July 2011.
133. Tomblin J, S.J., Seneviratne W, Raju KS, , *Advanced General Aviation Transport Experiments. A – Basis and B – Basis Design Allowables for Epoxy – Based Prepreg TORAY T700GC-12K-31E/#2510 Unidirectional Tape,* 2002, National Institute for Aviation Research Wichita State University: Wichita, Kansas.
134. ASTM, *Mode I Interlaminar fracture Toughness of Unidirectional Fiber-Reinforced Polymer Matrix Composites.* D5528-01, 2007.
135. Daniel, I. and O. Ishai, *Engineering Mechanics of Composite Materials*. Vol. Second edition. 2006: Oxford University Press.
136. Wang, J., et al., *Experimental fabrication and characterization of out-of-plane fiber waviness in continuous fiber-reinforced composites.* Journal of Composite Materials, 2012. **46**(17): p. 2041-2053.
137. Bloom, D., J. Wang, and K. Potter, *Damage progression and defect sensitivity: An experimental study of representative wrinkles in tension.* Composites Part B: Engineering, 2012.
138. Elhajjar, R.F. and S.S. Shams, *Compression testing of continuous fiber reinforced polymer composites with out-of-plane fiber waviness and circular notches.* Polymer Testing, 2014. **35**: p. 45-55.
139. Berg, C.A. and M. Salama, *Fatigue of graphite fibre-reinforced epoxy in compression.* Fibre Science and Technology, 1973. **6**(2): p. 79-118.
140. Shams, S. and R. Elhajjar, *Investigation into the effects of fiber waviness in standard notched composite specimens.* CEAS Aeronautical Journal, 2015. **6**(4): p. 541-555.
141. Caminero, M.A., et al., *Damage monitoring and analysis of composite laminates with an open hole and adhesively bonded repairs using digital image correlation.* Composites Part B: Engineering, 2013. **53**(0): p. 76-91.
142. H. Thomas Hahn, M.S.a.S.M., *Compression Failure Mechanisms of Composite Structures.* NASA Technical Report, Langley Research Center, 1986.

143. Seyedmohammad S Shams, R.F.E.-H., *On Using the Open Hole Tension and Compression Specimens for Evaluating the Waviness Effects in Laminated Composites.* Proceedings of the American Society for Composites 2014. **Twenty-ninth Technical Conference on Composite Materials**
144. Berbinau, P., et al., *Effect of off-axis ply orientation on 0°-fibre microbuckling.* Composites Part A: Applied Science and Manufacturing, 1999. **30**(10): p. 1197-1207.
145. Prabhakar, P. and A.M. Waas, *Micromechanical modeling to determine the compressive strength and failure mode interaction of multidirectional laminates.* Composites Part A: Applied Science and Manufacturing, 2013. **50**(0): p. 11-21.
146. Lee, J. and C. Soutis, *A study on the compressive strength of thick carbon fibre–epoxy laminates.* Composites Science and Technology, 2007. **67**(10): p. 2015-2026.
147. 08, A.D.D.M.-. *Standard Test Method for Tensile Properties of Polymer Matrix Composite Materials.*
148. Seyedmohammad S Shams, R.F.E.-H., *The Open Hole Compression Test for Evaluation of the Effects of Fiber Waviness in Fiber Reinforced Composites.* ANTEC 2014, 2014.
149. Elhajjar, R.F. and S.S. Shams, *A new method for limit point determination in composite materials containing defects using image correlation.* Composites Science and Technology.
150. El-Hajjar, R. and D.R. Petersen, *Adhesive Polyvinyl Chloride Coatings for Quantitative Strain Measurement in Composite Materials.* Composites Part B-Engineering, 2011. **42**(7): p. 1929-1936.
151. Elhajjar, R.F., et al., *A hybrid numerical and imaging approach for characterizing defects in composite structures.* Composites Part A: Applied Science and Manufacturing, 2016. **81**: p. 98-104.
152. ASTM, *D7264 / D7264M - 15 Standard Test Method for Flexural Properties of Polymer Matrix Composite Materials.*
153. Gemma, R., et al., *Focused ion beam as a tool for graphene technology: Structural study of processing sequence by electron microscopy.* Japanese Journal of Applied Physics, 2014. **53**(2S): p. 02BC22.
154. Tavabi, A.H., Z. Yasenjiang, and T. Tanji, *In situ off-axis electron holography of metal-oxide hetero-interfaces in oxygen atmosphere.* J Electron Microsc (Tokyo), 2011. **60**(5): p. 307-14.
155. Hashin, Z., *Failure criteria for unidirectional fiber composites.* Journal of applied mechanics, 1980. **47**(2): p. 329-334.
156. Puck, A. and H. Schürmann, *Failure analysis of FRP laminates by means of physically based phenomenological models.* Composites Science and Technology, 2002. **62**(12): p. 1633-1662.
157. Zhou, Y., Z. Lu, and Z. Yang, *Progressive damage analysis and strength prediction of 2D plain weave composites.* Composites Part B: Engineering, 2013. **47**(0): p. 220-229.
158. Abaqus, *Abaqus 6-13.14*, in *Dassault Systems*2013, Simulia.
159. Yang, P., et al., *Evaluation of temperature effects on low velocity impact damage in composite sandwich panels with polymeric foam cores.* Composite Structures, 2015. **129**: p. 213-223.
160. Kyriakides, S., et al., *On the compressive failure of fiber reinforced composites.* International Journal of Solids and Structures, 1995. **32**(6): p. 689-738.

## B**iography**

Sadegh Shams joined the College of Engineering at University of Wisconsin-Milwaukee in 2011 as a Research Assistant. His expertise falls in the areas of experimental and computational solid mechanics, with specializations in numerical multiphysics analysis, characterization and optimization of engineering materials and design, manufacturing and identifications of composite materials. He has been fortunate to obtain diversity in his academic training in Mechanical and Aerospace Engineering and ten years of professional experiences working as a Research Assistant, Stress Analysis Engineer and Structural Condition Monitoring Engineer.

He has published numerous papers in high prestigious journals, conferences and book chapters. He has presented his research in several professional associations and exhibitions. He is serving as a reviewer for top tier conferences and journals such as ASME and SAE.

In addition to Distinguished Dissertation Fellowship for 2015 he has won several awards such as CMMI-Engineering Research and Innovation Conference, GE Healthcare awards student researchers for innovation, Student award in ASTM-E08 Fracture Mechanics.

At University of Wisconsin, he has advised both graduate and undergraduate students in discussion and laboratory classes for eight semesters. He was a mentor for undergraduate students competing in a NASA sponsored competition to design a composite based lunar wheel (won the second place). In the X-Hab project sponsored by NASA which was assigned to design a carbon-fiber/FDM spacecraft structural fabrication System (SSFS) for manufacturing recyclable and high performing structural parts in a zero-g environment, he served as the leader for the structural analysis group.

Selected Publications:

- **Seyedmohammad S. Shams**, Rani F. Elhajjar, “Investigation into the Effects of Fiber Waviness in Standard Notched Composite Specimens”, CEAS Aeronautical Journal, August 2015
- Rani F. Elhajjar, **Seyedmohammad S. Shams**, Gabor J. Kemeny, Gina Stuessy, ” A Hybrid Numerical and Imaging Approach for Characterizing Defects in Composite Structures”, Composite Part A., October 2015
- Rani F. Elhajjar, **Seyedmohammad S. Shams**,“ A new method for limit point determination in composite materials containing defects using image correlation”, Composites Science and Technology, Nov 2015
- **Seyedmohammad S. Shams**, Peng Yang, and Rani F. Elhajjar, “Damage Initiation and Fatigue Behavior of Carbon-Fiber Composite Disk Springs”, SAE International Journal of Materials and Manufacturing, 2015-01-908